NOV 2 1961
LIBRARY

MONTHLY NOTICES

NOV 6 1961

OF THE

ROYAL ASTRONOMICAL SOCIETY

Volume 123 No. 1 1961

Published and Sold by the

ROYAL ASTRONOMICAL SOCIETY
BURLINGTON HOUSE
LONDON, W.1

Price £1 4s. 0d. (*US* $3.50)

Subscription for volume £6 (*US* $18)

XUM

NOW AVAILABLE

MEMOIRS

OF THE

ROYAL ASTRONOMICAL SOCIET

VOL. LXVIII—PART III

CONTENTS

CLASSIFICATION AND RADIAL VELOCITIES OF BRIGHT SOUTHERN GALAXIES

by

GERARD DE VAUCOULEURS

AND

ANTOINETTE DE VAUCOULEURS

AND

ANALYSIS OF LIMB DARKENING OBSERVATIONS

by

A. KEITH PIERCE AND JOHN H. WADDELL

PRICE £1 (US $3)

Orders to:

ASSISTANT SECRETARY, ROYAL ASTRONOMICAL SOCIETY,
Burlington House, London, W.1
England

XUM

MONTHLY NOTICES
OF THE
ROYAL ASTRONOMICAL SOCIETY
Vol. 123 No. 1

ON THE USE OF THE JACOBI INTEGRAL OF THE RESTRICTED THREE-BODY PROBLEM

M. W. Ovenden and A. E. Roy

(Communicated by the Director of the Glasgow University Observatory)

(Received 1960 October 14)

Summary

Some authors have used the Jacobi integral of the classical restricted three-body problem (two massive bodies moving in a circular relative orbit and an infinitesimal third body) as an approximate integral in the elliptical restricted three-body problem (where the two massive bodies move in an elliptical relative orbit). This paper discusses, from first principles, the justification for this approximation. The coordinates and velocities of the three bodies are expressed as power series in the relative mass of the third body, and the series are substituted in the integrals of the general three-body problem (expressed in non-uniformly rotating rectangular coordinates), the limit as the relative mass of the third body approaches zero being then taken. In this way, formal expressions for the Jacobi integral and the angular momentum integrals of the elliptical restricted three-body problem are obtained in terms of certain auxiliary functions (whose physical significance is exhibited by the development adopted). However, the behaviour in time of these auxiliary functions is known only through explicit equations for their first time-derivatives in terms of the coordinates of the infinitesimal body. It is considered that, in the absence of any other known integrals involving these auxiliary functions, there is no justification for assuming that conclusions drawn for arbitrarily long times from the Jacobi integral of the classical problem are approximately true in the elliptical case.

1. *Introduction.*—It is well known that the equations of motion of a body of infinitesimal mass moving under the gravitational attractions of two massive bodies, which move in circles about their common centre of gravity (the circular restricted three-body problem), admit of an integral, called, after its discoverer, the Jacobi integral (**1**). According to Bruns (**2**), no other algebraic integrals of this problem exist (when rectangular coordinates are used), while Poincaré (**3**) has shown that if the elements of the orbits are used as variables, there are no new uniform transcendental integrals, even when the mass of one of the finite bodies is very small compared with the mass of the other.

The Jacobi integral has been used for two different purposes, viz. (*a*) to construct surfaces of zero velocity which limit the regions of space in which the small body, under given initial conditions, can move, and (*b*) to derive a criterion (the Tisserand criterion) for the re-identification of a comet whose orbit has suffered severe perturbations by a planet. It should be noted that under (*a*), long-term predictions are made, while under (*b*) only short-term predictions are made.

In using (*b*), for example in the case of Jupiter, the Jacobi integral is not strictly valid, since the planet moves about the Sun in an (approximately) elliptic orbit. Attempts to take partially into account the departure from circular orbits (i.e. to treat the elliptical restricted three-body problem) have been made by several authors (e.g. Callandreau (**4**)).

Several authors have also used the circular Jacobi as an approximate integral of the elliptical restricted three-body problem, under (*a*). Thus Hill (**5**), treating the Moon as an infinitesimal body in the Sun–Earth–Moon system, and neglecting the eccentricity of the Earth's orbit about the Sun, concluded that the Moon's distance from the Earth has a superior limit. Although Hill was careful to point out that his conclusion was valid only to the extent to which the behaviour of the Sun–Earth–Moon system could be represented by the circular restricted three-body problem, this reservation has not always been remembered by subsequent authors.

The restricted three-body problem has been applied in a wide variety of contexts. Thus Hagihara (**7**) has discussed the stability of the orbits of the satellites of the solar system, Kopal (**8**) has investigated the transfer of material between the components of a close binary star, and Huang (**9**) has studied the stability of planetary orbits in binary systems. Recently, several authors have discussed the behaviour of a lunar probe, using the circular restricted three-body problem (see, e.g., **10**). The time thus seems appropriate for a re-examination of the validity of conclusions drawn from the application of the circular Jacobi as an approximation in the elliptical restricted three-body problem.

The Jacobi integral is usually derived by direct integration of equations of motion constructed under the assumption that the infinitesimal body is attracted by, but does not attract, the massive bodies (which move in undisturbed circular orbits about their common centre of gravity) (see, e.g., **11**, **12**). We prefer to derive the integral from the general equations of motion, making the mass of the third body approach zero only after the integration (a process that we have not discovered in print). This procedure admits of a ready generalization to the elliptical case.

2. *Integrals of the general three-body problem in non-uniformly rotating rectangular coordinates.*—Let three bodies, m_1, m_2 and m_3, move, under their mutual gravitational attractions, about their centre of gravity G. Adopting gravitational units (constant of gravitation = 1), the equations of motion of the three bodies with respect to a Galilean set of axes $Gxyz$ are

$$\left.\begin{aligned} m_i\ddot{x}_i = m_i\frac{\partial}{\partial x_i}\sum_j\frac{m_j}{r_{ij}} &= \frac{\partial U}{\partial x_i}\\ m_i\ddot{y}_i &= \frac{\partial U}{\partial y_i}\\ m_i\ddot{z}_i &= \frac{\partial U}{\partial z_i}\end{aligned}\right\} \qquad (1)$$

where $i, j = 1, 2, 3$ and $U = \frac{1}{2}\sum_j\sum_i\frac{m_i m_j}{r_{ij}}$, $j \neq i$.

Letting the positions of the bodies be now referred to a set of axes $G\xi\eta\zeta$, where $G\zeta \equiv Gz$, and $\underline{\xi Gx} = \phi = f(t)$, equations (1) lead to

$$\ddot{\xi}_i - 2\dot{\eta}_i\dot{\phi} - \xi_i\dot{\phi}^2 - \eta_i\ddot{\phi} = \frac{1}{m_i}\frac{\partial U}{\partial \xi_i}, \qquad (2)$$

$$\ddot{\eta}_i + 2\dot{\xi}_i\dot{\phi} - \eta_i\dot{\phi}^2 + \xi_i\ddot{\phi} = \frac{1}{m_i}\frac{\partial U}{\partial \eta_i}, \qquad (3)$$

$$\ddot{\zeta}_i = \frac{1}{m_i}\frac{\partial U}{\partial \zeta_i}. \qquad (4)$$

These equations admit of the following integrals:

$$\sum_i m_i\{(\dot{\xi}_i^2+\dot{\eta}_i^2+\dot{\zeta}_i^2)-\dot{\phi}^2(\xi_i^2+\eta_i^2)\}=2U+2C_3\dot{\phi}+D \tag{5}$$

$$\sum_i m_i\{(\eta_i\dot{\xi}_i-\xi_i\dot{\eta}_i)-\dot{\phi}(\xi_i^2+\eta_i^2)\}=C_3 \tag{6}$$

$$\sum_i m_i\{(\xi_i\dot{\zeta}_i-\zeta_i\dot{\xi}_i)+\dot{\phi}\zeta_i\eta_i\}=C_1\sin\phi-C_2\cos\phi \tag{7}$$

$$\sum_i m_i\{(\eta_i\dot{\zeta}_i-\zeta_i\dot{\eta}_i)-\dot{\phi}\zeta_i\xi_i\}=C_1\cos\phi+C_2\sin\phi \tag{8}$$

where C_1, C_2, C_3 and D are constants.

Equations (6), (7) and (8) are the angular momentum integrals. The Jacobi integral is derived from equation (5).

Now put $m_3=\mu m_2=\mu\alpha m_1$, where $\mu\leqslant 1$, $\alpha\leqslant 1$. Equations (2), (3) and (4) then lead to the relations associated with the centre of gravity, viz.:

$$\left.\begin{aligned}\xi_3&=-\frac{1}{\mu}\left\{\frac{1}{\alpha}\xi_1+\xi_2\right\} \qquad \eta,\zeta\\ \dot{\xi}_3&=-\frac{1}{\mu}\left\{\frac{1}{\alpha}\dot{\xi}_1+\dot{\xi}_2\right\} \qquad \dot{\eta},\dot{\zeta}\end{aligned}\right\}. \tag{9}$$

Equations (5)–(9) give the ten known integrals of the general three-body problem in a non-uniformly rotating frame of reference.

3. *Derivation of the integrals of the circular restricted three-body problem.*—We take the initial position at $t=0$ of the axes $G\xi\eta\zeta$ as follows: $G\xi$ is parallel to the line $m_2G'm_1$ where G' is the centre of gravity of m_1 and m_2. The $\xi\eta$-plane is taken parallel to the plane through $m_2G'm_1$ containing the instantaneous velocity vector of m_1. At $t=0$, we let $G'm_1=a_1$ and $G'm_2=a_2$, where $a_1=\alpha a_2$. We also assume that at $t=0$ the velocity vectors of the two bodies m_1 and m_2 are the circular velocity vectors about G'. Thus the instantaneous velocity vector of m_2 will be parallel to the plane $\xi\eta$. We now suppose that the axes $G\xi$ and $G\eta$ rotate about $G\zeta$ with constant angular velocity n given by

$$n^2=(m_1+m_2)/(a_1+a_2)^3. \tag{10}$$

We shall derive Jacobi's integral from (5) with $\dot{\phi}=n$ (and $\ddot{\phi}=0$). (In the elliptic case we shall be using (5) with a variable $\dot{\phi}$.)

At any other time t we may write

$$\begin{aligned}\xi_1&=a_1+\xi_{11}, & \xi_2&=-a_2+\xi_{21},\\ \eta_1&=\eta_{11}, & \eta_2&=\eta_{21},\\ \zeta_1&=\zeta_{11}, & \zeta_2&=\zeta_{21},\end{aligned}$$

where $(\xi,\eta,\zeta)_{11,21}$ and $(\dot{\xi},\dot{\eta},\dot{\zeta})_{11,21}$, of order (μ), tend to zero as μ tends to zero but are not necessarily equal to zero at $t=0$ if μ does not equal zero.

Then by a known theorem (**13**) we have, over any fixed range $0\leqslant t\leqslant T$, and for $\mu<\mu_0$, where μ_0 depends on T so that T can be made arbitrarily large by taking μ_0 arbitrarily small, and for each of ξ_i, η_i, ζ_i, $i=1,2$, the expansions given below, namely

$$\left.\begin{aligned}\xi_{i1}&=\sum_{p=1}^{\infty}\mu^p\Xi_i(t)\mu^p\\ \eta_{i1}&=\sum_{p=1}^{\infty}\mu^p\mathrm{H}_i(t)\mu^p\\ \zeta_{i1}&=\sum_{p=1}^{\infty}\mu^p\,\mathrm{Z}_i(t)\mu^p\end{aligned}\right\} i=1,2.$$

Furthermore,

$$\dot{\xi}_{i1} = \sum_{p=1}^{\infty} {}^{p}\dot{\Xi}_i(t)\mu^p, \qquad \ddot{\xi}_{i1} = \sum_{p=1}^{\infty} {}^{p}\ddot{\Xi}_i(t)\mu^p, \quad \text{etc.}$$

Since the series are all of the form $\chi_1(t)\mu + O(\mu^2)$, $(t \leqslant T)$, we may, with a new notation, write

$$\left.\begin{aligned} &\xi_1 = a_1 + \mu\,{}^{1}\Xi_1 + O(\mu^2), \qquad \xi_2 = -a_2 + \mu\,{}^{1}\Xi_2 + O(\mu^2),\\ &\dot{\xi}_i = \mu\,{}^{1}\dot{\Xi}_i + O(\mu^2),\\ &\eta_i = \mu\,{}^{1}\mathrm{H}_i + O(\mu^2), \qquad \dot{\eta}_i = \mu\,{}^{1}\dot{\mathrm{H}}_i + O(\mu^2)\\ &\zeta_i = \mu\,{}^{1}\mathrm{Z}_i + O(\mu^2), \qquad \dot{\zeta}_i = \mu\,{}^{1}\dot{\mathrm{Z}}_i + O(\mu^2) \end{aligned}\right\} \quad i = 1, 2.$$

We write further,

$$V = m_1/r_{13} + m_2/r_{23}, \qquad J = v^2 - n^2R^2 - 2V,$$

where $v^2 = \dot{\xi}_3^2 + \dot{\eta}_3^2 + \dot{\zeta}_3^2$, $R^2 = \xi_3^2 + \eta_3^2$.

We have now from (5), with an obvious notation,

$$m_3 \frac{dJ}{dt} = \frac{d}{dt}\left\{ -\sum_{1,2} m_i(v_i^2 - n^2R_i^2) + \frac{2m_1m_2}{r_{12}} \right\}. \tag{11}$$

Now

$$\frac{d}{dt}(v_i^2) = 2(\dot{\xi}_i\ddot{\xi}_i + \dot{\eta}_i\ddot{\eta}_i + \dot{\zeta}_i\ddot{\xi}_i) = O(\mu^2). \tag{12}$$

$$\begin{aligned} \frac{d}{dt}\left(n^2 \sum_{1,2} m_iR_i^2 \right) &= n^2 \frac{d}{dt}[m_1(a_1 + \mu\,{}^{1}\Xi_1)^2 + m_2(-a_2 + \mu\,{}^{1}\Xi_2)^2 + O(\mu^2)]\\ &= 2n^2\mu(m_1a_1\,{}^{1}\dot{\Xi}_1 - m_2a_2\,{}^{1}\dot{\Xi}_2) + O(\mu^2). \end{aligned}$$

Now

$$m_1a_1 = m_2a_2 = (a_1 + a_2)/(m_1^{-1} + m_2^{-1}) = \frac{m_1m_2(a_1 + a_2)}{m_1 + m_2}.$$

Hence we have

$$\frac{d}{dt}\left(n^2 \sum_{1,2} m_iR_i^2 \right) = n^2 \frac{2m_1m_2}{m_1 + m_2}(a_1 + a_2)\mu({}^{1}\dot{\Xi}_1 - {}^{1}\dot{\Xi}_2) + O(\mu^2). \tag{13}$$

Next,

$$\begin{aligned} \frac{d}{dt}\left(\frac{2m_1m_2}{r_{12}} \right) &= 2m_1m_2 \frac{d}{dt}[(\xi_1 - \xi_2)^2 + (\eta_1 - \eta_2)^2 + (\zeta_{12} - \zeta_2)^2]^{-1/2}\\ &= 2m_1m_2 \frac{d}{dt}\{[(a_1 + a_2) + \mu({}^{1}\Xi_1 - {}^{1}\Xi_2)]^2 + O(\mu^2)\}^{-1/2}\\ &= -2m_1m_2(a_1 + a_2)^{-2}\mu({}^{1}\dot{\Xi}_1 - {}^{1}\dot{\Xi}_2) + O(\mu^2). \end{aligned}$$

From this, (11), (12), (13), we have, substituting for n^2 in (11) from (10),

$$m_3\dot{J} = O(\mu^2),$$

that is $\dot{J} = O(\mu)$, or

$$J = J(0) + O(\mu) = \kappa + O(\mu),$$

where κ is a constant. Then, letting $\mu \to 0$, we have the "circular" Jacobi,

$$(\dot{\xi}_3^2 + \dot{\eta}_3^2 + \dot{\zeta}_3^2) - n^2(\xi_3^2 + \eta_3^2) = 2\left(\frac{m_1}{r_{13}} + \frac{m_2}{r_{23}} \right) + \kappa. \tag{14}$$

Consider now the integrals of angular momentum. From (6),

$$m_3 \frac{d}{dt}[(\eta_3\dot{\xi}_3 - \xi_3\dot{\eta}_3) - n(\xi_3^2 + \eta_3^2)] = -\frac{d}{dt}\left\{ \sum_{1,2} m_i[(\eta_i\dot{\xi}_i - \xi_i\dot{\eta}_i) - n(\xi_i^2 + \eta_i^2)] \right\}.$$

Putting $\omega_\zeta=(\eta_3\dot{\xi}_3-\xi_3\dot{\eta}_3)-n(\xi_3^2+\eta_3^2)$, we obtain

$$m_3\frac{d}{dt}\omega_\zeta=-\frac{d}{dt}\{-m_1a_1\mu({}^1\dot{\mathrm{H}}_1-{}^1\dot{\mathrm{H}}_2)-n[(m_1a_1^2+m_2a_2^2)+2m_1a_1\mu({}^1\Xi_1-{}^1\Xi_2)]+O(\mu^2)\},$$

or

$$m_3\frac{d}{dt}\omega_\zeta=-\frac{d}{dt}\{-m_1a_1\mu[({}^1\dot{\mathrm{H}}_1-{}^1\dot{\mathrm{H}}_2)+2n({}^1\Xi_1-{}^1\Xi_2)]+O(\mu^2)\}.$$

That is, dividing by m_3 and integrating, we obtain

$$\omega_\zeta=\omega_\zeta(0)+a_2[({}^1\dot{\mathrm{H}}_1-{}^1\dot{\mathrm{H}}_2)+2n({}^1\Xi_1-{}^1\Xi_2)]+O(\mu).$$

Then, writing $\mathrm{H}={}^1\mathrm{H}_1-{}^1\mathrm{H}_2$, $\Xi={}^1\Xi_1-{}^1\Xi_2$, and letting $\mu\to0$, we obtain

$$(\eta_2\dot{\xi}_3-\xi_3\dot{\eta}_3)-n(\xi_3^2+\eta_3^2)=K+a_2(\dot{\mathrm{H}}+2n\Xi), \tag{15}$$

where K is a constant of integration.

The other two integrals must be treated together.

From (7) and (8) we have, putting

$$A=\sum_i m_i[(\xi_i\dot{\zeta}_i-\zeta_i\dot{\xi}_i)+n\zeta_i\eta_i],$$

and

$$B=\sum_i m_i[(\eta_i\dot{\zeta}_i-\zeta_i\dot{\eta}_i)-n\zeta_i\xi_i],$$

$$\frac{dA}{dt}-nB=0,\qquad \frac{dB}{dt}+nA=0.$$

Then, from the first of these equations we get

$$m_3\left\{\frac{d}{dt}[(\xi_3\dot{\zeta}_3-\zeta_3\dot{\xi}_3)+n\zeta_3\eta_3]-n[(\eta_3\dot{\zeta}_3-\zeta_3\dot{\eta}_3)-n\zeta_3\xi_3]\right\}$$
$$=-\frac{d}{dt}\left\{\sum_{1,2}m_i[(\xi_i\dot{\zeta}_i-\zeta_i\dot{\xi}_i)+n\zeta_i\eta_i]\right\}+n\left\{\sum_{1,2}m_i[(\eta_i\dot{\zeta}_i-\zeta_i\dot{\eta}_i)-n\zeta_i\xi_i]\right\},$$

or

$$m_3\left\{\frac{d}{dt}[(\xi_3\dot{\zeta}_3-\zeta_3\dot{\xi}_3)+n\zeta_3\eta_3]-n[(\eta_3\dot{\zeta}_3-\zeta_3\dot{\eta}_3)-n\zeta_3\xi_3]\right\}$$
$$=-\frac{d}{dt}[m_1a_1\dot{\zeta}_{11}-m_2a_2\dot{\zeta}_{21}]-n^2(m_1a_1\zeta_{11}-m_2a_2\zeta_{21})+O(\mu^2).$$

Then, with obvious notation, we have

$$m_3\left[\frac{d}{dt}A_3-nB_3\right]=-\frac{d}{dt}[m_1a_1\mu({}^1\dot{\mathrm{Z}}_1-{}^1\dot{\mathrm{Z}}_2)]-n^2m_1a_1\mu({}^1\mathrm{Z}_1-{}^1\mathrm{Z}_2)+O(\mu^2).$$

Writing $\mathrm{Z}={}^1\mathrm{Z}_1-{}^1\mathrm{Z}_2$, etc., we obtain

$$\frac{d}{dt}[A_3+a_2\dot{\mathrm{Z}}]-n[B_3-na_2\mathrm{Z}]=O(\mu). \tag{16}$$

In a similar manner, from the second equation, namely $dB/dt+nA=0$, we obtain

$$\frac{d}{dt}[B_3-na_2\mathrm{Z}]+n[A_3+a_2\dot{\mathrm{Z}}]=o(\mu). \tag{17}$$

The solutions, to (16) and (17), when $\mu\to0$, are

$$A_3+a_2\dot{\mathrm{Z}}=C_4\sin\phi-C_5\cos\phi,$$
$$B_3-na_2\mathrm{Z}=C_4\cos\phi+C_5\sin\phi,$$

where C_4 and C_5 are constants of integration.

Hence

$$(\xi_3\dot{\zeta}_3-\zeta_3\dot{\xi}_3)+n\zeta_3\eta_3=C_4\sin\phi-C_5\cos\phi-a_2\dot{Z}, \tag{16'}$$

$$(\eta_3\dot{\zeta}_3-\zeta_3\dot{\eta}_3)-n\zeta_3\xi_3=C_4\cos\phi+C_5\sin\phi+na_2Z. \tag{17'}$$

(It may be noted in passing that the elimination of the unknown functions Z and $\dot{Z}$ by taking $[d/dt(17')+n(16')]$ yields an identity.)

4. *The unknown functions of time.*—Let us now consider the nature and behaviour of the time-dependent functions ${}^1\Xi_i$, ${}^1H_i$, ${}^1Z_i$ and their derivatives. These functions must be discussed by first considering the three-body problem with finite m_3, and then allowing μ to tend to zero.

At $t=0$, by definition, m_1 and m_2 are distant a_1 and a_2 from G' (their common centre of gravity). Therefore, at $t=0$, the true ξ-coordinates of m_1 and m_2 (i.e. with respect to G as origin) will be $(a_1+\xi_{G'})$ and $(-a_2+\xi_{G'})$ respectively, where $\xi_{G'}$ is the ξ-coordinate of G'. Hence, *at* $t=0$, we have $\xi_{11}=\xi_{G'}=\xi_{21}$. Letting $\mu\to 0$, we have

$${}^1\Xi_1=\frac{1}{\mu}\xi_{G'}={}^1\Xi_2. \tag{18}$$

But, from (9),

$$\xi_3=-\frac{1}{\mu}\left[\frac{1}{\alpha}(\alpha a_2+\xi_{11})+(-a_2+\xi_{21})\right]$$

which becomes, as $\mu\to 0$,

$$\xi_3=-\left(\frac{1}{\alpha}{}^1\Xi_1+{}^1\Xi_2\right). \tag{19}$$

Putting (18) in (19), we have

$${}^1\Xi_1={}^1\Xi_2=-\frac{\xi_3\alpha}{(1+\alpha)} \tag{20}$$

and

$$\Xi=0 \tag{21}$$

with analogous expressions for $\dot{\Xi}$, H, $\dot{H}$, Z and $\dot{Z}$. Thus the unknown functions can be calculated *for* $t=0$ if the position and velocity of the infinitesimal particle at $t=0$ are known.

We now consider the situation at some later time $t=t'$ of the system with finite m_3 which started at $t=0$ in the manner already defined. At $t=t'$, we write, as before, $\xi_1=\alpha a_2+\xi_{11}$, $\xi_2=-a_2+\xi_{21}$. However, we must now, in general, write

$$\xi_{11}\neq\xi_{21} \tag{22}$$

because the values of ξ_1 and ξ_2 are different from αa_2 and $-a_2$, respectively, not only because of a separation between G and G', but also because (*a*) the line $m_2G'm_1$ may be no longer parallel to the ξ-axis, and (*b*) the distance between m_1 and m_2 may be no longer (a_1+a_2). Therefore, on letting $\mu\to 0$ in the inequality (22), we find

$${}^1\Xi_1\neq{}^1\Xi_2, \quad \text{and} \quad \Xi\neq 0.$$

Therefore, even in the case of infinitesimal m_3, equations (20) and (21) are applicable *only at the instant chosen as* $t=0$.

Since in the case of infinitesimal m_3 the two massive bodies m_1 and m_2 are moving in strictly circular orbits, any phase of the motion of the system for which ξ_3 is known may be chosen as $t=0$. However, once the instant $t=0$ has

been defined, the subsequent variations of ${}^1\Xi_1$, ${}^1\Xi_2$ and Ξ are unknown. It is seen that similar arguments apply to the H and Z functions, and to the derivatives.

Therefore, although the constants of the angular momentum equations (15), (16′) and (17′) may be evaluated for the initial conditions (at $t=0$), the fact that the Ξ, H and Z functions change with time in an unknown manner precludes our using these equations to obtain any information about the behaviour of the infinitesimal particle at times after $t=0$.

5. *Derivation of the integrals of the elliptical restricted three-body problem.*—We now take the initial position of the axes $G\xi\eta\zeta$, at $t=0$, as follows: $G\xi$ is taken parallel to the line $m_2G'm_1$. The $\xi\eta$-plane is taken parallel to the plane through $m_2G'm_1$ containing the instantaneous velocity vector of m_1. At $t=0$ we let $G'm_1=\rho_1=\alpha\rho_2$ and $G'm_2=\rho_2$. We also assume that at $t=0$ the velocity vectors of the two bodies m_1 and m_2 are the velocity vectors they would have if they were to move, in the absence of m_3, about G' in ellipses of eccentricity e and major semi-axes a_1 $(=\alpha a_2)$ and a_2. Thus the instantaneous velocity vector of m_2 will be parallel to the plane $\xi\eta$. We now suppose that the axes $G\xi$ and $G\eta$ rotate about $G\zeta$ with a variable angular velocity $\dot\phi$ such that at any time t, $\dot\phi=\dot\theta$; that is

$$\dot\phi^2=\frac{(m_1+m_2)}{(\rho_1+\rho_2)^3}(1+e\cos\theta) \tag{23}$$

where

$$\rho_1=\alpha\rho_2=\frac{\alpha a_2(1-e^2)}{1+e\cos\theta}.$$

In this expression θ is the true anomaly of either m_1 or m_2 at time t (*in the absence of* m_3).

At any time t, and for $\mu\neq 0$, let

$$\begin{aligned}
\xi_1&=\alpha\rho_2+\xi'_{11}, & \xi_2&=-\rho_2+\xi'_{21},\\
\dot\xi_1&=\alpha\dot\rho_2+\dot\xi'_{11}, & \dot\xi_2&=-\dot\rho_2+\dot\xi'_{21},\\
\eta_1&= \quad \eta'_{11}, & \eta_2&= \quad \eta'_{21},\\
\zeta_1&= \quad \zeta'_{11}, & \zeta_2&= \quad \zeta'_{21},
\end{aligned}$$

where $(\xi',\eta',\zeta')_{11,21}$ and $(\dot\xi',\dot\eta',\dot\zeta')_{11,21}$ tend to zero as μ tends to zero, but are not necessarily zero at $t=0$ if μ does not equal zero.

Then, as in the circular case, and by the same theorem, we may write

$$\xi'_{i1}=\sum_{p=1}^{\infty}{}^p\Xi'_i(t)\mu^p, \quad \text{etc.} \qquad (i=1,2).$$

We treat equation (6) first.

We have

$$m_3\frac{d\omega_\zeta}{dt}=-\frac{d}{dt}\left\{\sum_{1,2}m_i[(\eta_i\dot\xi_i-\xi_i\dot\eta_i)-\dot\phi(\xi_i^2+\eta_i^2)]\right\}$$

where we have written

$$\omega_\zeta=(\eta_3\dot\xi_3-\xi_3\dot\eta_3)-\dot\phi(\xi_3^2+\eta_3^2).$$

Then

$$\begin{aligned}
m_3\frac{d\omega_\zeta}{dt}=-\frac{d}{dt}\{&m_1[\eta_{11}\dot\rho_1-\rho_1\dot\eta_{11}-\dot\phi(\rho_1^2+2\rho_1\xi_{11})]\\
&+m_2[-\eta_{21}\dot\rho_2+\rho_2\dot\eta_{21}-\dot\phi(\rho_2^2-2\rho_2\xi_{21})]+O(\mu^2)\}.
\end{aligned}$$

Using the above expansions and the relations

$$m_1\rho_1 = m_2\rho_2 = \frac{m_1m_2}{m_1+m_2}(\rho_1+\rho_2); \qquad m_1\dot{\rho}_1 = m_2\dot{\rho}_2 = \frac{m_1m_2}{m_1+m_2}(\dot{\rho}_1+\dot{\rho}_2), \tag{24}$$

we obtain, on writing $\Xi' = {}^1\Xi'_1 - {}^1\Xi'_2$, etc.,

$$m_3\frac{d\omega_\zeta}{dt} = \frac{d}{dt}\{m_1\rho_1\dot{\phi}(\rho_1+\rho_2) - \mu m_1[\dot{\rho}_1\mathrm{H}' - \rho_1(\dot{\mathrm{H}}' + 2\dot{\phi}\Xi')] + O(\mu^2)\}.$$

Now write $\rho = \rho_1+\rho_2$. Then we have the following two-body relationships, as are obtained by putting $\mu = 0$ in equations (2), (3) and (4), and using the initial conditions specified above:

$$\ddot{\rho} - \rho\dot{\phi}^2 = -\frac{m_1+m_2}{\rho^2}; \qquad \rho^2\dot{\phi} = h, \qquad \rho^2\ddot{\phi} + 2\rho\dot{\rho}\dot{\phi} = 0. \tag{25}$$

It is seen that

$$\frac{d}{dt}[m_1\rho_1\dot{\phi}(\rho_1+\rho_2)] = \frac{d}{dt}\left[\frac{m_1m_2}{m_1+m_2}\rho^2\dot{\phi}\right] = 0.$$

Hence we obtain, on dividing through by m_3, integrating, and letting $\mu \to 0$,

$$(\eta_3\dot{\xi}_3 - \xi_3\dot{\eta}_3) - \dot{\phi}(\xi_3^2+\eta_3^2) + \frac{1}{\alpha}\dot{\rho}_1\mathrm{H}' - \rho_1(\dot{\mathrm{H}}' + 2\dot{\phi}\Xi') = C''', \tag{26}$$

where C''' is a constant of integration.

Writing $V' = m_1/r_{13} + m_2/r_{23}$, $J' = v^2 - \dot{\phi}^2R^2 - 2V'$ where

$$v^2 = \sum_{\xi\eta\zeta}\dot{\xi}_3^2 \quad \text{and} \quad R^2 = \xi_3^2+\eta_3^2,$$

we have from (5)

$$m_3\frac{dJ'}{dt} = \frac{d}{dt}\left\{-\sum_{1,2}m_i(v_1^2 - \dot{\phi}^2R_i^2) + \frac{2m_1m_2}{r_{12}} + 2C_3\dot{\phi}\right\}.$$

Now

$$\frac{d}{dt}\left(-\sum_{1,2}m_iv_i^2\right) = -\frac{d}{dt}[m_1(\dot{\rho}_1^2 + 2\mu\dot{\rho}_1\,{}^1\dot{\Xi}'_1) + m_2(\dot{\rho}_2^2 - 2\mu\dot{\rho}_2\,{}^1\dot{\Xi}'_2) + O(\mu^2)].$$

Also

$$\frac{d}{dt}\left(\dot{\phi}^2\sum_{1,2}m_iR_i^2\right) = \frac{d}{dt}\{\dot{\phi}^2[m_1(\rho_1^2 + 2\mu\rho_1\,{}^1\Xi'_1) + m_2(\rho_2^2 - 2\mu\rho_2\,{}^1\Xi'_2) + O(\mu^2)]\}.$$

Again,

$$\frac{d}{dt}\left(\frac{2m_1m_2}{r_{12}}\right) = 2m_1m_2\frac{d}{dt}\left\{\frac{1}{\rho_1+\rho_2} - \mu\frac{{}^1\Xi'_1 - {}^1\Xi'_2}{(\rho_1+\rho_2)^2} + O(\mu^2)\right\}.$$

$$\frac{d}{dt}(C_3\dot{\phi}) = \frac{d}{dt}\left\{\dot{\phi}m_3[(\eta_3\dot{\xi}_3 - \xi_3\dot{\eta}_3) - \dot{\phi}(\xi_3^2+\eta_3^2)] + \dot{\phi}\sum_{1,2}m_i[(\eta_i\dot{\xi}_i - \xi_i\dot{\eta}_i) - \dot{\phi}(\xi_i^2+\eta_i^2)]\right\},$$

$$= \frac{d}{dt}\{\dot{\phi}[C'''m_3 - m_1\rho_1\dot{\phi}(\rho_1+\rho_2) + o(\mu^2)]\},$$

using (26). Hence we have

$$m_3\frac{dJ'}{dt} = \frac{d}{dt}\left\{E + 2m_3\dot{\phi}C''' - 2\mu\left[m_1\dot{\rho}_1\dot{\Xi}' - \dot{\phi}^2m_1\rho_1\Xi' + \frac{m_1m_2}{\rho^2}\Xi'\right] + O(\mu^2)\right\},$$

where

$$E = -m_1\dot{\rho}_1^2 - m_2\dot{\rho}_2^2 + \dot{\phi}^2(m_1\rho_1^2 + m_2\rho_2^2) + \frac{2m_1m_2}{\rho} - 2m_1\rho_1\rho\dot{\phi}^2.$$

Then, using (24), we have

$$E = -\frac{m_1 m_2}{m_1+m_2}\left[\dot\rho^2+\rho^2\dot\phi^2-\frac{2(m_1+m_2)}{\rho}\right].$$

Hence, using (25) it is seen that $dE/dt = 0$.

Therefore we obtain, on dividing by m_3,

$$\frac{dJ'}{dt} = \frac{d}{dt}\left\{2\dot\phi C''' - \frac{2}{\alpha}\left[\dot\rho_1\dot\Xi' - \dot\phi^2\rho_1\Xi' + \frac{m_2}{\rho^2}\Xi'\right] + O(\mu)\right\}.$$

Integrating and letting $\mu\to 0$, we obtain finally

$$(\dot\xi_3^2+\dot\eta_3^2+\dot\zeta_3^2) - \dot\phi^2(\xi_3^2+\eta_3^2) - \left(\frac{m_1}{r_{13}}+\frac{m_2}{r_{23}}\right) - 2\dot\phi C''' + \frac{2}{\alpha}\left[\dot\rho_1\dot\Xi' - \dot\phi^2\rho_1\Xi' + \frac{m_2}{\rho^2}\Xi'\right] = \kappa',$$

where κ' is a constant of integration.

Equations (7) and (8) may be treated in the same manner to obtain two further integrals.

We may now, without loss of generality, assume that $\phi = 0$ when $\theta = 0$. This is equivalent to the assumption that (μ now being infinitesimal) the x-axis of our original Galilean frame lies along the apse-line of the relative orbit of m_1 and m_2, from G in the direction of pericentron of m_1. (The xy-plane is, of course, the plane of the relative orbit of m_1 and m_2.)

Using (23) we may re-write the four integrals as follows:

$$(\dot\xi_3^2+\dot\eta_3^2+\dot\zeta_3^2) - \dot\theta^2(\xi_3^2+\eta_3^2) - 2\left(\frac{m_1}{r_{13}}+\frac{m_2}{r_{23}}\right) - 2C'''\theta + \frac{2e}{1+\alpha}\left(\sqrt{\frac{m_1}{a_2(1-e^2)}}\right)\sin^2\theta\,\frac{d}{dt}\left(\frac{\Xi'}{\sin\theta}\right) = \kappa', \tag{27}$$

$$(\eta_3\dot\xi_3 - \xi_3\dot\eta_3) - \dot\theta(\xi_3^2+\eta_3^2) - \frac{a_2(1-e^2)}{(1+e\cos\theta)^2}\left[\dot{\mathrm{H}}' + e\frac{d}{dt}(\mathrm{H}'\cos\theta)\right] - \frac{2(1+e\cos\theta)}{1+\alpha}\left(\sqrt{\frac{m_1}{a_2(1-e^2)}}\right)\Xi' = C''', \tag{28}$$

$$(\xi_3\dot\zeta_3 - \zeta_3\dot\xi_3) + \dot\theta\zeta_3\eta_3 + \frac{a_2(1-e^2)}{(1+e\cos\theta)^2}\left[\dot{\mathrm{Z}}' + e\frac{d}{dt}(\mathrm{Z}'\cos\theta)\right] = C_4'\sin\theta - C_5'\cos\theta, \tag{29}$$

$$(\eta_3\dot\zeta_3 - \zeta_3\dot\eta_3) - \dot\theta\zeta_3\xi_3 - \frac{(1+e\cos\theta)}{1+\alpha}\left(\sqrt{\frac{m_1}{a_2(1-e^2)}}\right)\mathrm{Z}' = C_4'\cos\theta + C_4'\sin\theta, \tag{30}$$

where $\mathrm{Z}' = {}^1\mathrm{Z}_1' - {}^1\mathrm{Z}_2'$, etc.

The following convenient transformations may now be employed. Let the functions L', F' and S' be defined by the expressions

$$L' = \dot\rho\mathrm{H}' - \rho(\dot{\mathrm{H}}' + 2\dot\theta\Xi'),$$

$$F' = \sin^2\theta\,\frac{d}{dt}\left(\frac{\Xi'}{\sin\theta}\right),$$

$$S' = -\frac{h}{(1+\alpha)}\left(\frac{\mathrm{Z}'}{\rho}\right) - (C_4'\cos\theta + C_5'\sin\theta),$$

where $\rho=\rho_1+\rho_2$ and $h^2=(m_1+m_2)a(1-e^2)$. The equations of motion of the particle are:

$$\ddot{\xi}-2\dot{\theta}\dot{\eta}-\dot{\theta}^2\xi-\ddot{\theta}\eta=-m_1\left[\xi\left(\frac{1}{r_1^3}+\frac{\alpha}{r_2^3}\right)-\rho_1\left(\frac{1}{r_1^3}-\frac{1}{r_2^3}\right)\right], \tag{31}$$

$$\ddot{\eta}+2\dot{\theta}\dot{\xi}-\dot{\theta}^2\eta+\ddot{\theta}\xi=-m_1\eta\left(\frac{1}{r_1^3}+\frac{\alpha}{r_2^3}\right), \tag{32}$$

$$\ddot{\zeta}=-m_1\zeta\left(\frac{1}{r_1^3}+\frac{\alpha}{r_2^3}\right). \tag{33}$$

Here, the suffix "3" referring to the coordinates of the infinitesimal body is dropped, to conform with common practice, although it must be remembered that the ξ, η, ζ coordinates are referred to non-uniformly rotating axes.

Using the above transformations, equations (27), (28), (30) and (29) become, respectively,

$$(\dot{\xi}^2+\dot{\eta}^2+\dot{\zeta}^2)-\dot{\theta}^2(\xi^2+\eta^2)-2\left[\frac{m_1}{r_1}+\frac{m_2}{r_2}\right]+\frac{2e(m_1+m_2)}{h(1+\alpha)}F'=\kappa'+2C'''\dot{\theta}, \tag{34}$$

$$(\eta\dot{\xi}-\xi\dot{\eta})-\dot{\theta}(\xi^2+\eta^2)+\frac{L'}{(1+\alpha)}=C''', \tag{35}$$

$$(\zeta\dot{\eta}-\eta\dot{\zeta})+\dot{\theta}(\zeta\xi)-S'=0 \tag{36}$$

and

$$\dot{S}'=\dot{\theta}[(\xi\dot{\zeta}-\zeta\dot{\xi})+\theta(\zeta\eta)]. \tag{37}$$

Again, differentiating equations (34) and (35), we obtain, after some reduction,

$$\dot{F}'=\left[m_2\xi\left(\frac{1}{r_1^3}-\frac{1}{r_2^3}\right)-m_2\rho_2\left(\frac{\alpha}{r_1^3}+\frac{1}{r_2^3}\right)-\frac{2hL'}{\rho^3}\right]\sin\theta \tag{38}$$

and

$$\dot{L}'=-m_2\rho\eta\left(\frac{1}{r_1^3}-\frac{1}{r_2^3}\right). \tag{39}$$

6. *The unknown functions of time in the elliptical problem.*—The discussion of the behaviour of the unknown functions of time in the circular problem (Section 4), in particular equations (19), (20) and (21) and the inequality (22), applies, *mutatis mutandis*, to the primed functions of the elliptical problem. It may be re-emphasized here that the existence of significant values for any of these functions does not imply any sensible departure of the two massive bodies from their elliptical motion since, to obtain the actual displacements of the massive bodies, these functions have to be multiplied by μ, which becomes infinitesimal.

It should be noted that although the function F' may be taken to be zero at $t=0$, in general it is finite and of zero order in "e". In the corresponding circular case, F' becomes F, a function which is in general not zero (except at $t=0$), whose behaviour is given by equation (38), but which does not appear in the circular Jacobi because it has zero coefficient there.

The assumption that the circular Jacobi is an approximation (to order "e") to the elliptic Jacobi for arbitrarily long times is equivalent to supposing that the elliptic Jacobi "constant" $\kappa_e=\kappa(1+eA)$, where

$$\kappa_e=\kappa'+2C'''\dot{\theta}-[2e(m_1+m_2)/h(1+\alpha)]F',$$

and A is a time-dependent variable of order not greater than unity. Putting $e=0$ in equation (34) we find $\kappa=\kappa'+2nC'''$, i.e.

$$A=\frac{2(\dot\theta-n)C'''}{e\kappa}-\frac{2(m_1+m_2)}{h(1+\alpha)\kappa}F'.$$

While the first term is certainly always of order unity, or less, in the absence of any knowledge of F' the assumption that the second term remains of order unity or less is unwarranted.

Indeed, from the strictly rigorous standpoint, there is no more justification for ignoring the changes of the unknown functions in the Jacobi integral (34) than there is for ignoring them in the angular momentum integrals (35), (36) and (37). Perhaps for a sufficiently short time, variations of these functions might be neglected, and since in equation (34) the function F' appears only in a term with coefficient "e", it might be expected that (34) without the term involving F' would be approximately valid for a longer time than the angular momentum equations, similarly truncated. But no estimates of this time are known to the authors. (We might expect to be able to use the truncated Jacobi for a time of the order of $1/e$ times as long as the truncated angular momentum equations for a given accuracy.)

7. *Long-term predictions.*—Let us now consider what conclusions, if any, may be drawn from equation (34) that are true for any arbitrarily long time (on the assumption that μ is arbitrarily small). We suppose that we have a system for which, at $t=0$, we know the masses and the configuration of positions and velocities for the two massive bodies and the particle; i.e. we know m_1, α, a and e. Then the constants κ' and C''' may be evaluated from equations (34) and (35) by using the initial conditions, since, at $t=0$, the functions L' and F' may be taken to be zero. Since the velocity of the particle cannot be imaginary, we may write, from (34),

$$(\dot\xi^2+\dot\eta^2+\dot\zeta^2)=\dot\theta^2(\xi^2+\eta^2)+2\left[\frac{m_1}{r_1}+\frac{m_2}{r_2}\right]+\kappa'+2\dot\theta C'''+\lambda F'\geqslant 0$$

where $\lambda=-2e(m_1+m_2)/h(1+\alpha)$, a constant.

If, at any time other than $t=0$, we knew the value of F', without knowing the position of the particle, we could conclude that the particle must, at that time, be situated in that region of space corresponding to a real velocity, whose limits are defined by a surface of zero velocity

$$\dot\theta^2(\xi^2+\eta^2)+2\left[\frac{m_1}{r_1}+\frac{m_2}{r_2}\right]+\kappa'+2\dot\theta C'''+\lambda F'=0. \tag{40}$$

This surface of zero velocity varies its shape and size with time as (i) $\dot\theta$ and ρ vary, and (ii) F' varies. Equation (40) becomes, for $t=0$,

$$\dot\theta^2(\xi^2+\eta^2)+2\left[\frac{m_1}{r_1}+\frac{m_2}{r_2}\right]+\kappa'+2\dot\theta C'''=0 \tag{41}$$

which differs from the circular Jacobi in form only to the extent to which $\dot\theta$ differs from n and ρ differs from a. The true surface, given by (40), departs from that given by (41) as F' varies. It can be seen that (i) the infinitesimal particle can only be on that surface of zero velocity appropriate to the values of κ' and C''' (determined by the initial conditions) and F' at that time, when the surface itself is stationary, and (ii) the particle cannot cross the (varying) surface of zero velocity.

It must be emphasized that the surface, with its changes, is characteristic of the particle, since, in general, the function F' which influences the behaviour of the surface is a function of time through the coordinates of the particle. This is in contrast with the circular Jacobi where any particle with a given Jacobi constant has the same surface of zero velocity.

But in practice it is not known how to express F' in terms of the initial conditions of the particle and of the time explicitly, so that no information of the way in which F' changes with time is available. Therefore no conclusions true for arbitrarily long times may be drawn from equation (34) even if μ is arbitrarily small, unless other information is available about the behaviour with time of F'. Since the only known explicit expression for F' in terms of the coordinates and velocity of the infinitesimal particle is the elliptical Jacobi equation (34), even if the orbit of the particle is known, equation (34) gives no additional information. But in any case, if the orbit of the particle is known, equation (34) is redundant.

Summing up, we may say that while the initial conditions enable one to draw a surface of zero velocity at $t=0$ (which surface, if e is very small, will be similar to the corresponding surface of zero velocity in the circular case) they do not enable one to identify the appropriate surface of zero velocity for any time after $t=0$.

As an illustration, suppose that the configuration (positions and velocities) of a system of two massive bodies moving in an ellipse of small eccentricity and an infinitesimal particle is noted by an observer at a time taken to be $t=0$. The observer uses the circular Jacobi (equation (14)) to calculate a surface of zero velocity. This surface is correct for $t=0$, apart from a discrepancy of order "e" due to the particular values of θ and ρ, which depend upon the true anomaly of the massive bodies at $t=0$. The observer now leaves the system, and then returns at some later time t_1. Using the circular Jacobi again, and the new configuration of the system, he calculates what he believes to be the new surface of zero velocity for the same particle. Should it happen that this second surface of zero velocity is greatly different from the previous one, the observer would conclude that in his absence the system had been interfered with. This conclusion may be erroneous, the difference between the two surfaces of zero velocity being due to the change of F' in the interval from $t=0$ to $t=t_1$. If, on the other hand, the two surfaces are almost or exactly identical, the observer would conclude that the particle could not, in his absence, have wandered outside the "fixed" surface. This conclusion, too, may be erroneous, since the surface of zero velocity appropriate to the particle may have expanded and contracted during his absence due to the behaviour of F'.

We have mentioned that Hill, in his celebrated lunar theory (**5**), qualified his statement that the Moon's distance from the Earth has a superior limit. This limit he obtained from the value of the Jacobi constant in the case Sun–Earth–Moon, treating the Moon as an infinitesimal body and neglecting the eccentricity of the Earth's orbit. His actual words were "Thus, the eccentricity of the Earth's orbit being neglected, we have a rigorous demonstration of a superior limit to the radius vector of the Moon". He went on to obtain the actual motion of the Moon from an intermediate orbit (a periodic solution of the circular restricted three-body problem), finding that it differed from the intermediate orbit by small periodic terms and small empirical secular terms.

XUM

His statement about the Moon's superior limit is equivalent to a statement that the function F' is periodic and of small amplitude and is without any secular terms. But since this information about F' could have been obtained only from his independent investigation of the Moon's motion, he really obtained no rigorous information from the use of the circular Jacobi.

Similarly, Hagihara (**7**), in applying the circular Jacobi to the other satellites of the solar system, could only be rigorous in his conclusions if he knew that F' was periodic without secular terms. But this is known only if the natures of the satellite orbits are known for all time, so that no additional information is obtained in this way by applying the circular Jacobi.

In his investigation of the origin of the satellites and the Trojans, Kuiper (**6**) points out, with respect to the asteroids, that beyond $a=4{\cdot}0$ A.U., one finds only Thule ($a=4{\cdot}28$), 13 Trojans ($5{\cdot}10 \leqslant a \leqslant 5{\cdot}27$) and Hidalgo ($a=5{\cdot}79$). He states that "... the limit near $a=4{\cdot}0$ has an important dynamical meaning. For smaller 'a' values and small or moderate eccentricities and inclinations the Jacobian constants of the three-body system Sun–Jupiter–Asteroid are such that the asteroids must for ever stay within the solar oval of the Hill surface of zero velocity defined by the finite masses of the Sun and Jupiter and passing through the Lagrangian point L_1. Conversely, they must have been in that oval ever since the mass of Jupiter stabilized to the present value, a few hundred million years after Jupiter was formed". And again: "The Trojans cannot have formed in the asteroid belt; if they had, they would still be there". Thus Kuiper, using the circular Jacobi, is forced to state that the Trojans, Hidalgo and possibly Thule cannot ever have been within $a=4{\cdot}0$ A.U. From the point of view of the present paper, these conclusions cannot be drawn.

Kuiper then uses the circular Jacobi to "prove" that a body near Jupiter could not have become a Trojan if the mass of Jupiter had remained constant, and goes on: "Since this is a rigorous result it is of great importance; this leaves only the possibility that the Trojans got their position because of the decreasing mass of Jupiter".

According to the views of the present authors, Kuiper is in the position of the observer mentioned earlier in this section, who, using the circular Jacobi to calculate surfaces of zero velocity for two epochs for the same particle, finds them widely different and assumes that the system has been interfered with. He chooses a diminution of mass as the interfering process, an unjustified assumption in the light of the present section's arguments.

In conclusion, then, we may say that the use of the Jacobi integral of the circular restricted three-body problem for long-term predictions in any real case where the two massive bodies' relative orbit has a finite eccentricity (however small) is without justification even if the mass of the third body is infinitesimal.

Our thanks are due to a referee for suggesting an improvement in the method of presentation of part of this paper.

Dept. of Astronomy,
University of Glasgow:
1960 *October* 10.

XUM

References

(1) C. G. J. Jacobi, *Compte Rendus de l'Acad. des Sciences*, Paris, III, 59, 1836.
(2) H. Bruns, *Acta Mathem.*, XI, 25, 1887–88.
(3) H. Poincaré, *Les Méthodes Nouvelles de la Mécanique Céleste*, I, Chap. V, Paris 1892.
(4) M. O. Callandreau, *Ann. Obs. Paris, Memoires XX*, B.29, 1892.
(5) G. W. Hill, *Coll. Math. Works*, Vol. I, 284, Washington 1905.
(6) G. P. Kuiper, *Vistas in Astronomy*, Vol. 2, 1631, London 1956.
(7) Y. Hagihara, *Proc. Japan Acad.*, **28**, 182, 1952.
(8) Z. Kopal, *Ann. Astrophys.*, **19**, Part 6, 1956.
(9) S-S. Huang, *P.A.S.P.*, **72**, 106, 1960.
(10) V. A. Egorov, VIIIth Int. Astronaut. Cong., Barcelona 1957, Proc. 480, Wien 1958.
(11) W. M. Smart, *Celestial Mechanics*, London 1953.
(12) F. R. Moulton, *An Introduction to Celestial Mechanics*, 2nd Edition, New York 1914.
(13) F. R. Moulton, *Periodic Orbits*, Carnegie Inst. Publ., Washington, 1920.

XUM

SMALL-SCALE EXPLOSION CRATERS, IMPACT CRATERS, AND THE PHYSICAL STRUCTURE OF THE MOON'S SURFACE

*Gilbert Fielder**

(Received 1961 March 10)

Summary

A comparison of the forms of experimental explosion craters and the observed forms of lunar craters leads to the conclusion that parts of the Moon may be covered with a layer of material, having the physical properties of a gravel, to a depth of between 0·3 km and 1–3 km. Predictions are given for the variation of the ratio of the depth of a crater to its diameter, as the diameter varies, for likely models of the Moon's surface layers, and an elementary but critical type of lunar observation, which may be of great assistance in the identification of the broad physical nature of these layers at different points on the Moon, is described.

Both explosion-experiments, and experiments involving non-explosives, indicate that the lunar rays were ejected from craters at relatively low angles, and that the rays probably consist of small, secondary craters and many more small, bright particles. The primary ray-craters were probably produced by near-surface meteoritic impacts in which explosive-type violence and crushing both played parts. In the small secondary craters, with velocities only ~ 1 km sec^{-1}, crushing would predominate, and this hypothesis is supported by the fact that the rays extending from these small craters are unidirectional.

Conditions for dome-formation are stipulated. If domes and conical craters are found to occur together on the Moon, then the domes are probably igneous phenomena rather than the surface effects of camouflets.

Experimental conditions required for the formation of craters with central eminences are described, and photographs of bomb craters and explosion craters in lead are compared with the lunar craters. Both small-scale and lunar-size craters often display approximately radial patterns outside their walls, and these patterns indicate that the stresses associated with their formation were of similar type and distribution on the two different scales.

---

1. *Nature of experiments.*—Laboratory experiments which attempt to imitate large scale craters in solid rock should be performed in materials which have only little tensile strength; for, with the large energies involved in the formation of meteoritic impact craters, the materials would be shattered irrespective of their compositions and hence their actual tensile strengths would play but minor roles in the determination of the forms of the resulting craters. The use of such materials in small-scale experiments also ensures that reproducibility may best be obtained. For these reasons, and for reasons of availability, experiments were conducted with the media listed in Table 1. The angles of repose are

* Imperial Chemical Industries Research Fellow of the University of London.

approximate values of the maximum slope of a heap of loose material. The maximum slopes observed in the case of Shelbux were only 35° but, exceptionally, angles of up to 90° were obtained with the powders. As there are good reasons for supposing that there is much finely granulated rock at certain points on the Moon, these materials might not, in fact, differ very greatly in their physical properties from parts of the Moon's surface. In making the comparison with

TABLE I

Material	Angle of repose
Kieselguhr (diatomaceous earth)	45°
Limbux (hydrated limestone)	45°
Limbux slurry (Limbux and water, forming a thixotropic mix)	any value
Baribux (waterproofed limestone powder)	45°
Shelbux (chickengrit)	40°

lunar-sized craters, any scaling effects which would arise as a consequence of the weight of the overlying rocks on the Moon will be disregarded; but this assumption is thought to be reasonable in view of the fact that depths of the order of only a kilometre will be considered.

The explosives used in these experiments were charges A and B, details of which are provided in Table II. The gelignite, in charge B, was always moulded to the shape of a sphere with its centre in the base charge of the detonator; but Schlieren photographs showed that, even when a detonator was used alone (charge A), the explosion was propagated with roughly spherical symmetry.

TABLE II

Charge	Description	Approx. energy released (ergs).
A	I.C.I. No. 6 copper-cased instantaneous electric detonators	$4{\cdot}2 \times 10^{10}$
B	Charge A used to fire 2·5 gm of blasting gelatine	$1{\cdot}5 \times 10^{11}$

Experiments were first performed with charges A fired at various "focal depths" in a receptacle holding six cubic feet (0·17 m^3) of each of the materials listed in Table I, in turn, and the shapes of the resulting formations were studied. The depths, δ, of craters were measured from the average level of the tops of their ringwalls to the lowest parts (the centres) of their floors, and mean diameters, Δ, were estimated between the crests of the walls.

Similar experiments were performed by exploding charges B in a receptacle containing three tons of Baribux—a medium which was selected from the others for purely practical reasons. Cine films of these explosions were taken through a rectangular aperture in one of the walls of the explosion shelter, in order to investigate the patterns (end elevations) of each set of ejected particles.

2. *Dependence of crater form on depth of explosion, energy of explosive, and physical nature of the medium.*—In general, with an explosive of given energy fired at a small focal depth, a crater was formed but, at larger focal depths, this crater was replaced by large numbers of small domes and small craters. However, different materials sometimes behaved differently when considered in detail.

Plots of the diameters and depths of craters against $\mathscr{F}$, the proportional focal depths per unit of energy, are shown in Figs. 1 (*a*) and 1 (*b*), respectively. These

plots show that four of the materials* listed in Table I could be grouped together to form curves 1, the curves for Shelbux (curves 2) differing radically from them. The differences between curves 1 and 2 is due to the fact that the relative volume of the interstices of the Shelbux is very much greater than in the cases of the other materials, and that the angle of repose of Shelbux is less than the angles of repose of the other materials. The *final* shape of a crater formed in Shelbux differs from that shape which is produced instantaneously, by the explosive, in a manner which is more marked than in the cases of the other media. It should be noted that the final shape which a crater assumes depends mostly on its surface properties, and that these properties are not dependent on scaling factors such as the change of the physical properties of a medium with increasing depth. A gravel on the Moon would behave in a similar way to the gravel used in the experiments, whereas solid rock on the Moon might be expected to behave in a similar way to the dusty media of these experiments. That a gravelly material on the Moon might be expected to yield craters so different from those produced in solid rock, or in cohering dust, is interesting.

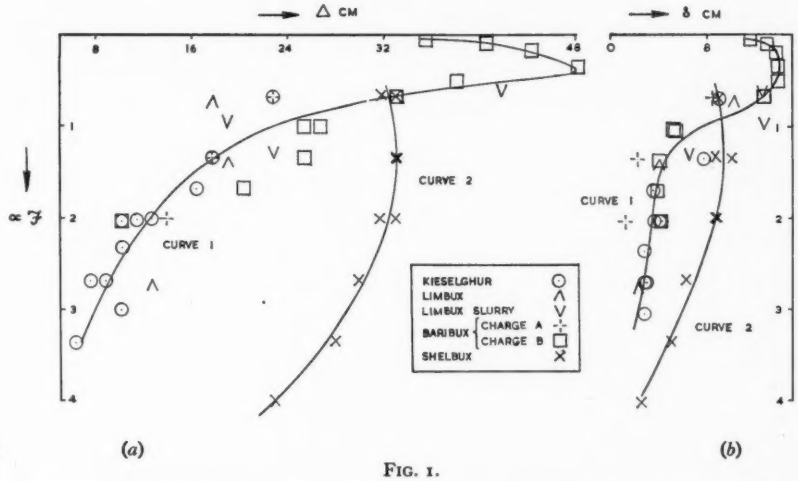

FIG. 1.

The $\Delta - \mathscr{F}$ and $\delta - \mathscr{F}$ curves show maxima values of Δ and δ, respectively. These maxima occur at what will be termed "critical" values, $\mathscr{F} = \mathscr{F}_c$. In general, the explosive dissipates its energy in two media: the medium in which the crater is formed, and the air above the upper horizontal plane bounding that medium. With $\mathscr{F} \gg \mathscr{F}_c$, the solid medium absorbs virtually all the energy of the explosive. As $\mathscr{F} \to 0$ over the range $\mathscr{F}_c > \mathscr{F} > 0$, an increasingly larger proportion of the total energy available is transferred to the air. For an explosive of given energy, the critical focal depth is that smallest focal depth at which the solid medium absorbs the maximum amount of energy. With an explosion centred at $\mathscr{F}_c$, the volume of a crater in a particular medium assumes a maximum value. (Baldwin (1) found similar relationships for other explosion craters but for these δ_{max} occurred at a smaller value of the focal depth than did Δ_{max}). The value of $\mathscr{F}_c$ was found to be greater in the coarser (more porous) of the

* For identification marks, see Fig. 1.

materials used (cf. Fig. 1). Estimates indicated that the volume of a crater formed in any of the media was directly proportional to the energy of the explosive only when the explosion was centred at $\mathscr{F}_c$.

3. *Application of results to the Moon.*—At what depths and in what types of media did the explosions which produces the lunar craters occur ? Gold (**2**) has reasoned that meteorites impinging with the Moon would initiate explosions before they had penetrated more than a very few diameters, and Gilvarry and Hill (**3**) have shown theoretically that large meteorites would explode within a penetrative distance of about two diameters. The diameters of the present explosives were of the order of magnitude of the critical focal depths; so it seems reasonable to assume that the results most relevant to the study of the formation of meteoritic craters are contained in those parts of the curves defined by $\mathscr{F} \sim \mathscr{F}_c$.

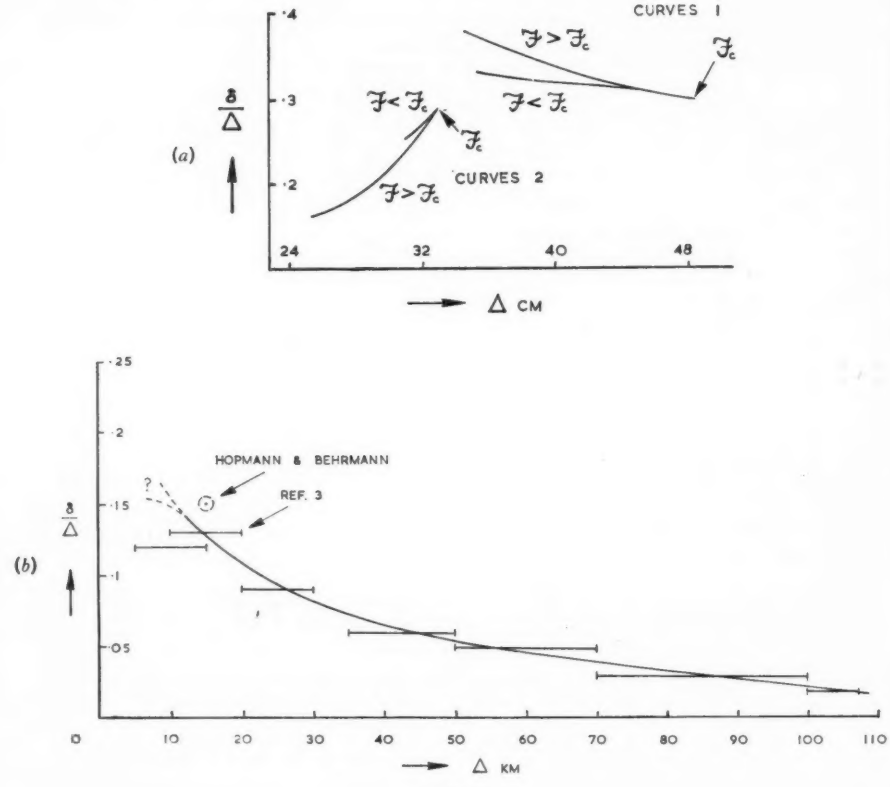

FIG. 2.

The smoothed $\delta/\Delta - \Delta$ relationship (Fig. 2*a*) for the experimental craters formed at values of $\mathscr{F}$ in the vicinity of $\mathscr{F}_c$ shows that, except for Shelbux, the "delta ratio" decreases as Δ increases. The lunar craters having $\Delta > 15$ km show the same tendency (Ebert's Rule: see Fig. 2*b*, which is based on data listed by the writer (**4**)). Shelbux shows the reverse trend.

It was found, from repeat experiments, that diameters or depths were never in error by $\pm 0{\cdot}64$ cm. The total errors in the delta ratio could therefore possibly be up to the order of 20–30 per cent in the vicinity of $\mathscr{F}_c$ in each case, but the assumption that the slopes are of different signs is considered to be reasonable in view of the fact that the curve of Fig. 2*a* represent averaged values of the variables. The results which follow depend on the validity of this assumption.

Now the $\delta/\Delta - \Delta$ curve for the lunar craters is incomplete at $\Delta < 15$ km. Estimates of the delta ratio for lunar craters of $\Delta = 15$ km have been made by Hopmann and Behrmann (see the point marked on Fig. 2*b*) and by Fielder, Moore, and Warner (**5**), who found the ratio to be at least 0·13 (actually for craters in the 10 to 20 km diameter grouping). Arthur (**6**) has suggested to the writer that the delta ratio may not continue to increase with decreasing Δ.

Close to $\mathscr{F}_c$, values of the delta ratio as large as 0·3 would probably have to be attributed to lunar craters as small as a metre of so in diameter if they were formed in cohering dust or in solid rock and, in this case, Ebert's Rule might be expected to hold for all values of Δ. If, however, the lunar rocks have a gravelly texture, one would expect to find a maximum value of the delta ratio in the region $15\text{ km} > \Delta > 0$. It is therefore of importance to examine carefully the delta ratio of lunar craters in this diameter grouping.

The predicted behaviour of the delta ratio in different media is summarized in Table III. The possibility of the Moon's consisting of a medium of gravel

TABLE III

Medium	Variation of δ/Δ as Δ decreases
Cohering dust or solid rock	Monotonic increase
Cohering dust over solid rock	Non-monotonic increase
Material behaving like a gravel	Monotonic decrease
Material behaving like a gravel over solid rock	Increase and then decrease

down to the depths of the deepest craters (say ~ 10 km) can be eliminated, since the condition that the delta ratio decreases as Δ decreases does not satisfy Ebert's Rule. Furthermore, if there is a layer of gravel—or other rock with similar properties—covering more compact lunar rock, then a turning point should be expected in the $\delta/\Delta - \Delta$ curve at $\Delta < 15$ km. As Ebert's Rule is observed to hold down to craters as small as $\Delta = 15$ km, the present theory predicts that there cannot be a layer of gravel covering the Moon to a depth (obtained from Fig. 2*b*) of greater than 2 or 3 km.

4. *The shapes of the craters.*—The craters corresponding to curves 1 in Figs. 1 and 2 took the general cup-form shown in Fig. 3*a*, whereas the craters formed in Shelbux were essentially conical pits (with the inner slopes slightly convex in all except for near-surface explosions: Fig. 3*b*). Cross (**7**) showed that the majority of the small ($5 \lesssim \Delta \lesssim 25$ km) craters on the Moon were probably paraboloids. Of 86 craters which Cross examined in this diameter-grouping, only 11 per cent did not fit the simple conoidal form. Hence it seems as if one may further restrict the maximum depth of any gravel-layer* (bearing in mind that the limitation is statistical and does not necessarily apply to any given part of the Moon) to only 1 or 2 km (using $\delta/\Delta = 0{\cdot}3$ and $\Delta = 5$ km).

* For gravel, read also possibly, " free dust ". If it can be shown that other materials, in addition to gravels, yield conical explosion craters, the results given here would be modified. It is possible, for example, that powders would behave like gravel when completely dry.

As shown by Cross, the shape of a shadow-boundary varies, with the altitude of the Sun, in a way which is strikingly different in the cases of conoidal and conical craters when a shadow covers little more than half a diameter of a crater (Figs. 4*a* and 4*b*). Fig. 4*c* shows the shadow effects in conical craters with convex slopes. Cross pointed out that a change in the delta ratio does not change the sequence of shadow-forms which appear in a crater, but merely means that the elevation of the Sun, for which a partciular shadow-form appears, is different. It is unfortunate that observers usually look at small craters when they are near to the terminator: it is at higher altitudes of the Sun that the differences between conoidal and conical craters are most marked.

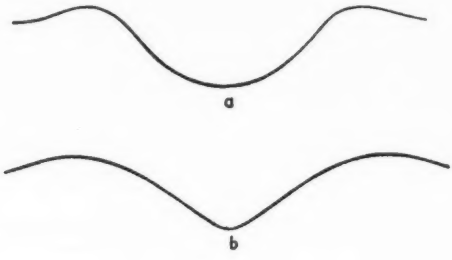

FIG. 3.

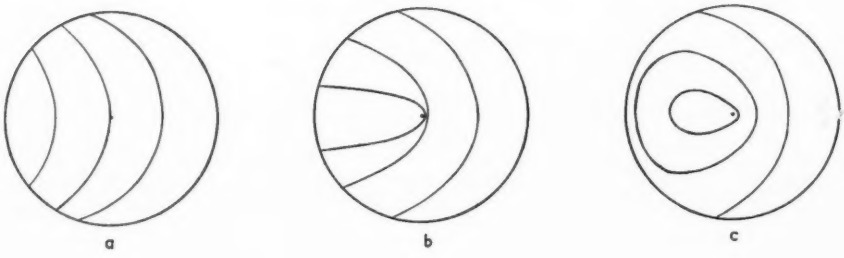

FIG. 4.

Cross found only one doubtful conical crater (Messier) in 84. Kuiper (**8**) maintains that one class (which he supposes to have been produced explosively, but by internal action rather than by meteorites) of lunar crater, having $\Delta \lessapprox 3$ km, has members shaped like inverted cones, but that the members of this class with $\Delta > 3$km have convex slopes.

For the reasons stated (cf. Fig. 4) conoidal and conical craters as small as this would be indistinguishable at low solar altitudes. One must therefore presume that Kuiper's observations were made under high angles of illumination. In this case, contrast and diffraction distort the true scene; if the craters have dark floors partly enclosed by bright walls, there is a tendency for the shadows and the dark floors to unite and become indistinguishable; and accurate observations of such small shadows become difficult. It would clearly be of great interest to have more observations of small craters with large instruments under good conditions.

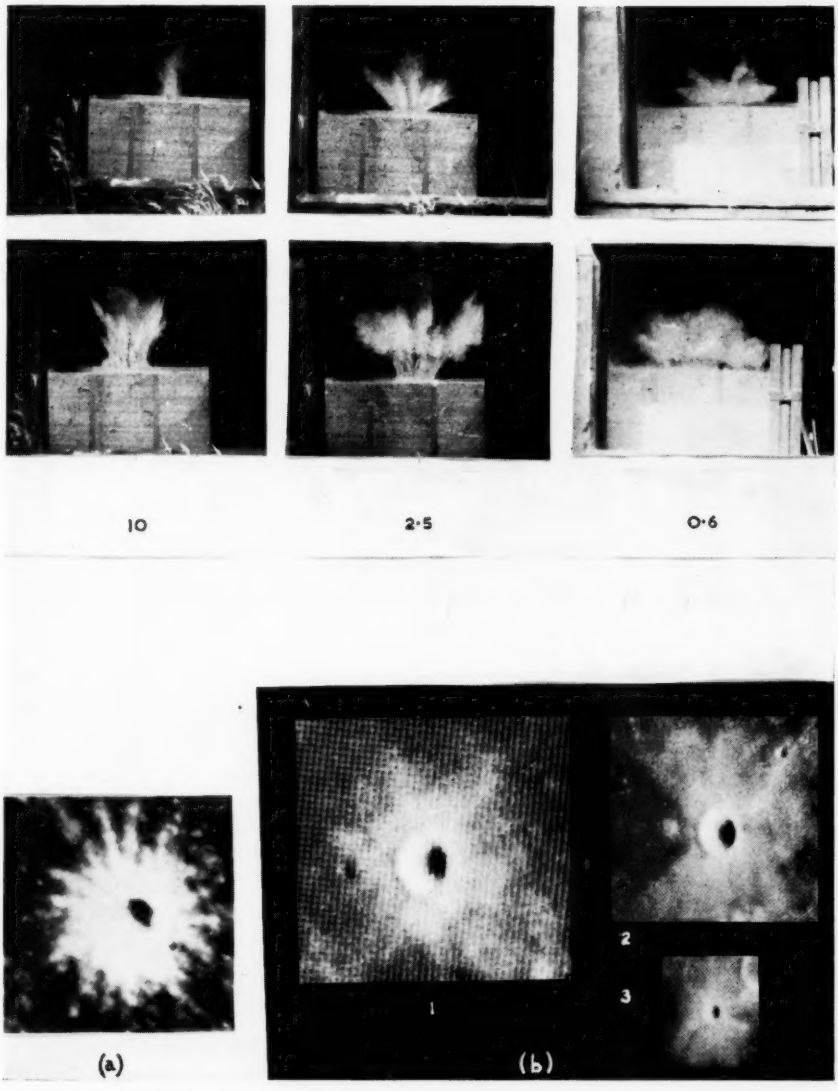

FIG. 5 (*top*).—*Explosions in powder at various focal depths* (*cm*).

FIG. 6 (*bottom*).—(*a*): *rays around a bomb crater*, $\Delta \simeq 15$ *m*.

(*b*): *Rays around three lunar craters*, $\Delta_1 = 8$ *km*, $\Delta_2 = 11$ *km*, $\Delta_3 = 5$ *km*. (*Mount Wilson Observatories.*)

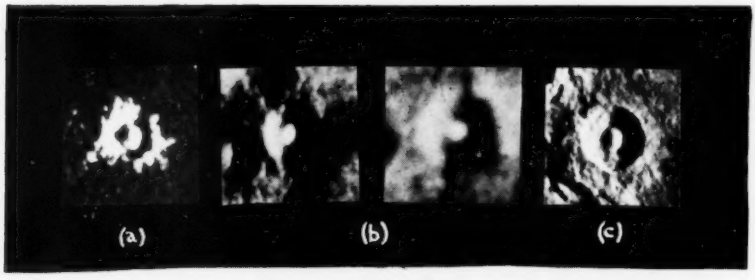

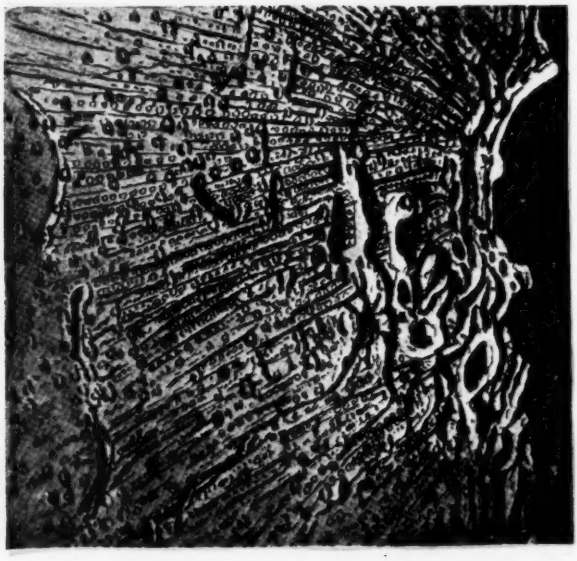

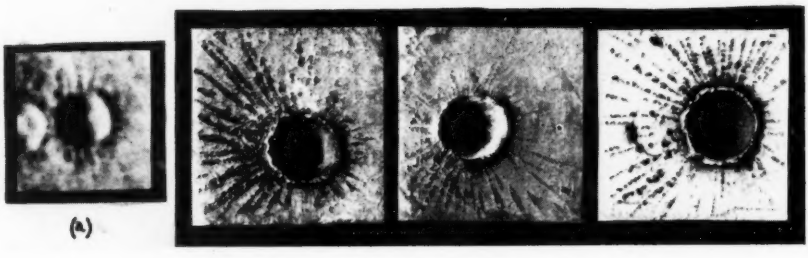

FIG. 9. (*Top*)—(*a*) *Bomb crater with central hill, First World War* (*Astrophysical Journal*).
(*b*) *Two bomb craters with central hills, Second World War.* $\Delta_1 \approx 15$ *m*, $\Delta_2 \approx 20$ *m.*
(*c*) *The lunar crater Alpetragius,* $\Delta = 41$ *km, with central mountain* (*Mount Wilson Observatories*).

FIG. 11. (*Centre*)—*Western flanks of Copernicus,* $\Delta = 91$ *km, drawn by H. P. Wilkins.*

FIG. 12. (*Bottom*)—(*a*) *Bomb crater,* $\Delta \approx 15$ *m, with radial structure;* (*b*) *Small explosion craters* ($\Delta \sim 1$ *cm*) *in lead.*

XUM

Accepting Kuiper's observations, the present experiments lead one to predict that there is a material having the properties of a gravel covering those parts of the Moon where these conical, 3 km-diameter craters appear, up to a depth of at least 0·3 km (using $\delta/\Delta = 0{\cdot}1$; cf. Fig. 2*a*). Even if the specific origin of these conical craters is not defined, this result probably still holds.

5. *Relationship between the angles of ejection of material and the focal depth: the origin and nature of rays.*—As described in Section 1, a special series of explosion experiments was conducted with charges B. The photographic frames (Fig. 5) depicting the initial stages of each explosive upheaval were measured to provide data on the dependence of focal depth on the initial directions of motion of the ejected particles. Fig. 5 shows the first and third frames of a film strip, for each of the focal depths indicated. (Adjacent frames were separated in time by about 1/300 sec.)

It is evident that, with an explosion at a small focal depth, the ejecta can be grouped into a low-angle and a high-angle zone. The same effect may be seen in a photograph of an explosion, on a much larger scale, reproduced in a paper by Giamboni (**9**). Experiments showed that the low-angle branch was the one responsible for the long, thin rays which are characteristic of impact craters (both explosive and non-explosive), bomb-craters formed in limestone country (Fig. 6*a*), and certain lunar craters (Fig. 6*b*). The high-angle branch is normally widely and uniformly dispersed and contributes merely to the general background intensity around a crater. Measurements of the bounding angles of elevation, θ, of the low-angle branch are listed for different focal depths in Table IV and these results are represented graphically in Fig. 7. In this series of experiments, the critical focal depth was found to be 6·4 cm. Hence,

TABLE IV

Focal depth (cm)	0·6	1·3	2·5	5*	7·6*	10	12·7	20	25	30
Range of θ (deg)	16–19	29–40	26–50	34–43	41–49	52–59	66–85	77–87	80–83	58–90

* The critical focal depth lies between these two values.

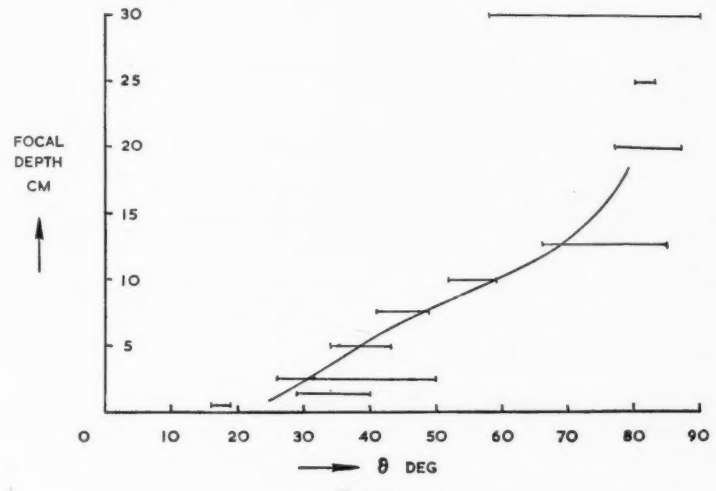

FIG. 7.

using the result of Section 3, namely, that $\mathscr{F} \gtrsim \mathscr{F}_c$ probably holds in the formation of lunar meteroritic craters, it seems as if the rays on the Moon provide strong evidence of near-surface explosions caused by meterorites.

A plausible hypothesis for the origin and physical nature of the lunar rays, based on these observations, is that they were produced by particles ejected from craters at comparatively low angles of elevation and that, since the rays take the form of short, bright streaks, often originating in very small craters, they are composed of these crater-pits and numerous small particles excavated from just beneath the surface of the Moon and thrown across the surface from each pit to form an array of debris often in the shape of an isosceles triangle of small vertical angle. The pit, which occurs at this vertex, and the ray-particles, would be bright, relative to the background, simply because they represent disturbed sub-surface materials; the surface itself having been darkened by, for example, the action of ultraviolet light, as described by Stair and Johnston (**10**). Such a physical structure would be consistent with the variation of luminous intensity, with the phase, which is characteristic of the rays.

6. *Deep focus phenomena*: *domes.*—In spite of the fact there there are good reasons for supposing that high-energy meterorites colliding with the Moon would explode at small $\mathscr{F}$-values, it is nevertheless of interest to examine the surface-effects of deep-focus explosions. Domes are a common feature of the Moon's surface, and domical uplifts may be produced, under certain conditions, by deep-seated explosions.

Table V generalizes the results obtained, the various phenomena occurring at increasing values of $\mathscr{F}$, as indicated. The slurry experiments were instructive

TABLE V

$\mathscr{F}$	Powders**	Shelbux	Slurry
$\leqslant \mathscr{F}_c$	Cup-shaped crater (Fig. 3*a*)	Conical crater (Fig. 3*b*)	Cup-shaped crater (Fig. 8*a*)
$> \mathscr{F}_c$	Partial camouflet formation, followed by tendency of surface materials to slump, forming a cylindrical hole, or a cup-shaped crater.	Conical crater	Camouflet, capped by one large dome (Fig. 8*b*)
$\geqslant \mathscr{F}_c$	Camouflet (Fig. 8*c*) and many domes* and pits† clustering around the epicentre	No regular effect	Camouflet and many small domes* and craters due to material falling back.

**Note that if these powders had been dehydrated, the craters formed might have approached the conical shape.

*Dome-top craters (Fig. 8*c*) were sometimes produced, and were due to the collapse of material from the top of a dome when the gases, which produced the domes themselves, streamed out. The walls of these dome-top craters were without external slopes. See, also, Baldwin (**1**).

†These pits were due to (*a*) material, detached from the surface during a stress-pulse falling back again; and (*b*) the ascent of gases freeing themselves from the high-pressure gas chamber (Fig. 8*c*). The frequency of occurrence of these craters, per unit of surface, decreased with increasing epicentral distance.

because the slurry behaved in such a way that, as soon as the stresses acting on it were reduced to certain values, its motion virtually ceased, and the "frozen" forms could then be examined at leisure. The results indicated that they were practically equivalent to those which would have been found had it been possible

to take high-speed, close-up photographs of the initial phases of the explosive processes in the cases of the other media.

Terrestrial domes are common igneous phenomena, and they are due to sill-type intrusions, or to batholiths. The domes on the Moon might of course be of similar origin and those with dome-top-craters (which are also not uncommon

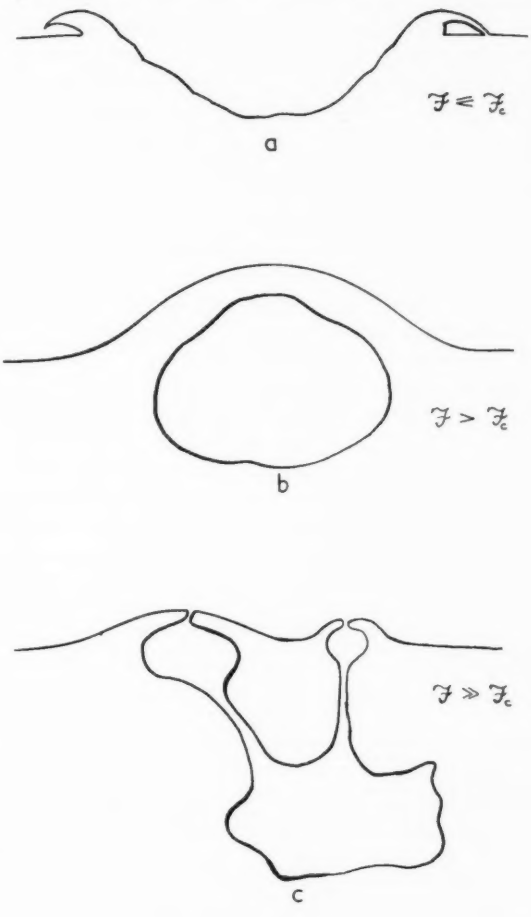

FIG. 8

on the Moon) might be extrusive. It is only because of the possibility that, under certain conditions, a meteorite might explode at depth (rather than on the Moon's surface) that the deep-focus phenomena observed in the experiments have been noted here. There is no particular reason to suppose that a high-energy meterorite would give rise to dome-type phenomena, and no domes would be observed, it appears, in a medium of gravel. In particular, one would not expect to find domes next to conical craters if the domes were due to deep focus explosions. If such an association is observed, it will mean that the lunar domes

are probably igneous phenomena, for a gravelly medium could be arched by an igneous intrusion.

7. *Craters with central eminences: high- and low-velocity collisions.*—No central elevations were formed, in any of the experiments, by the direct action of the explosives. (In the Limbux-powder and slurry experiments, deep-focus explosions sometimes produced small craters with central hills. These craters were due to the outrush of gases and the central hills themselves were produced by the action of the ascending gases on the material slumping into—and thus tending to block—the narrow feed-pipe. Kuiper (**11**) has envisaged a rather similar process for the formation of the central mountains of lunar craters.) However, Partridge and Vanfleet (**15**) showed that 2 km sec^{-1} projectiles containing cavities in their leading surfaces generally produced craters with central peaks. Furthermore, some bomb-craters of both World Wars show distinct central hills (Figs. 9*a* and 9*b*), and it is interesting to compare these with the lunar craters with central mountains and, especially, with the lunar crater Alpetragius (Fig. 9*c*). The precise conditions under which the bomb-craters were formed are not known to the writer, but the comparison—even though the diameters of the terrestrial and lunar craters are in the ratio of $1:10^3$—indicates at least that there is no reason to suppose that, given certain specific conditions, high-velocity impact craters would not have central elevations. A mechanism for the formation of central mountains by impacts of meterorites has been proposed by Gold (**2**).

Small-scale experiments in which "charges" of dry powder are dropped on to a layer of similar powder produce craters with central protuberances only if the substrata (see Fig. 10) are relatively hard and close to the surface. Low-velocity meteoritic impacts in which crushing, rather than explosive violence, is the principal mechanism by which a crater is shaped, may yield similar results. In practice, the hard sub-stratum might be either pre-existent or induced by compression. At such low velocities, a soft sub-stratum, such as dust, would favour the production of a cup-shaped crater having a volume proportional to the momentum of the missile, as shown by Johnson (**12**).

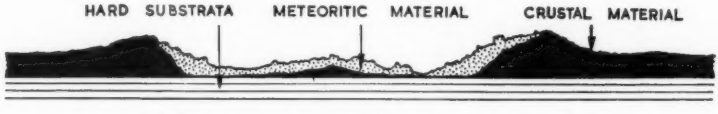

FIG. 10.—*Cross-section of non-explosive crater in powder.* $\Delta = 13$ *cm.*

Now those lunar craters with the most conspicuous ray-systems display prominent central mountains. In the low-velocity "crushing" experiments just described, the lengths of rays were found to increase both with increase of impact velocity and with increasing tendency to form a central mound. The bulk of these central mounds consisted of compressed, but otherwise undisturbed, ground material (see Fig. 10) and were of the same order of size as the falling "charge". The rays took the forms of streaks which often emanated from small "secondary" craters, as in the case of the lunar rays. Confirming the work of the writer, Sabaneev (**13**) concluded, from similar experiments with dry powders, that the directions and lengths of rays depended upon the forms of the ringwalls of craters. This is another indication that the ray-forming particles

were shot off at small angles to the horizontal and that the upheavals occurred at small focal depths.

Secondary impact craters—"bombs", ejected from larger craters during their formation—must exist on the Moon and, having only low velocities (probably $\sim 0{\cdot}5$ to $1{\cdot}5\,\mathrm{km\,sec^{-1}}$ and never $> 2{\cdot}4\,\mathrm{km\,sec^{-1}}$), crushing would play an important role in their formation. It is therefore proposed that certain other of the lunar craters were produced not simply by crushing, as in the case of these low-velocity impacts; and not simply by explosions resulting from very high-velocity collisions; but by a combination of these two processes.

8. *Radial patterns around explosion craters.*—Some prominent radial furrows were observed immediately outside the slurry craters, but only in those explosion experiments conducted at small values of the parameter $\mathscr{F}$. These markings provided clear evidence that several lumps of material had been ejected at glancing angles to the horizontal. Secondly, Scully (**14**) observed surface cracks radial to a small-scale, high-velocity impact crater. These two phenomena are distinctly different, and possibly both are found on the Moon.

Lunar craters very frequently display approximately radial features which may be classed, broadly, as valleys, ridges, or crater-chains. The so-called valleys around Mare Imbrium have been discussed at length in the literature, and some of these are crateriform in structure. The latter may be of internal origin or they may even have been formed by the ricocheting of objects approaching the surface at glancing angles (cf. Fig. 2 in the paper of Partridge and Vanfleet (**15**)).

Fig. 11 shows a detailed drawing of the western flanks of Copernicus made by the late H. P. Wilkins (**16**) with the Meudon 84 cm (33-inch) refractor under favourable conditions at time of sunrise. Wilkins' short paper is of such interest that extracts relevant to the present discussion are translated, here:—

> "Certain objects. . . . . appeared to be covered by a mass of details, small hills, tiny craters and smaller holes, whilst the entire surface appeared to be criss-crossed by lines as fine as hairs."
>
> "Hundreds of holes of some tens* of metres in diameter were seen—like wells, sunk vertically, without any walls on the surface, but evidently of great depth, judging by the shadows cast even under a very high light. They appeared like black spots, sometimes isolated, but sometimes in lines, often connected by a line, like knots in a rope. Sometimes the line ended in a hillock and reappeared on the other side as if it had run through a tunnel."
>
> "Between the western wall of Copernicus, as far as the eye could see, and the lightly marked surface of Stadius, all the space appeared to be covered by 'spines' almost parallel to each other, strongly marked near to Copernicus, more lightly marked towards Stadius, and barely perceptible near to Stadius. They ran in straight lines until Stadius was approached. Between these spines lines of craters appeared, and in some cases the above-mentioned holes, as the level of the ground changed."

Thus, according to Wilkins, the chains of small craters are set in between the radial ridges. Certainly, bomb-craters sometimes display radial ridges (Fig. 12*a*); and crater-chains showing a rather surprising degree of radialism may be found around some explosion craters. Those in Fig. 12*b* were produced when metal-cased detonators were placed vertically on, and fired with their base-charges in contact with, thin rectangular prisms of lead. Once again, one is led

* This should read "hundreds".

to suggest that the disturbances which produced the lunar craters were essentially shallow-focus phenomena.

It would undoubtedly be dangerous to draw strict analogies between all the similar characteristics of the small-scale experimental and bomb-craters, and those of the lunar craters; but the degree of similarity between certain of the features on the two scales is so striking that it is hoped that these experiments may be regarded as a starting point for further research.

Acknowledgments.—The writer's experiments were performed during the tenure of a State supplemented J. R. Ashworth Research Scholarship at the University of Manchester. Professor J. A. L. Matheson and Dr P. W. Rowe, of the Department of Mechanical Engineering of Manchester University, provided space and equipment for the experiments in which the non-explosive craters were made. Through Professor Z. Kopal, Professor of Astronomy at Manchester University, facilities for the performance of the explosives' experiments were very kindly provided by the Directors of the Safety in Mines Research Establishment, at their Buxton Laboratories. I.C.I. detonators, gelignite, and Kieselguhr were provided gratis by S.M.R.E., and up to 8 cwt. of each of the materials Limbux, Baribux, and Shelbux were provided gratis by I.C.I. Ltd., Buxton. Assistance with photography was given by Mr F. Holden and Mr H. Martin. Dr J. G. Dawes, Mr Godwin, Dr H. C. Grimshaw, Dr E. M. Guenault, Dr Rae, and Mr R. Wilson, all of S.M.R.E., gave valuable advice on the handling of explosives.

Dr W. Taylor, and several of his staff at the Stevenston Research Laboratories of the Nobel Division of I.C.I. Ltd., also gave useful advice and demonstrated the formation of small explosives' craters in lead blocks and in sand.

Mr W. Beanland provided a translation of Dr Wilkins' paper from the Spanish. Mr H. Martin and Mr Th. Saemundsson prepared the photographic illustrations.

University of London Observatory,
Mill Hill Park, London, N.W.7:
1961 *March.*

References

(1) Baldwin, R. B., *The Face of the Moon*, pp. 140; 142, Univ. Chicago Press, 1949.
(2) Gold, T., *M.N.*, **115**, 585–604, 1955.
(3) Gilvarry, J. J., and Hill, J. E., *P.A.S.P.*, **68**, 223–229, 1956; *Ap. J.*, **124**, 610–622, 1956.
(4) Fielder, G., *Structure of the Moon's Surface*, p. 18, Pergamon Press, 1961.
(5) Fielder, G., Moore, P., and Warner, B., *J.I.L.S.*, **1**, 151–154, 1960.
(6) Arthur, D. W. G., private correspondence.
(7) Cross, C. A., *J.B.A.A.*, **64**, 167–171, 1954; and **65**, 72–81, 1955.
(8) Kuiper, G. P., *J. Geophys. Res.*, **64**, 1713–1719, 1959.
(9) Giamboni, L. A., *Ap. J.*, **130**, 324–335, 1959.
(10) Stair, R., and Johnston, R., *J. Res. Nat. Bur. Stand.*, **51**, 81, 1953.
(11) Kuiper, G. P., *Proc. Nat. Acad. Sci.*, **40**, 1096–1112, 1954.
(12) Johnson, F. N., *J.B.A.A.*, **66**, 319–322, 1956.
(13) Sabaneev, P. F., *Bull. Vsesoyuznovo Astr.-Geod. Obs.*, No. 17 (24), 22–25, 1956.
(14) Scully, C. N., *Proc. of Lunar and Plan. Explor. Colloq.*, **1**, 23–25 (Fig. 2). North American Aviation, 1959.
(15) Partridge, W. S., and Vanfleet, H. B., *Ap. J.*, **128**, 416–419, 1958.
(16) Wilkins, H. P., *Urania*, No. 230, 1952.

XUM

UBV PHOTOMETRY OF THE ASSOCIATION CASSIOPEIA V

*V. C. Reddish**

(Received 1961 April 5)

Summary

Magnitudes of 127 OB stars have been determined photographically in the *UBV* system. A catalogue and identification chart is given. The two-colour diagram shows a reddening which increases with intrinsic colour index.

The association Cassiopeia *V* ($23^h\,50^m$ (1900) $+61°$) appears in the Hamburg spectral survey (Hardorp *et al.*, 1959) as a rich concentration of OB⁻ stars. Using the Hamburg 80/120 cm Schmidt telescope, *UBV* magnitudes have been measured photographically for the OB stars in an area about 2° in diameter centred on the association. The Eastman Kodak plate and 2 mm Schott filter combinations were 103aO + UG2, 103aO + GG13 and 103aD + GG11 for *U*, *B* and *V* respectively. Identification charts are given in Plate 3 and Fig. 1. The magnitudes were calibrated, and colour equations determined, by the photoelectric sequence in NGC 7790 (Sandage 1958), which is on the edge of the association. Four plates in each colour were measured on the Haffner iris photometer, the iris reading of which is punched directly on to cards. The reductions were carried out on an IBM 650 computer using a standard programme devised by Mr Brosterhus. The results are given in Table I. Stars brighter than $V = 10{\cdot}5$ are not included because the standard sequence did not extend to stars brighter than $V = 11{\cdot}0$. The average internal mean errors are $\pm 0^m{\cdot}023$ in V, $\pm 0^m{\cdot}042$ in $B-V$ and $\pm 0{\cdot}036$ in $U-B$.

The apparent colour magnitude array, Fig. 2, is cut off at the top by the omission of stars brighter than $V = 10{\cdot}5$ and at the bottom by the limiting magnitude of the Hamburg spectral survey. It shows a wide dispersion in apparent colour.

The two colour diagram, Fig. 3, displays an unusual feature. The points are distributed about a mean line which is neither that of a main sequence with constant reddening nor a group of stars of similar intrinsic colours and variable reddening. The line is such that the reddening increases with the intrinsic colour of the star according to the equation

$$E_{(B-V)} = 0{\cdot}77(B-V) + 0{\cdot}33 \qquad (1)$$

where $(B-V)$ is the observed colour index. The average $B-V$ component of the mean deviation about this line is $\pm 0^m{\cdot}050$ which is satisfactory when compared to the average internal mean error of $\pm 0^m{\cdot}042$.

* This work was carried out while the author was a guest investigator at the Hamburg Observatory.

TABLE I

NGC 7790

Sandage No.	*V*	*B–V*	*U–B*
A	11·11	0·23	−0·52
B	12·12	0·46	−0·05
C	12·48	0·56	+0·14
E	12·77	0·43	−0·13
F	12·82	2·05	
G	13·08	0·57	+0·28
H	13·20	0·47	+0·29
I	13·09	1·27	+0·86
J	13·26	0·48	+0·33
K	13·25	1·45	
L	13·30	0·62	+0·15
M	13·34	0·38	−0·17
N	13·53	0·42	−0·05
O	13·52	0·35	−0·08
P	13·59	0·78	+0·17
Q	13·77	0·36	+0·02
R	14·17	0·40	−0·06
S	14·26	0·52	−0·24
T	14·20	0·70	
U	14·51	0·58	+0·27
V	14·52	0·50	+0·07
W	14·58	1·36	
X	14·58	0·45	0·00
Y	14·72	1·25	

Cassiopeia V

Hamburg No.	*V*	*B–V*	*U–B*
60°24	12·39	0·63	−0·25
25	11·01	0·54	−0·28
29	12·60	0·63	−0·23
33	10·92	0·60	−0·27
34	10·92	0·61	−0·17
35	12·37	0·76	+0·01
36	10·77	0·50	−0·27
38	11·99	0·55	−0·26
40	11·18	0·65	−0·05
41	10·83	0·69	−0·07
43	12·34	0·73	−0·09
44	11·40	0·57	−0·13
45	11·77	0·68	−0·15
48	11·72	0·52	−0·29
49	11·51	0·44	−0·35
52	11·61	0·75	−0·08
55	10·68	0·39	−0·24
58	11·51	0·54	−0·27
59	10·80	0·32	−0·59
60	11·29	0·43	−0·27
61°21	11·63	0·62	−0·11
22	11·24	0·54	−0·18
23	11·31	0·62	−0·24

Hamburg No.	*V*	*B–V*	*U–B*
25	11·52	0·54	−0·31
27	11·16	0·82	−0·07
28	10·93	0·41	−0·57
30	11·32	0·45	+0·38
31	11·93	0·34	−0·29
32	11·66	0·57	−0·17
33	11·31	0·33	−0·43
34	10·50	0·35	−0·61
37	10·83	0·39	−0·34
38	11·19	0·38	−0·51
39	11·08	0·45	−0·25
40	11·86	0·47	−0·42
41	12·16	0·61	−0·07
42	10·77	0·33	−0·60
43	12·14	0·37	−0·34
45	11·85	0·32	−0·45
46	11·68	0·43	−0·43
47	11·42	0·69	+0·16
48	10·68	0·38	−0·44
50	10·84	0·57	−0·32
51	11·31	0·42	−0·36
52	11·91	0·49	−0·32
53	11·51	0·53	−0·02
55	11·87	0·35	−0·42
56	12·32	0·63	−0·11
57	11·19	0·55	−0·22
58	12·07	0·34	−0·37
60	11·89	0·39	−0·13
61	12·09	0·74	−0·21
62	11·95	0·47	−0·34
63	10·95	0·43	−0·35
66	11·66	0·41	−0·40
67	12·31	0·50	−0·36
69	12·04	0·31	−0·48
71	11·71	0·56	−0·16
72	11·96	0·34	−0·48
74	12·53	0·56	−0·21
75	12·08	0·42	−0·32
76	12·37	0·44	−0·44
77	11·36	0·26	−0·58
80	11·65	0·31	−0·47
81	10·97	0·48	−0·15
82	11·05	0·51	−0·29
84	10·68	0·37	−0·42
85	10·87	0·43	−0·41
86	12·53	0·59	−0·27
87	12·14	0·61	−0·19
90	11·33	0·54	−0·22
91	12·09	0·58	−0·28
92	11·17	0·50	−0·22
94	11·53	0·59	−0·18
95	12·27	0·55	−0·30

Hamburg No.	*V*	*B–V*	*U–B*
97	11·94	0·54	−0·29
98	11·15	0·59	−0·27
99	10·78	0·24	−0·54
100	11·90	0·52	−0·36
101	10·57	0·33	−0·46
103	11·92	0·36	−0·49
104	11·76	0·39	−0·48
105	12·84	0·42	−0·38
106	10·92	0·29	−0·50
107	10·75	0·34	−0·53
108	11·16	0·32	−0·51
109	12·04	0·37	−0·47
110	10·66	0·36	−0·38
111	11·21	0·45	−0·18
112	10·52	0·22	−0·49
114	12·21	0·40	−0·36
115	12·50	0·34	−0·32
116	11·68	0·36	−0·29
118	11·43	0·53	+0·13
120	11·75	0·40	−0·36
62° 5	11·75	0·46	−0·12
6	12·09	0·56	−0·05
7	11·39	0·50	−0·20
8	11·86	0·55	−0·14
9	11·10	0·61	−0·10
10	11·15	0·54	+0·03
11	11·35	0·77	0·00
12	10·94	0·44	−0·46
13	12·32	0·63	−0·03
15	11·59	0·48	−0·20
17	11·96	0·46	−0·32
19	10·69	0·69	−0·06
20	12·46	0·61	−0·10
22	11·35	0·74	−0·06
25	11·52	0·77	+0·03
26	12·41	0·59	−0·21
28	10·86	0·55	−0·01
30	11·54	0·46	−0·19
31	12·48	0·68	−0·08
32	10·76	0·45	−0·21
33	11·89	0·47	−0·34
34	11·14	0·30	−0·60
36	11·98	0·48	−0·29
37	11·64	0·47	−0·38
38	11·47	0·89	+0·51
40	11·12	0·36	−0·27
41	11·96	0·46	−0·37
42	11·16	0·40	−0·26
43	12·32	0·38	−0·38
44	12·54	0·48	−0·29
45	12·22	0·56	−0·20
51	11·58	0·35	−0·37

XUM

V	U-B
	−0·29
	−0·27
	−0·54
	−0·36
	−0·46
	−0·49
	−0·48
	−0·38
	−0·50
	−0·53
	−0·51
	−0·47
	−0·38
	−0·18
	−0·49
	−0·36
	−0·32
	−0·29
	+0·13
	−0·36
	−0·12
	−0·05
	−0·20
	−0·14
	−0·10
	+0·03
	0·00
	−0·46
	−0·03
	−0·20
	−0·32
	−0·06
	−0·10
	−0·06
	+0·03
	−0·21
	−0·01
	−0·19
	−0·08
	−0·21
	−0·34
	−0·60
	−0·29
	−0·38
	+0·51
	−0·27
	−0·37
	−0·26
	−0·38
	−0·29
	−0·20
	−0·37

XUM

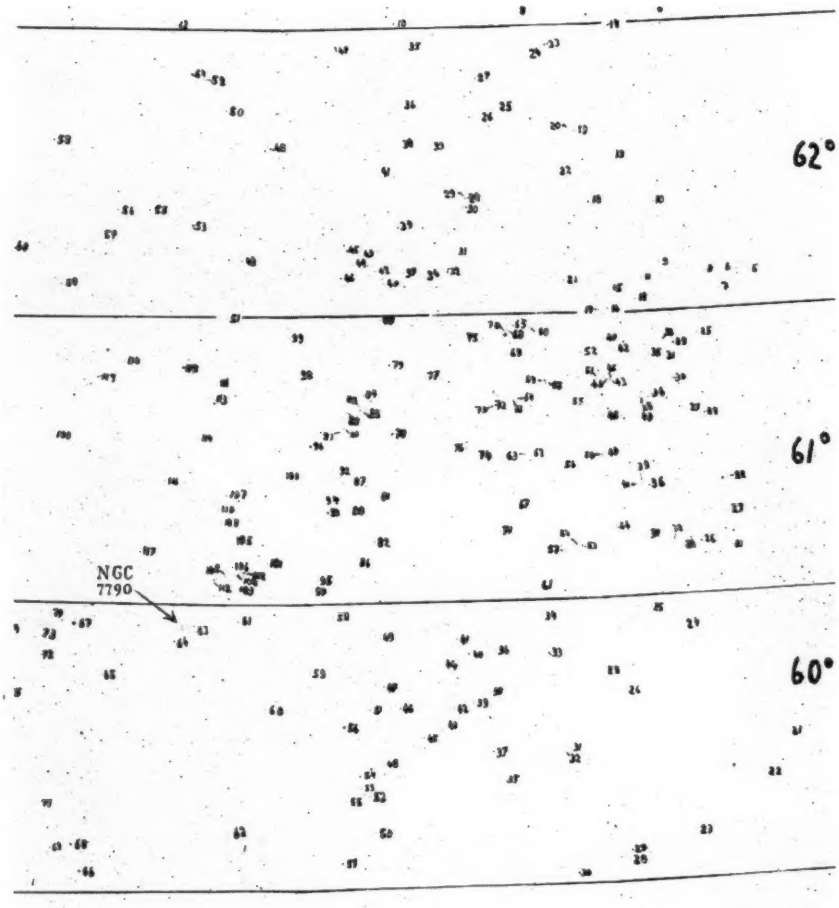

The star field of Cassiopeia V; see also the identification chart (*Fig.* 1).

Determining intrinsic colours $(B-V)_0=(B-V)-E_{(B-V)}$ using equation (1), and correcting the magnitudes for total absorption $A_V=3E_{(B-V)}$, the colour magnitude array corrected for reddening and total absorption now displays a narrow dispersion in colour (Fig. 4).

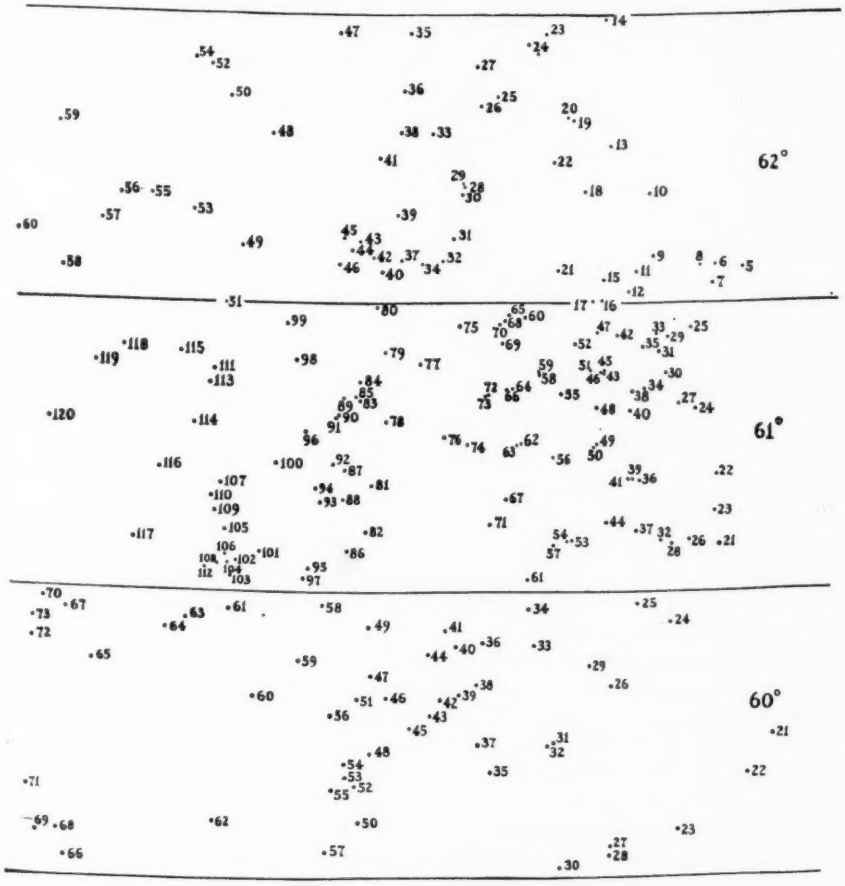

FIG. 1.—*Identification chart for the Cassiopeia V stars in Table* 1.

Comparison of the histogram of the numbers of OB⁻ stars of various $V-A_V$ magnitudes with a histogram of the distribution in luminosity classes from the data given by Slettebak and Stock (1957) indicates a true distance modulus of $12^m\cdot75$ with an estimated error of $\pm0^m\cdot35$ due to the fittings of the histograms to each other and to the absolute magnitude scale (assuming no errors in the absolute magnitudes used for the luminosity classes). The corresponding distance is $3\,500\pm600$ parsecs. This may be compared to the distance of $3\,630\pm250$ parsecs for the cluster NGC 7790 on the edge of the association, determined by

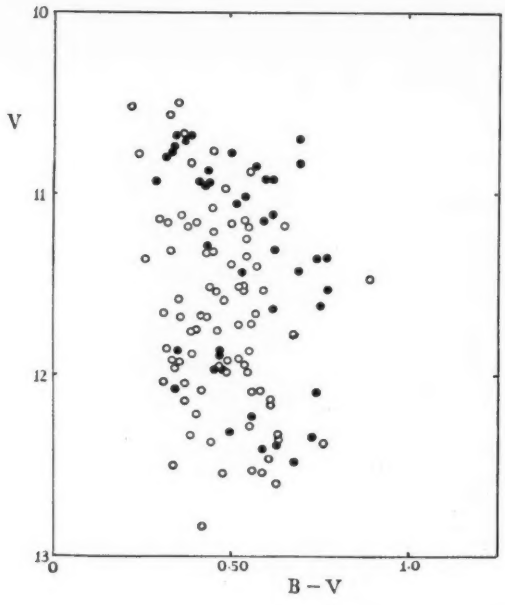

FIG. 2.—*Apparent colour-magnitude array; filled circles OB stars, open cirles OB⁻ stars.*

Sandage (1958). This method of obtaining the distance to the association, although crude, is completely independent of the method used by Sandage for NGC 7790, and the distances obtained are consistent with the view that cluster and association are connected.

The differences between the photoelectric measures by Sandage and the present photographic measures, for the standard stars used, are plotted in Fig. 5. If the peculiar slope of the points in Fig. 3 were the result of errors in one of the colour equations, the differences would depend on colour according to the slope of one of the lines given on Fig. 5 (*b*) and 5 (*c*), according as the true relation should be a reddening line or a reddened main sequence.

The conclusion that the dependence of colour excess on intrinsic colour is not the result of an error in the calibration curves is confirmed by the substantial dependence of colour excess on position (Fig. 6).

Variations in the reflectivity of the mirror cannot be the cause of such a large dependence. For example, even if the ultra-violet reflectivity varied discontinuously from zero to 100 per cent, while the visual reflectivity remained constant, the resulting errors could not be larger than $0^{m}{\cdot}25$ per degree of angular distance across the plate, about half the rate of variation of $U-V$ excess now found. In fact the reflective coating of the mirror was in good condition and any systematic errors due to variations in it cannot exceed a very few hundredths of a magnitude.

There is no significant dependence of the colour excesses, the dispersion of the colour excesses, or the internal errors of the measured colour indices, on distance from the standard stars (Fig. 7), nor is there any relation between the colour excess and the internal mean errors (Fig. 8). Variations in plate sensitivity

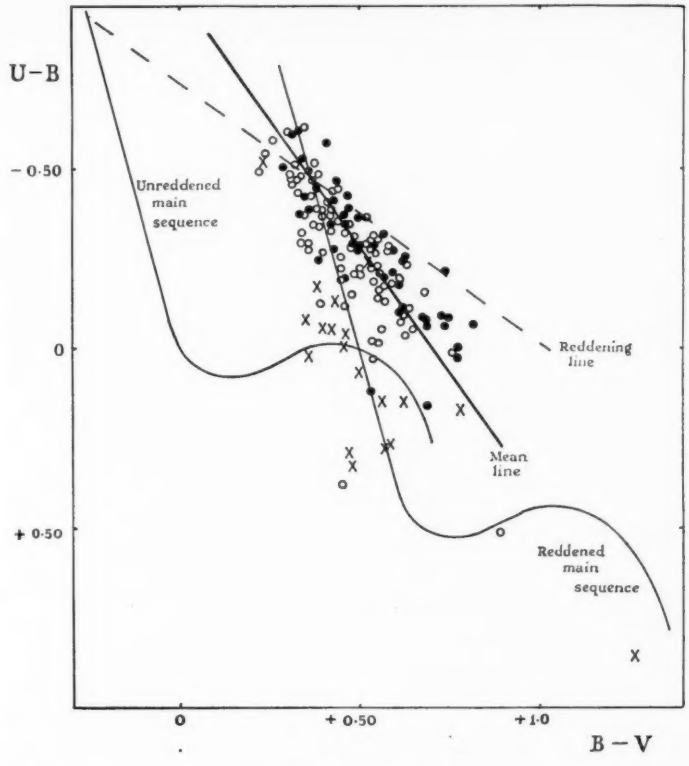

FIG. 3.—*Two colour plot. Filled circles OB stars; open circles, OB⁻ stars; crosses, stars in NGC 7790.*

as a cause of the variations in the colour excess across the association can therefore reasonably be ruled out because the sensitivity would not only have to be patchy but dependent on position in exactly the same way on at least all eight plates used for two of the three colours.

The patchiness of the colour excesses does not appear to be due to observational errors. That it is not the result of random groupings can be seen from Fig. 9. When the association is divided up into a number of equal areas, the solid line represents the average r.m.s. dispersion in colour excess in an area as a function of the angular diameter of the area. The dashed line is the corresponding curve to be expected from a random distribution of colour excesses with the same overall dispersion and sampling procedure. The consistently lower values of the observed curve indicate real groupings of similar colour excesses; and hence, through the dependence of colour excess on observed colour (Fig. 3) real groupings of stars with similar intrinsic colours.

It is concluded that the increase of the colour excess with the observed (and intrinsic) colour, and the grouping together of stars of similar colour, are real effects. However, the possibility of variable background nebulosity makes it important to test this conclusion by photoelectric measures.

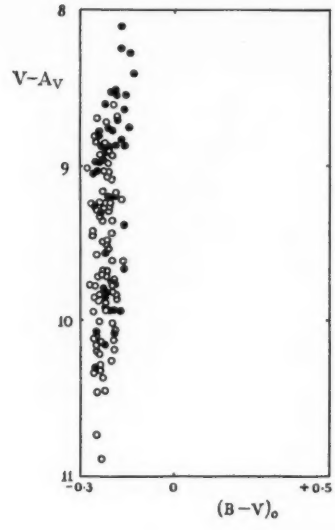

FIG. 4.—*Colour-magnitude array corrected for reddening and total absorption. Filled circles, OB stars; open circles, OB⁻ stars.*

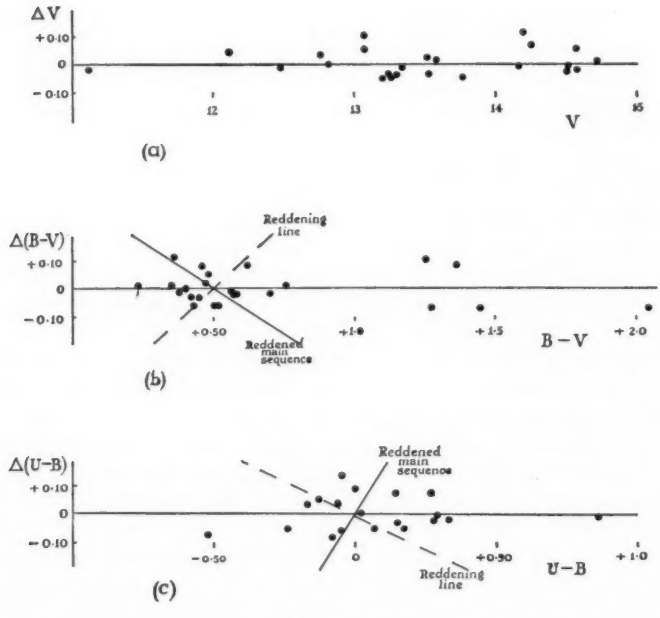

FIG. 5.—Δ *represents standard minus observed values for the standard stars in NGC 7790.*

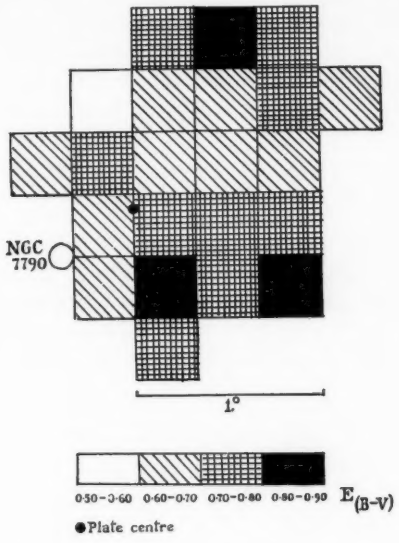

FIG. 6.—*Distribution of colour excess over the Association.*

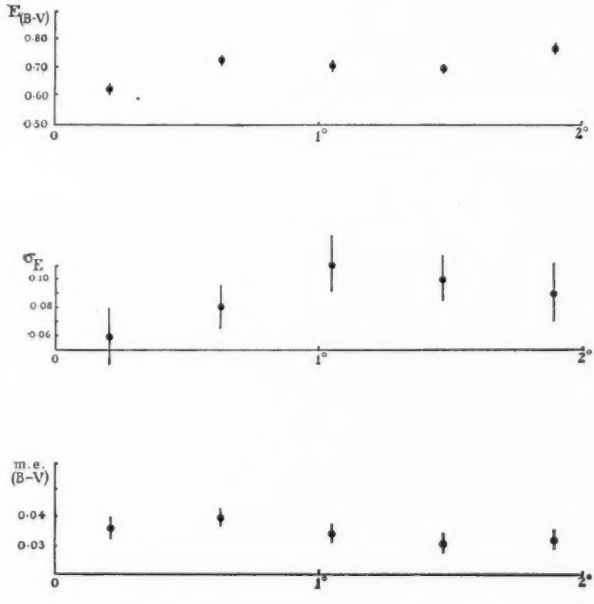

FIG. 7.—*Colour excess, dispersion in colour excess, and internal mean error, against angular distance from the standard stars.*

If the OB stars in Cassiopeia V were not in fact grouped together in space but were stars at greatly different distances seen through a hole in the absorption, it would be expected that the intrinsically bluer and hence normally intrinsically brighter stars would be observed to the greater distances and hence suffer the most reddening. But the contrary is observed. Also the considerable concentration of OB stars in a small area of the sky argues strongly in favour of the association being a real grouping in space. The distribution of the OB⁻ and OB stars in Fig. 4 is consistent with the belief that most of these stars are at about the same distance.

It is therefore possible that the redder stars are in the last stages of contraction to the main sequence, the groupings of them still being surrounded by absorbing matter in the clouds out of which they have condensed. It may be noted that if the bluer stars are on the main sequence they may be up to about two hundred times as old as the very slightly redder stars which have only just reached it.

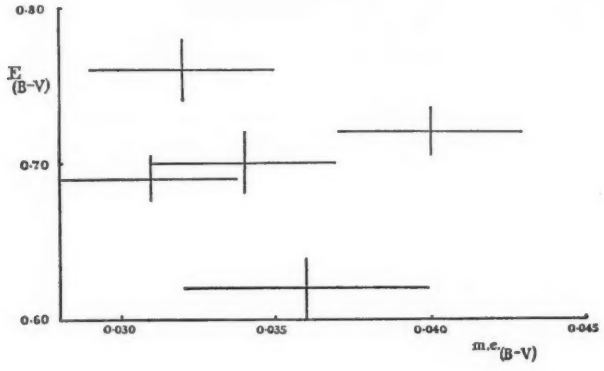

FIG. 8.—*Colour excess against internal mean error, from the data used in Fig. 7.*

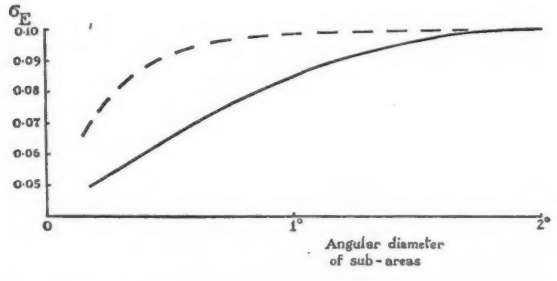

FIG. 9.—*Average r.m.s. dispersion in colour excesses in sub-areas as a function of the angular diameters of the sub-areas. Solid line, observed curve; dashed line, theoretical curve for a random distribution of colour excesses.*

Acknowledgments.—The author is indebted to Professor O. Heckman for the opportunity to use the excellent facilities of the Hamburg Observatory, to Mr Brosterhus for handling the computing, and to Mr Rohlfs for helping with the observing and in many other ways. The visit was made while the author was on leave of absence from the Nuffield Radio Astronomy Laboratories, Jodrell Bank, and was assisted by a grant from the Deutsche Akademische Austauschdienst-Bonn.

1961 *February* 20.

References

Hardorp, J., *et al.*, 1959, *Luminous Stars in the Northern Milky Way*, Hamburg Observatory.
Sandage, A., 1958, *Ap. J.*, **128**, 150.
Slettebak, A. and Stock, J., 1957, *Mitt. Hamburg*, No. 258, *Zs. f. Ap.*, **42**, pt. 2.

THE IDENTIFICATION OF METEOR SHOWERS WITH APPLICATION TO SOUTHERN HEMISPHERE RESULTS

C. Ellyett, C. S. L. Keay, K. W. Roth and R. G. T. Bennett

(Received 1961 April 28)

Summary

Further meteor shower results observed by radar at Christchurch, New Zealand, are now given, including results at high rates, and all Christchurch data are compared with visual observations, and radar results from Adelaide, for the declination range from $+26°{\cdot}5$ to about $-50°$. Seven meteor showers appear in all three surveys, and can be regarded as certain, and another 6 to 9, which are each reported twice, are probable. An additional 9 to 10 radiants, however, are found by each survey alone.

The errors inherent in the identification of meteor showers from radar data are considered. Different techniques have been used at Christchurch and at Adelaide. It is concluded that no single method of analysis is fundamentally better than any other.

The technique of shower identification depends partly on the nature of the background rate, which may be due either to sporadic meteors, or to the resultant of many minor radiants. The resolution of this uncertainty is necessary before the occurrence of less active showers can be confirmed.

The rate-count method has been extended to multiple range bands, resulting in a useful additional means of sorting out the significance of peaks in the rate curves.

---

1. *Introduction.*—Early radar equipments for the study of meteor showers were adjusted to be comparable in echo rate with visual observations. Consequently the visual shower picture was reinforced, and enlarged by the increased viewing hours available. Meteors not in shower groups were relatively infrequent and were regarded as sporadic.

At several centres, however, from about 1956 onwards, the radar detection rates were increased substantially above the visual rates. This resulted in difficulty in identifying all but the most prominent showers, due to their higher background count. The view was expressed by Ellyett and Keay in 1956 (**1**) that, with increasing sensitivity, major meteor showers blend with ever-increasing numbers of smaller meteor complexes, which may or may not be of annual occurrence. This idea, stressed again by the photographic results of Whipple and Hawkins (**2**), has now received substantial reinforcement from the work of Gallagher and Eshelman (**3**).

As opposed to this, however, a recent paper by Davies and Gill (**4**) describes the measurement of individual meteor orbits, and it is concluded that few of the meteors, down to a magnitude of $+7$ or a little smaller, belong to showers. This paper does mention, though, that three new showers were recorded in a total of

XUM

only 12 isolated days of observing. In addition the number of computed orbits per hour was not high, so the evidence against the idea of minor shower occurrence cannot yet be regarded as conclusive.

Weiss (**5**) has adopted a system of shower identification by determining the periods of high departure of rates from the monthly averaged background, followed by Clegg range–time plots (**6**) for these periods. A shower may not depart significantly from the mean, however, if either it continues for a number of days, or the background contains other minor showers.

The present paper considers the difficulties which occur in radar shower identification, either with range–time plots (**6**) or by partial rate analysis (**7**), and gives the empirical rules which have been evolved at Christchurch.

Three surveys of Southern Hemisphere radiant activity are now available, viz.:

(i) Earlier visual work (summarized in (**8**)), together with more recent surveys of visual, photographic and Northern Hemisphere radar results by Whipple and Hawkins (**2**) and by Fedynsky (**9**).

(ii) The Christchurch 1953 survey (**8**), together with previously unpublished 1954 and 1956 results.

(iii) A recently-published survey of Adelaide results by Weiss (**10**).

From these surveys a composite picture is presented which leaves little doubt of the major Southern Hemisphere meteor streams, but shows that all three independent groups report additional activity, considered of reasonable or even high probability, which is not found by the other groups.

A new method of examining the validity of peaks in the rate curve is described.

2. *The problem of shower identification.* (*a*) *Clegg range–time plots.*—At visual and slightly higher rates the Clegg method of plotting individual meteors (**6, 11**) enables shower radiants passing through the aerial beams to be identified by inspection. This method was used throughout 1953 for the first Christchurch survey (**8**). Since results for 1954 were also obtained by this method, it is desirable to state the procedure adopted in grading the probability of each shower.

All daily plots were examined independently by two observers for the identification of shower envelopes. (The equipment, using 75 kW peak power pulses of 3 μs duration at 69 Mc/s, and a rotatable beam aerial, has already been described (**8**).) Maximum ranges seldom exceeded 800 km, and these largely determined the envelope apex, and hence the transit time. The width of the envelope was often so uncertain that it was impossible to extrapolate with any certainty to a theoretical horizon range of 1100 km. Consequently an error occurred in right ascension, α, in the 1953 results, which, following Keay (**7**), has now been corrected, as follows:

$$0^\circ \text{ in } \alpha \text{ at declination } \delta = \quad 0^\circ,$$
$$2^\circ \text{ in } \alpha \text{ at declination } \delta = -20^\circ,$$
$$5^\circ \text{ in } \alpha \text{ at declination } \delta = -40^\circ.$$

The 1954 results have the time correction included.

When all possible pairs of radiant envelopes had been selected and the radiants of a probable shower grouped together, its worth was assessed in the following empirical way:

$(a) = 2$ [(number of days showing radiant) − (days in between not showing radiant)].

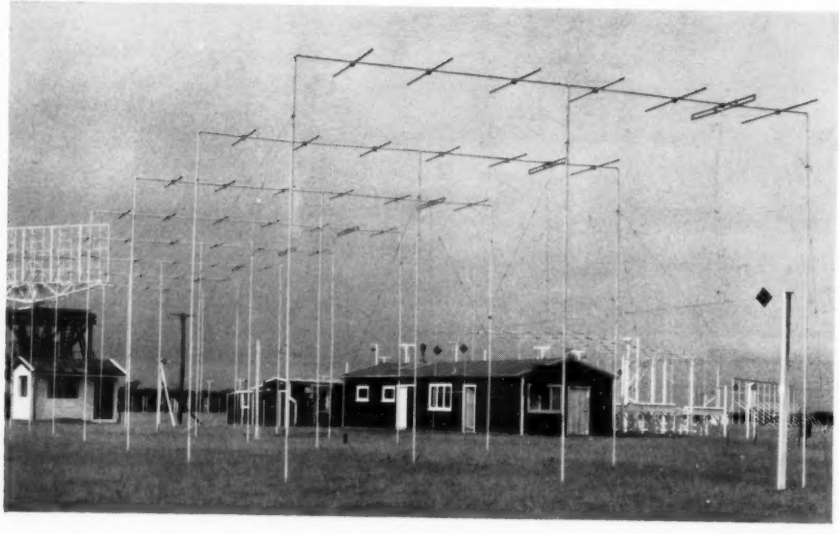

C. Ellyett et al., The identification of meteor showers

(b) = 2 (number of independent radiant values).

(c) = reasonable match in envelope contour in the two aerial directions = 0, well matched = 4, very well matched = 8.

(d) = meteor density above background, graded from 1 for very weak to 10 for very strong.

Daily shifts were overwhelmed by equipment and reading errors. However, the more compact the grouping, the more certain is a shower. Two further arbitrary figures were therefore introduced:

(e) = (number of days showing radiant) − total $\Delta\alpha°$,

(f) = (number of days showing radiant) − total $\Delta\delta°$.

If either (e) or (f) fell below zero the value was ignored. The sum of these ratings was used to grade the shower probability from A to D.

One fact which has appeared consistently is the wide spread in days of many of the showers. Admittedly when a clear-cut radiant is present there is a strong tendency to include weaker envelopes on either side of the central group of days, which would not otherwise be accepted. However, the occurrence has been so common that it must be assumed that some of the visual showers possess a fringe of smaller meteoric material. This idea of increased width is supported by photographic observations (Whipple and Hawkins (**2**)), where it is found that 50 per cent of the fainter meteors can still be identified with diffuse streams of great duration. Measurements of the radiants of many individual meteors, rather than the present statistical radar approach, may finally be necessary to resolve this point.

At high sensitivities the worth of the Clegg method rapidly deteriorates. The background rate tends to obscure the shower groupings. This may be due either to a rising background of sporadic meteors (**4, 12**) or to the presence of many interspersed minor radiants (**1, 2, 3**). Also, quite apart from this physical change, groupings enabling envelopes to be drawn cannot be discerned when the rate reaches thousands per day (**1**).

(b) *Partial rate curves.*—This method involves merely the counting of echoes for successive time intervals in a discrete range band (**7**). The basic equipment remained the same, except that the pulse width was increased to 26 μs, and the rotatable beam aerial was replaced by two fixed arrays of eight Yagi aerials spaced 1·5 λ apart horizontally, and mounted 1·5 λ above the ground. Each aerial, as shown in Plate 4, comprised seven elements mounted on a metal frame. The main beam had a half-power width in azimuth of $\pm 2°{\cdot}2$, and was centred in elevation at 9°45′ with a spread of approximately $\pm 5°$. Side lobes 42° off centre, and other minor lobes, absorbed 20 per cent of the total power.

The second vertical lobe was calculated to be centred on 27°. The lower half-power point of this lobe at 23° gives a range of 243 km for an average echo height of 95 km. If the ranges involved in the partial rate method are kept above this, the second and higher vertical lobes are of no consequence. The arrays were directed at 67°·5 and 112°·5 East of North, and fed in parallel from the transmitter. On successive pulses a gated preamplifier selected echoes from alternate arrays (**11**).

The range band of maximum sensitivity was at 350–450 km, and rate counts in this band were recorded for every 10 minute interval. The rates were then smoothed in a sliding half-hour group, in the ratio 1 : 2 : 1 for the three 10 minute

intervals. Large variations of rate can occur *within* a shower group. It is fully realized, in agreement with Weiss (5), that smoothing in this way in a search for weak radiants can cause misleading identification. Smoothing, however, was necessary in order to arrive at a more accurate time of radiant passage from the partial rate counts, and reliance was placed on multi-day occurrence of the same peaks in both aerials to remove as far as possible the chance of random coincidence being counted as a shower.

Three typical records are shown.

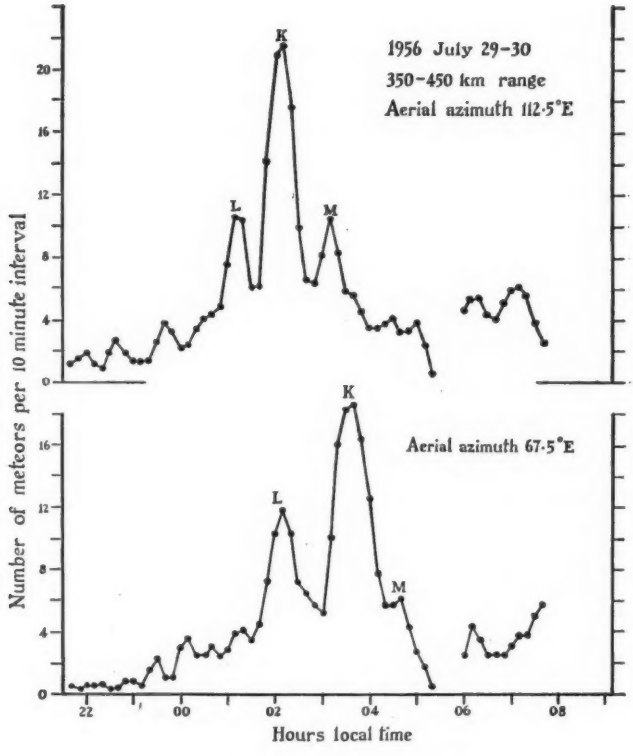

FIG. 1 (*a*).—*Partial rate counts showing definite showers.*
00^h00^m U.T. ≡ 11^h30^m N.Z.L.T. ≡ 12^h00^m N.Z.S.T.

In Fig. 1 (*a*) two certain (and probably a third) radiants passed through the aerial beam during the night. Shower K is the δ-Aquarid stream, and is one of the strongest recorded during the year. Shower L is readily recognized as the Pisces Australids. Shower M fails to pass the reliability tests given below, and is excluded, but the radiant coordinates indicate that it might be a Cetid stream.

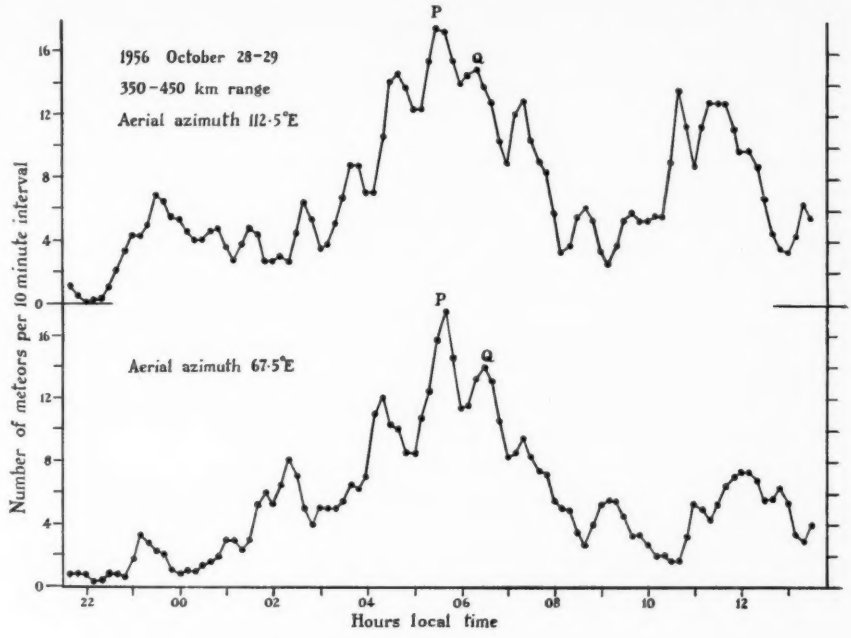

FIG. 1 (*b*).—*Partial rate counts showing a possible shower.*

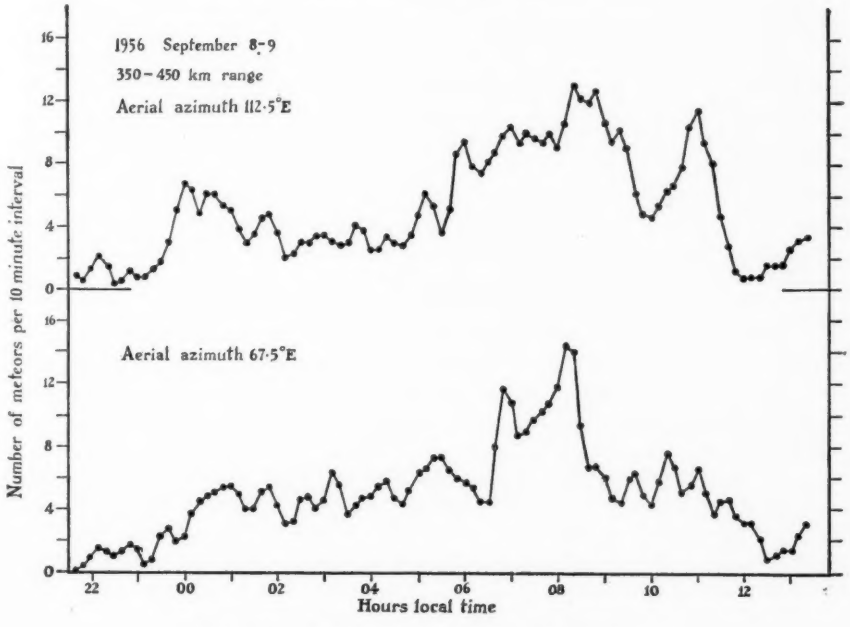

FIG. 1 (*c*).—*Partial rate counts showing no shower.*

Fig. 1 (*b*) shows a similarity of pattern, but no exact comparison between the two aerials. Both P and Q, in conjunction with adjacent days, pass the reliability test, and are recorded as a Puppis group.

Finally Fig. 1 (*c*) shows fluctuations of the same order of magnitude as the earlier examples, but no comparison between aerials is evident, and no shower is recorded.

Partial rate analysis required a new method of assessing the reality of each shower. The factors included were:

(*a*) Recognition of the rate maximum, above the background rate, for each day and each aerial separately, on the scale of certain = 8, probable = 4, doubtful = 2, very doubtful = 1, giving a value

$$\sum(\text{rate estimates})/10.$$

The scale was purposely made non-linear, as very high consistent rates mean high reality.

(*b*) Background noise level, estimated on each occasion on a scale of nil = 5, through unit steps to heavy interference = 1, giving

$$\sum(\text{noise estimates})/10.$$

(*c*) (Number of days showing radiant) − (days in between not showing radiant).

(*d*) 2(number of radiants)/$\Delta\alpha°$.

(*e*) Number of radiants/$\Delta\delta°$.

The overall reliability figure = *abcde*/10. The grading was then selected according to the scale:

$$< 100 = \text{D}; \quad 100\text{–}500 = \text{C}; \quad 501\text{–}2500 = \text{B}; \quad > 2500 = \text{A}.$$

3. *Intercomparison of probable Southern Hemisphere showers.*—The present information covers radar surveys from Christchurch during parts of 1953, 1954 and 1956. The 1956 partial rate observations in particular appeared to favour the detection of showers with declinations close to the latitude of Christchurch. This effect strongly influences the apparent rate. The system of grading, however, acts against the recognition of showers where they are non-existent. Because of this latitude effect most published shower rates do not indicate the true meteor flux. Consequently, rates are not given for the present series. It is sufficient to state that the 1953 rate was maintained at a little above the visual rate, and the 1954 series was at approximately twice the visual rate. The 1956 series was conducted at a much higher rate, giving a partial rate count averaging 70 per hour over 16 hours of observing time per day. The 1954 data filled the gaps in the 1953 survey, with the exception of January. The 1956 observations commenced on July 24 and were continuous until the end of the year. Five showers graded D only in the 1953 Christchurch survey, and not otherwise supported, have now been deleted. Unsupported D groupings in 1954 and 1956 have also been excluded.

A second group of shower information covers the visual work of various observers over many years, together with any Northern Hemisphere photographic and radar observations which extended to the Southern Hemisphere. This list, published in 1953 (**8**), has now been brought up to date by the inclusion of the more recent listings of Whipple and Hawkins (**2**), and of Fedynsky (**9**). Many of the visual results have been based on the work of McIntosh (**13, 14, 15, 16**),

which has since been shown by Hawkins (**17**) to be of high reliability. The listing by Fedynsky contains no source information.

A third independent grouping of showers is given by the recent work of Weiss (**10**), summarizing the results of a series of radar observations at Adelaide, 34° 45′ S, taken over a period of about 7 years. In this work major showers were recorded and then deleted from the data. Statistically significant rate peaks in the remaining data were selected and range–time plots for these periods drawn.

An intercomparison of the three surveys is given in Tables I, II, and III. A boundary line for all radiants in these tables has been taken at 26°·5 N, as the altitude at transit at Christchurch (43°·5 S) is then only 20° above the horizon, and showers further north than this will be poorly observed, or not observed at all.

Table I covers showers observed by all three groups, and now considered certain. Table II covers showers observed by two of the three groupings, and Table III contains all showers given in firm listings by one group, but not seen by the other two. Points of interest in the tables will now be considered.

Table I

Sagittarids.—Weiss (**10**) reports this as a newly-discovered shower in 1957 and 1958, with no trace in the Adelaide 27 Mc/s equipment in 1952, 1953, 1954 or 1956. It was, however, reported by Ellyett and Roth (**8**) in the 1953 Christchurch survey (and now also in 1954), with coordinates agreeing with the visual work of still earlier years.

Capricornids, Pisces Australids, Cetids.—These showers were suspected by Adelaide in 1953 (**10**) and the first two were listed by Christchurch in that year. They occur within a few hours of one another, as shown in Fig. 1 (*a*), and are now confirmed by Weiss (**18**). The Cetids fall into Table II. They are probably present, but due to the masking effect of the δ-Aquarids, do not reach the required grading for inclusion in the Christchurch list.

δ-Aquarids.—There is no doubt of the certainty of this group. Three of the Christchurch radiants, graded A, C and D, agree excellently with the results from elsewhere, but one graded B shows a large discrepancy in right ascension. Range–time plots frequently appear to show sub-groups, rising to high range and close together in time. The tendency has been to treat these as true sub-groups, but the lower range echoes are merged so that it is impossible to draw clear envelopes, and any error in pairing sub-groups gives a displaced radiant. (A converse error can arise if true sub-groups are merged into a single envelope.)

Puppids and Velids.—This activity is certain, and will be the subject of a separate communication.

Table II

The Arietids, ζ-Perseids and October Orionids, found by the Adelaide but not by the more southerly Christchurch surveys, are near the limit of observation at the latter site. Consequently detection is difficult. With the exception of these, and the Cetids, which have already been mentioned, Adelaide records none of the other showers in Table II.

The coordinates and dates for the Christchurch Leonids and December Orionids make them doubtful compared with the well-established northerly streams, but there is no obvious reason for their exclusion.

Table I

Showers observed by all three survey groups

Constellation	Photographic (P) or radar (R) in Northern Hemisphere; Visual (V) in Northern Hemisphere and Southern Hemisphere					Christchurch radar surveys				Adelaide radar surveys 1952–1959			
	Date	α°	δ°	Method	Author	Date	α°	δ°	Grade	Date	α°	δ°	Grade
η-Aquarids	Apr. 28–May 12	335	−1	V, R	F	1953 Apr. 29–May 4	343	0	D				
	Apr. 28–May 16	338	+1	V	M								
	May 1–6	326	−1	R	J					May 4–11	339	+2	I
	May 2–6	336	0	V, R	W								
Sagittarids	May–June	270	−30	V	F	1954 May 12–21	291	−15	C				
						,, May 28–June 14	277	−22	B	May 31	289	−18	II
	June 30–July 10	268	−20	V	M	1953 June 19–25	271	−23	C				
	July 2–19	283	−15	V	M	,, July 3–13	306	−33	B	June 9–13	304	−35	I
β-Taurids	June 24–July 6	86	+19	R	W								
	June 26–July 4	87	+20	R	J	1953 June (17)–26	84	+23	B	June			I
Capricornids						1953 June (17)–29	306	−21	B				
						,, June 29–July 13	302	−19	B				
						,, July 3–9	319	−17	D				
	July 10–Aug. 5	313	−15	V	M	,, July 21–30	323	−17	C	> July	320	−20	I
	July 17–Aug. 21	309	−10	P, R	W	,, July 29–Aug. 12	302	−11	A				
δ-Aquarids N	July 14–Aug. 19	339	−5										
S	July 21–Aug. 15	339	−17	V, R	W	1956 July 25–Aug. 7	340	−19	D				
ι-Aquarids S	July 16–Aug. 25	338	−14			1953 July 30–Aug. 7	338	−18	A	July 16–Aug. 10	342	−17	I
N	July 16–Aug. 25	331	−5										
	July 22–Aug. 9	338	−12	V, R	F	,, Aug. 1–12	322	−7	B				
	July 22–Aug. 15	341	−9	V	M	,, Aug. 2–9	331	−12	C				
	July 25–Aug. 6	339	−12	R	L								
	July 29–31	345	−20	V	H								
Pisces	July 14–Aug. 22	335	−30	V	M	1953 July 21–26	331	−27	B	> July	335	−20	I
Australids	July 26–Aug. 8	344	−32	V	M								
						1956 July (25)–(30)	320	−28	D				
Puppids						1953 Dec. 2–10	117	−25	C				
						,, Dec. 12–19	113	−16	D				
						1956 Nov. 18–21	122	−46	D				
						,, Nov. 28–Dec. 15	119	−42	D	Dec. 2–10	140	−50	I
						,, Dec. 13–25	104	−44	B	(Puppis–Velids)			
Velids	Dec. 5–Jan. 7	149	−51	V	F	1956 Nov. 28–Dec. 29	135	−47	A				

F = Fedynsky (9) M = McIntosh (13, 14, 15, 16)
W = Whipple and Hawkins (2)
J = Jodrell Bank Group (19, 20, 21, 22)
H = Hoffmeister (23) L = Lindblad (24)

(Dates in brackets indicate that the shower may have extended outside the limits shown)

1953 Clegg method
1954 Clegg method
1956 Partial rate method.

J = Jodrell Bank Group (19, 20, 21, 22)
H = Hoffmeister (23) L = Lindblad (24)

may have extended outside the limits shown)

1953 Clegg method
1954 Clegg method
1956 Partial rate method.

TABLE II

Showers observed by two groups

Constellation	Photographic (P) or radar (R) in Northern Hemisphere; Visual (V) in Northern Hemisphere and Southern Hemisphere					Christchurch radar surveys					Adelaide radar surveys 1952–1959			
	Date	$\alpha°$	$\delta°$	Method	Author	Date	$\alpha°$	$\delta°$	Grade		Date	$\alpha°$	$\delta°$	Grade
Virginids	Mar. 5–21	183	+4	V, R	W									
	Apr. 4–30	209	−10	V	M	1953 Apr. (10)–(15)	212	−7	C					
	March–May	200	−6	V	F	1954 May 12–28	221	−4	B					
Librids	Apr. 1–21	234	−21	V	M	1953 Apr. 29–May 8	230	−22	C					
Arietids	May 29–June 18	44	+23	R	W						June			I
	June	44	+23	R	J									
						,, June (17)–21	255	−20	D					
Ophiuchids	June 1–10	255	−23	V	M	1953 June (17)–28	272	−13	A					
						,, June (17)–28	266	−21	A					
						1954 May 11–23	257	−9	A					
						,, May 24–30	255	−23	B					
ζ-Perseids	June 1–16	62	+23	R	W						June			I
	June 1–16	65	+22	R	J									
Cetids	July 19–Aug. 1	2	−18	V	M	Possibly masked by δ-Aquarids					July	351	−18	I
Taurids	Sep. 15–Dec. 15	51	+14	V, R	W									
	Oct. 17–Dec. 2	52	+21	V, R	W									
	Oct. 26–Nov. 16	58	+23	R	J									
	Oct.–Nov.	58	+20	V, P, R	W	1954 Nov. 13–Dec. 2	60	+23	B					
Orionids	Oct. 14–26	90	+14	V, R	F									
	Oct. 15–25	97	+11	R	J									
	Oct. 18–26	94	+16	V, P, R	W						Oct. 21–22			I
Leonids	Nov. 10–18	150	+20	V	F									
	Nov. 14–20	152	+22	V, R	W									
	Nov. 17–18	151	+22	V	H	1954 Nov. 12–16	165	+26	D					
						,, Nov. 25–Dec. (4)	163	+25	B					
						1954 Nov. 14–Dec. (3)...	125	−3	A					
Monocerotids	Dec. 13–15	103	+8		W	,, Nov. 13–Dec. (4)...	112	−1	A					
						,, Nov. 20–Dec. (4)...	98	+8	A					
Orionids	Dec. 9–14	87	+21		W	1953 Dec. (1)–6	89	−3	D					
						1954 Nov. 20–Dec. 3	88	0	A					

Table III

Showers observed by one group only

Constellation	Photographic (P) or radar (R) in Northern Hemisphere; Visual (V) in Northern Hemisphere and Southern Hemisphere					Christchurch radar surveys				Adelaide radar surveys 1952–1959			
	Date	α°	δ°	Method	Author	Date	α°	δ°	Grade	Date	α°	δ°	Grade
Aquilids						1953 Feb. 17–22	298	−6	D d				
						1954 Feb. (2)–8	302	−2	C d				
Sagittarids						1954 Feb. (2)–6	290	−19	C d				
α-Piscids										Mar. 31–Apr. 8	340	−32	II
Sagittarids	April 1–5	280	−35	V	F								
Velids										Apr. 3–4	153	−39	II
Normids										Apr. 22–23	241	−44	II
γ-Capricornids	Apr. 29–May 7	324	−17	V	M								
Cetids										May 1–12	13	−18	II
γ-Scorpids	June 8–9	227	−28	V	F								
Eridanids						1953 June 18–21	50	−24	D				
						,, June 19–27	71	−27	B				
β-Scorpids	July 5–8	238	−19	V	M								
μ-Ophiuchids	July 5–9	259	−10	V	M								
Microscopids						1953 July 5–15	314	−33	A				
Phoenicids										July 7–22	32	−48	I
Pictids										July 10–11	80	−44	II
Aquarids						1953 July 16–25	321	+2	A				
Aquilids						1953 July 17–25	276	−8	C				
						,, July 20–Aug. 2	300	−3	A				
Pegasids	July 19–31	341	+21	V	F								
Tucanids	July 27–31	346	−58	V	F								
Sextantids-Leonids										Sep. 26–Oct. 4	155	±0	I d
Virginids						1953 Oct. 22–28	202	−16	B d				
						,, Oct. 31–Nov. 7	204	−5	C d				
						1954 Nov. 12–16	205	−15	A d				
						,, Nov. 29–Dec. 3	205	+4	D d				
Puppids						1956 Oct. 27–Nov. 2	102	−43	C				
						,, Oct. 27–Nov. 6	114	−40	B				
						,, Oct. 29–Nov. 4	127	−41	D				
Arietids	Oct.–Nov.	30	+25	V, R	F								
Andromedids	Nov. 7	22	+27	R	W								
Librids						1953 Dec. (1)–8	228	−27	C d				
						,, Dec. (1)–11	237	−19	D d				
						,, Dec. 12–20	230	−3	B d				
						1954 Nov. 12–Dec. 2	236	−6	A d				
						,, Nov. 12–30	222	−12	A d				
Phoenicids										Dec. 5	15	−55	I
Eridanids										Dec. 5–6	36	−30	II

The Virginids, found in two separate years by Christchurch, and in three other surveys, would appear to be a fairly definite shower.

Table III

The visual workers, with slight radar assistance, list 10 showers, Christchurch 9, and Adelaide 9, all of which are different. Some of the radar showers, entered as "d" in the grade column, are essentially daytime passages, and would not be found by visual observers.

Three of the Adelaide showers, regarded as certain, are in Table III. The 1956 December 5 Phoenicids is a well-recorded brief event which was missed in Christchurch due to equipment failure. For the two further showers listed by Adelaide no other evidence exists. This is surprising since the equatorial declination of the Sextantids-Leonids should make it detectable from the Northern Hemisphere, and the Phoenicids should be visible at night.

The number of isolated shower occurrences would seem to indicate that no single group of workers employs fundamentally better criteria than any other.

4. *Multiple rate-count method.*—The optimum range for echo reception with the 1956 aerial arrays is within the band 350–450 km. As the shower radiant moves through the aerial beam, rate counts will normally be lower in the 250–350 and 450–550 km range bands adjacent to the optimum. A recognizable peak count, correctly displaced in time, should still appear in these subsidiary range bands, provided the radiant remains active for the whole time of passage through the aerial beam.

The three range bands from both aerials are drawn in Fig. 2 (*a*) for the night of July 24/5 and Fig. 2 (*b*) for the night of July 25/6. The δ-Aquarid radiant (K) is present at all times and ranges. The Pisces Australid radiant (L)—present in all cases at the optimum range—is also clearly discernible in three of the four longer range strips, and possibly the fourth, but only in one of the short-range strips. The Cetid radiant (M) appears on only one of the two nights in the main range strip and is only appreciably supported in one of the other eight possible cases. The strength of the showers thus lies in the order δ-Aquarid — Pisces Australid — Cetid, which confirms Weiss's results (**18**).

Other fluctuations in the main bands are not followed in the subsidiary bands. This enlargement of the partial rate technique shows promise of being a powerful means of sorting out the significance of peaks in the rate curves. It has not yet been applied extensively to the Christchurch data.

5. *Conclusions.*—Three entirely independent and extensive sets of observations of meteor radiants extending from $\delta = +26°{\cdot}5$ to about $-50°$ have been compared. Seven showers which appear in all three surveys can be regarded as certain, and another 6 to 9 are probable. Each set gives a further 9 or 10 radiants found by that survey alone.

The radar surveys at Adelaide and Christchurch during the past seven years have both suffered from broken observing time and the troublesome effects of radio noise. Consequently, while the coverage is far better than the visual observations, the summarized results cannot yet be regarded as final for other than the major showers.

The Christchurch partial rates on first analysis showed the possibility of a subjective favouring of showers with declinations close to the latitude of

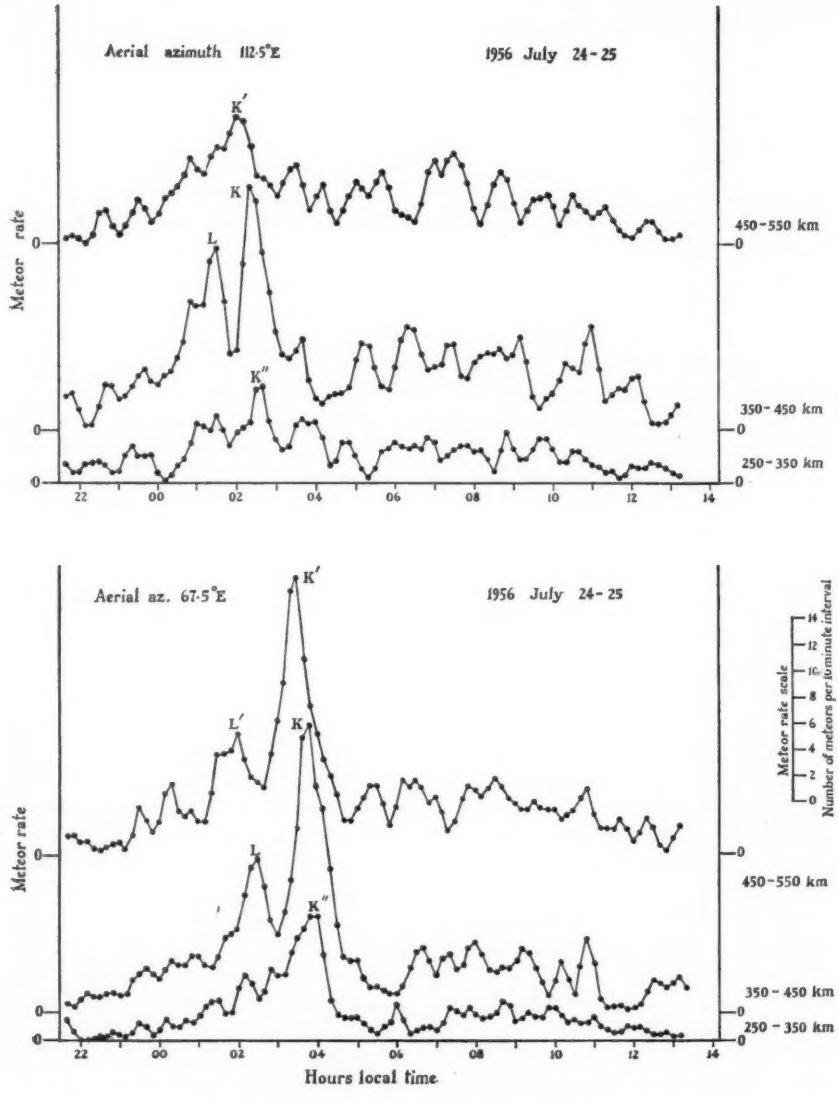

FIG. 2(*a*).—*Rate counts for multiple range bands*
K *grouping* = δ-*Aquarid radiant*
L *grouping* = *Pisces Australid radiant*
M *grouping* = *Cetid radiant* (*probable*)

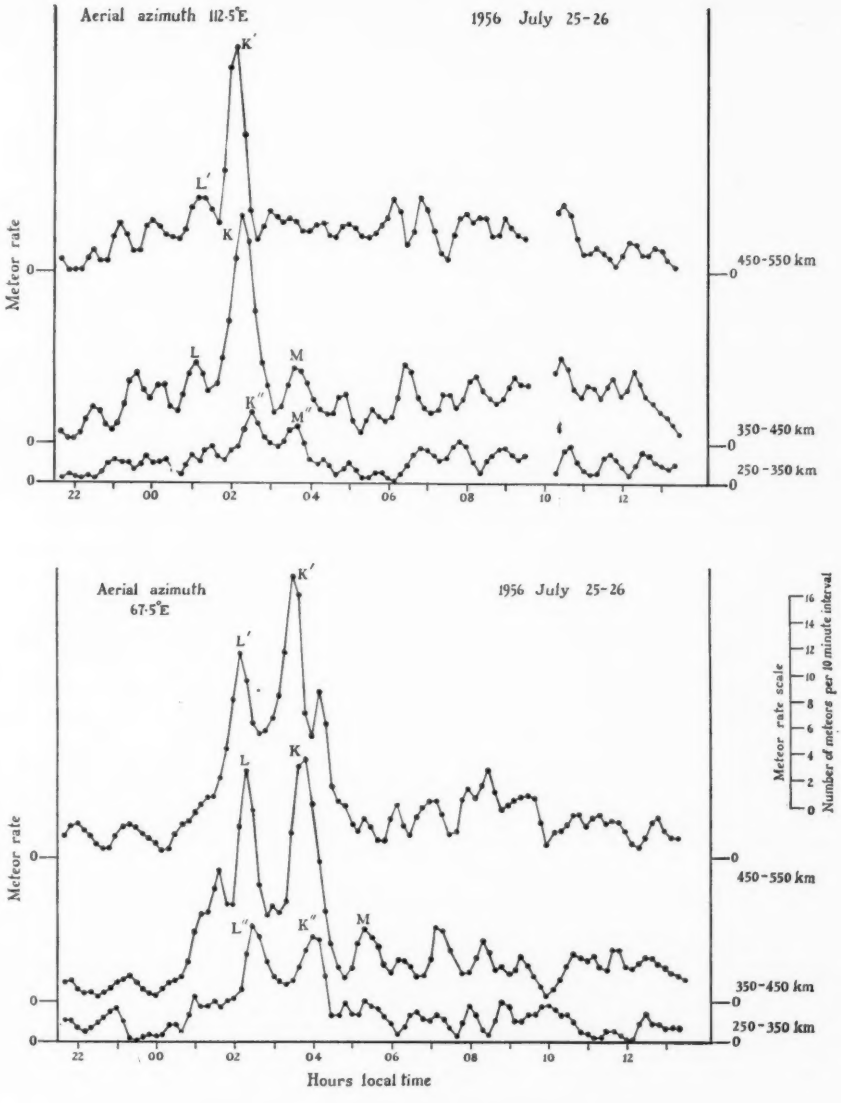

FIG. 2(*b*).—*Rate counts for multiple range bands*
K *grouping* = δ-*Aquarid radiant*
L *grouping* = *Pisces Australis radiant*
M *grouping* = *Cetid radiant* (*probable*)

Christchurch. The radiants which finally reached the requisite grading, however —with the exception of the Puppids and Velids—are not close to $\delta = -43°{\cdot}5$.

A major point of difference in the approach to the radar data is that smoothed curves with a stringent system of examination and grading are used at Christchurch. The Adelaide workers point out the dangers inherent in identifying a high rate count with shower activity, and first subtract an average monthly count. The cells which remain of high rate are used to identify their Grade II showers, and if these cells further show satisfactory range–time plots, the showers can become Grade I. It is not considered by the Christchurch group that the background count is sufficiently smooth to make this a reliable process.

Obviously no method to date is entirely satisfactory. The introduction of the multiple rate-count should result in an appreciable improvement in minor shower recognition.

6. *Acknowledgments.*—This work has been supported by grants from the New Zealand Department of Scientific and Industrial Research, and contract assistance from the Electronics Research Directorate of the Air Research and Development Command, U.S.A.F., under Contract AF64(500)-6.

Physics Department,
University of Canterbury,
Christchurch, C.I.,
New Zealand:
1961 *April* 10.

References

(1) Ellyett, C. D., and Keay, C. S. L., *Aust. J. of Phys.*, **9**, 471, 1956.
(2) Whipple, F. L., and Hawkins, G. S., " Meteors " in *Handbuch der Physik* (Springer-Verlag, Berlin), **52**, 519, 1959.
(3) Gallagher, P. B., and Eshelman, V. R., *J. of Geophys Res.*, **65**, 1846, 1960.
(4) Davies, J. G., and Gill, J. C., *M.N.*, **121**, 437, 1960.
(5) Weiss, A. A., *J. of Atmos. and Terr. Phys.*, **14**, 19, 1959.
(6) Clegg, J. A., *Phil. Mag.*, **39**, 577, 1948.
(7) Keay, C. S. L., *Aust. J. of Phys.*, **10**, 471, 1957.
(8) Ellyett, C. D., and Roth, K. W., *Aust. J. of Phys.*, **8**, 390, 1955.
(9) Fedynsky, V., " Meteors ", Foreign Languages Publishing House, Moscow, p. 81, 1959.
(10) Weiss, A. A., *M.N.*, **120**, 387, 1960.
(11) Aspinall, A., Clegg, J. A., and Hawkins, G. S., *Phil. Mag.*, **42**, 504, 1951.
(12) Kaiser ,T. R., *M.N.*, **121**, 284, 1960.
(13) McIntosh, R. A., *Trans. Roy. Soc. of N.Z.*, **63**, 433, 1934.
(14) McIntosh, R. A., *M.N.*, **95**, 709, 1935.
(15) McIntosh, R. A., *Trans. Roy. Soc. of N.Z.*, **66**, 60, 1936.
(16) McIntosh, R. A., *Trans. Roy. Soc. of N.Z.*, **69**, 392, 1940.
(17) Hawkins, G. S., *Smithsonian Contrib. to Astrophys.*, **3**, 7, 1958.
(18) Weiss, A. A., *Aust. J. Phys.*, **13**, 522, 1960.
(19) Almond, M., Bullough, K., and Hawkins, G. S., *Jodrell Bank Ann.* **1**, 13, 1952.
(20) Hawkins, G. S., and Almond, M., *Jodrell Bank Ann.*, **1**, 2, 1952.
(21) Hawkins, G. S., and Almond, M., *M.N.*, **112**, 219, 1954.
(22) Bullough, K., *Jodrell Bank Ann.*, **1**, 68, 1954.
(23) Hoffmeister, C., " Meteorströme " (Weimar) 1948.
(24) Lindblad, B., *Chalmers Tek. Högsk Handl.* No. 129, 1952.

XUM

A NOTE ON THE ORIGIN OF THE SUN'S POLAR FIELD

F. Hoyle and N. C. Wickramasinghe

(Received 1961 May 1)

Summary

A process is described whereby the Sun's polar field can be built up from comparatively small-scale magnetic loops carried outwards by particle streams. The reversal of the general polar field is associated with a reversal of the sense of the loops that straddle the solar equator.

1. *Introduction.*—The discovery (**1**), by H. W. Babcock and H. D. Babcock, of the existence of a weak general magnetic field of the Sun already raised a puzzling problem as to the mode of origin of such a field. Unless one were content with the idea that the Sun has always possessed a polar field, it appears, at first sight, to be necessary that lines of force passing from regions near the north pole to regions near the south pole be carried outwards from the solar surface by a general solar wind of particles. There is the serious objection, however, that any such line of force would have to pass from the northern region to the southern region without anywhere possessing roots below the photosphere —an unlikely requirement in view of the strong sub-photospheric convection within the Sun.

Recent magnetograph observations showing a reversal of the Sun's polar field (**2**) make these ideas seem even less plausible. While it is true that a nett reversal of polarity can be produced by carrying outwards from the Sun a sufficient number of lines of force of opposite sense to those which existed previously such a procedure increases the number of lines of force that enter and leave the Sun. Plainly the number of lines of force cannot be allowed to increase indefinitely from cycle to cycle. In such a picture, moreover, solar rotation produces a twisting of the external magnetic structure that does not accord with observation.

The reversal of the polar field, taken together with the requirement that the number of lines of force that enter and leave the photosphere shall not increase indefinitely, demands either:

(*a*) that the lines of force of one cycle are carried *back again* into the Sun before (or during) the succeeding cycle; or (*b*) ohmic dissipation in the corona is strong enough to render the concept of conservation of lines of force not even approximately valid.

The point of view of the present note is that (*b*) is the correct alternative. Reasons for believing that ohmic effects are important will be given in the next section. Once the existence of significant ohmic effects is admitted, the origin and reversal of the polar field can be understood, in terms that are free from the objections mentioned above.

No difficulty arises in transporting local photospheric fields into the corona, through the agency of localized particle streams—streams from flares, for example.

We expect such activity to lead to the emergence of loops of the type described by Gold (**3**) and by Alfven (**4**). So long as both feet of a loop lie in the same solar hemisphere no nett polarity arises from the drawing out of the loops. But if the feet straddle the solar equator then both hemispheres acquire a nett polarity. This is shown by the loops (*a*) and (*b*) of Fig. 1. And if loops that straddle the equator possess systematically the same sense in any one cycle then systematically through the cycle an excess of emergent, or entrant, lines of force will be added to the hemispheres. It is true that the nett polarity acquired in this way by a hemisphere is not initially of the form required, for initially the excess of lines of force enter (or leave) only the equatorial regions, not the polar regions. It is here that the process of ohmic dissipation plays a crucial role, however.

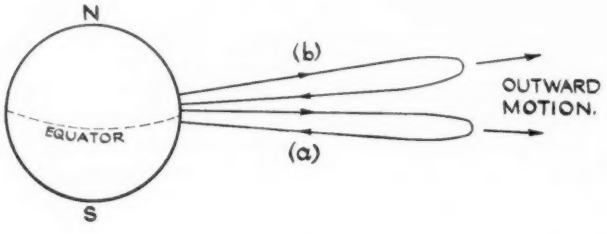

FIG. 1

Consider the outward particle motion to extend the loops of Fig. 1 effectively to infinity. The outward going lines of force of loop (*a*) tend to press against the inward going lines of force of loop (*b*). Provided ohmic effects are strong enough—and this will be considered below—annihilation of these opposed fields takes place, leaving behind the outward going lines of force of loop (*b*). The effect of cancellation between the loops is therefore to cause the lines of force that carry the nett polarity of the N hemisphere to take a step from the equator towards the pole. The effect of dissipation is thus to cause a general diffusion of the lines over the whole hemisphere. We expect a gradual drift from equator to pole of the nett magnetic polarity per unit area. In this connection it is important to realise that the magnetic polarity in high latitudes is not required to become as large as the magnetic polarity in low latitudes. Observation suggests a nett field of about 3 gauss in high latitudes, whereas the nett field near the equator could probably be as high as 10 gauss. The emphasis of the observations on polarity at high latitudes arises because at low latitudes there is the difficulty of distinguishing the nett field against a complicated background of strong local magnetic fields of both polarities.

To give a reversal in the polarity of the general field we only need a systematic reversal in the sense of the loops that straddle the equator. Lines of force of opposite polarity are then injected into each hemisphere, and proceed to diffuse over their respective hemispheres. Moreover, the existence of dissipation permits the lines of the new cycle to cancel those of the old cycle. The assumption of such a reversal at the equator does not seem at all implausible in view of the polarity reversal of the sunspot cycle. Tentatively, we set the reversal of the loops as occurring immediately after the disappearance at the equator of the

spots of the old cycle. The diffusion to the pole then occupies a period of about 5 years, during which time the new cycle develops to its maximum intensity. The switch at the pole coincides approximately with sunspot maximum. During the subsequent 5 years, as the sunspot activity declines to minimum phase, the polarity continues to increase in high latitudes, not attaining its maximum value until after the sense of the loops at the equator changes again.

The time scale for the annihilation of the opposed arms of two loops, such as those of Fig. 1, must be less by an order of magnitude than the time scale for diffusion from equator to pole—since the latter demands a number of poleward steps of the type described above. Thus if we set 5 years as the diffusion time from equator to pole, the annihilation time for the arms of two loops should not be longer than $\sim 0{\cdot}5$ years, say. It will be found in the following section that ohmic dissipation can produce annihilation in a time scale of this general order.

Manifestly, the diffusion time from equator to pole is not strictly defined. It must depend on the particular configuration of loops, and this in turn must depend on the particular pattern of solar activity. Since this is not exactly the same in the two hemispheres the diffusion times for the two hemispheres need not (and in general will not) be exactly the same. It is of interest that Babcock (**2**) reports a switch of polarity in high southern latitudes as taking place between March and July 1957, whereas the corresponding switch in high northern latitudes did not take place until November 1958.

2. *Ohmic dissipation rates.*—In Fig. 2 an idealized diagram shows a loop emerging from two patches on the photosphere. The scale of the figure is taken so large that the solar surface can be regarded as plane, and the loop as not diverging—i.e., the radial directions are essentially parallel. The figure makes clear that the loop is not an electromagnetically force-free structure. This would be given by a dipole, with its poles at the two feet of the loop. The lines of force of such a dipole are shown in the figure, and they are not at all similar to the loop. Hence to maintain the loop other forces must cancel the internal electromagnetic forces.

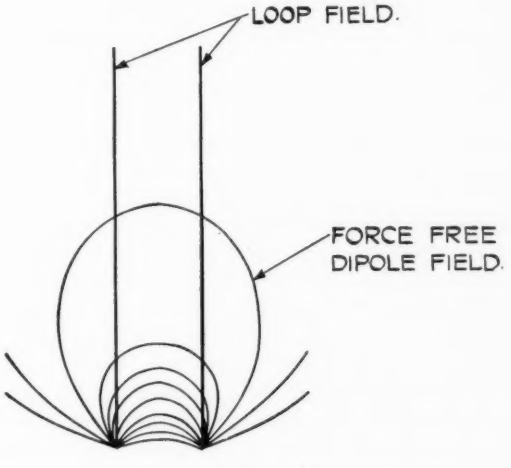

FIG. 2

The loop is initially pulled out of the Sun by the mechanical forces exerted by an outward beam of particles—say from a flare. Once the particles have left the Sun, however, the lower parts of the loop shown in Fig. 2 will bow out into an approximation to the lines of force of a dipole, unless the loop continues to be pressed inwards by external forces. The interesting case, from the present point of view, is where two such loops emerge from adjacent regions of the photosphere. Both loops will attempt to bow outwards and will press against each other. When the lines of force are directed in the same sense the mutual electromagnetic forces cause the loops to repel each other. But when the senses are opposite the forces are attractive. This is the case that relates to the discussion of the introductory section.

Opposed fields do not immediately annihilate each other, however, because the ionized gas of the corona is compressed between them until it attains a pressure adequate to keep the loops apart. This occurs when

$$\frac{H^2}{8\pi} \cong P_{gas} \cong 2\mathfrak{R}\rho T, \tag{1}$$

where H is the mean magnetic intensity within the loops, $\mathfrak{R}$ is the gas constant, T is the temperature, and ρ is the density after compression. When (1) is satisfied, a quasi-equilibrium state can be set up.

Write n for the electron density, and m_H for the mass of the hydrogen atom. Then

$$\rho \cong nm_H, \tag{2}$$

so that

$$\frac{H^2}{8\pi} \cong 2\mathfrak{R}nm_H T,$$

which gives

$$n \cong 1{\cdot}5 \times 10^{14} H^2/T \tag{3}$$

when expressed numerically. If $\bar{n}$ is the normal electron density before compression, then $\bar{n}/n$ is the linear compression factor necessary to raise the gas pressure sufficiently to keep the loops apart. The ratio $\bar{n}/n$ is large compared to unity in the cases of interest. Thus for $T = 1{\cdot}5 \times 10^6$ °K, $H = 10$ gauss, equation (3) gives $n \cong 10^{10}$ atom cm^{-3}, which exceeds by a factor $\sim 10^2$ the normal densities in the corona.

Such compressed material must tend to slide under gravity, and also to be squeezed out of the layer of separation between the opposed loops by excess gas pressure. Write L for the thickness of the layer, ΔR for its radial extension and D for its transverse extension—the distance D being of the order of the diameter of the loops. In general we expect ΔR to be greater than D, so that the layer is bounded by two faces of area $\sim D\Delta R$ and by a rim of area $\sim L\Delta R$. If material flows out of the layer across its rim with velocity V the total rate of loss of material from the layer is of order $nVL\Delta R$. If V arises from excess gas pressure then we expect $V \cong (\mathfrak{R}T)^{1/2}$, which is of order 100 km sec^{-1} for $T \sim 10^6$ °K. This is also of the order of the speed attained in a fall under gravity. In the following work V will therefore be taken as $\sim 10^7$ cm sec^{-1}, and this will be of the correct order for both a slide under gravity and for the effect of excess gas pressure (provided $\sim 10^6$ °K is a correct choice for T).

The layer also gains material, allowing it to maintain a quasi-equilibrium in which gain balances loss. This arises because of ohmic decay in the layer, which leads to lines of force diffusing through the layer in time $\sim\sigma L^2/c^2$, where σ is the conductivity given by

$$\sigma = \frac{e^2 n}{m_e \nu}, \tag{4}$$

e, m_e being the electronic charge and mass, and ν is the collision frequency between electrons and protons. For a gas at kinetic temperature T, σ can be put in the form (5)

$$\sigma \cong 2{\cdot}6 \times 10^{-13} c^2 T^{3/2}/\ln\Lambda, \tag{5}$$

where $\ln\Lambda$ is a slowly varying quantity with value ~ 20 over the ranges of T and n in question. Thus

$$\frac{\sigma}{c^2} \cong 1{\cdot}3 \times 10^{-14} T^{3/2}. \tag{6}$$

The diffusion speed v of the lines of force is given by $L/(\sigma L^2/c^2)$. Since this must be of the order of the speed with which new lines of force are added to the layer, it follows that the total rate of addition of material to the layer is $v\bar{n}D\Delta R$. Writing $c^2/\sigma L$ for v and equating to the rate of loss of material determines the thickness L of the layer, viz

$$L^2 \cong \frac{\bar{n}}{n} \cdot \frac{c^2}{\sigma} \cdot \frac{D}{V}. \tag{7}$$

The time scale τ for annihilation of the opposed magnetic fields is $\sim D/v \cong \sigma LD/c^2$. Inserting L from (7) the annihilation time is therefore given by

$$\tau \cong \left[\frac{\bar{n}}{n} \cdot \frac{\sigma}{c^2} \cdot \frac{D^3}{V}\right]^{1/2}. \tag{8}$$

With n given by (3) and σ/c^2 by (6) this can be written as

$$\tau \cong 10^{-14}\left[\frac{\bar{n} T^{5/2} D^3}{V H^2}\right]^{1/2}. \tag{9}$$

For D, H we take

$$D \cong D_0 R/R_\odot, \quad H \cong H_0 R_\odot{}^2/R^2, \tag{10}$$

R being radial distance from the solar centre, and D_0, H_0 being appropriate values of the loop size and of the magnetic field at the photosphere. Then (9) becomes

$$\tau \cong 10^{-14}\left[\frac{T^{5/2} D_0{}^3}{V H_0{}^2}\right]^{1/2} \cdot \left[\bar{n}\frac{R^7}{R_\odot{}^7}\right]^{1/2}. \tag{11}$$

$R/R_\odot$	$\log_{10}\bar{n}$ (cm^{-3})	$\frac{1}{2}\log\bar{n} + 7/2 \log R/R_\odot$
1·1	7·95	4·12
1·2	7·60	4·08
1·4	7·11	4·07
1·6	6·75	4·09
1·8	6·45	4·12
2·0	6·20	4·15
2·5	5·67	4·23
3·0	5·25	4·29
3·5	4·96	4·38
4·0	4·70	4·46

The first factor of (11) is approximately independent of R. In the above table we give values of the second factor as a function of $R/R_\odot$, the values taken for $\bar{n}$ being appropriate for the equatorial regions of the Sun at the time of sunspot minimum (**6**).

It is seen that the strong dependence of $(R/R_\odot)^{7/2}$ is closely compensated by the behaviour of $\bar{n}$. The second factor in (11) is therefore also approximately independent of $R/R_\odot$. The decay time is

$$\sim 10^{-10}\left[\frac{T^{5/2}D_0^{\,3}}{VH_0^{\,2}}\right]^{1/2}. \qquad (12)$$

As typical values we choose

$$T = 1{\cdot}5 \times 10^6\ ^\circ\mathrm{K},\ D_0 = 3{\cdot}10^9\,\mathrm{cm},\ H_0 = 10\,\mathrm{gauss},\ V = 10^7\,\mathrm{cm\,sec^{-1}}.$$

With these values (12) gives a decay time of $\sim 3{\cdot}10^7$ sec—about 1 year.

So far as our choice for H_0 is concerned, it seems unlikely that we have underestimated the decay time. H_0 could well be higher in some cases. Thus $H_0 = 10$ gauss gives $H \cong 2{\cdot}5 \times 10^{-4}$ gauss at $R/R_\odot = 200$—i.e., at about 1 AU. While this value is in accordance with the measured values of H in particle streams from the Sun, the use of (10) in calculating H requires the loop to remain radially directed without any bowing out of the lines of force. Since some bowing out probably takes place, somewhat higher values of H_0 should probably be used. With $H_0 = 30$ gauss, say, the decay takes place at $\sim 10^7$ sec.

A more serious issue concerns our use of a normal coronal value for T. The pressure in the layer is given by (1). For $H \sim 10$ gauss, $P_{gas} \cong 4$ dyne cm^{-2}, as compared with a normal coronal gas pressure of $\sim 4{\cdot}10^{-3}$ dyne cm^{-3} at $R/R_\odot = 1{\cdot}5$. To attain the required pressure in the layer the gas must be highly compressed. Under adiabatic conditions this would imply a considerable rise of temperature. For example, if the pressure were lifted by a factor 10^3 under adiabatic conditions, the density would increase by $10^{9/5}$ and the temperature by $10^{6/5}$. In such a case a temperature $\sim 10^7\ ^\circ$K, rather than $\sim 10^6\ ^\circ$K, should be used. The effect would be to increase the decay time to a value of order 10^8 sec, or more.

Although such an increase would have a seriously adverse effect on the main argument of the present paper it would have the interesting consequence of increasing the speed V with which matter would be squeezed out of the layer. Indeed, V would rise to a value comparable to the speed of escape from the Sun. The probability that an outward stream of particles might arise from adiabatic compression of gas between opposed magnetic loops is one that probably merits serious consideration.

Conduction and radiation tend to reduce the temperature within the layer. Equation (7) for L yields values of order 10^5 cm. Hence any appreciable rise of temperature within the layer leads to a large temperature gradient normal to the layer. Conduction out of the layer would reduce T almost instantaneously to a normal value, if a magnetic field were not present. We have to deal, however, with the case of conduction in a direction normal to the field. The inhibiting effect of the field then prevents a ready outflow of heat from the layer. In this connection it is noted that the time scale of relevance for the present purposes is not the time scale (12) but the time for which a particular element of material remains within the layer. This is $\sim D/V$, only about 300 sec, for $D = 3{\cdot}10^9$ cm, $V = 10^7\,\mathrm{cm\,sec^{-1}}$, and even less for larger values of V.

XUM

The situation concerning radiation appears to be critical. For ionized hydrogen at temperature $\sim 10^6$ °K, the continuum bremmstrahlung emission amounts to $\sim n$ erg gm^{-1} sec^{-1}. Since the heat capacity at $T = 10^6$ °K is $\sim 10^{14}$ erg gm^{-1}, the characteristic cooling time for hydrogen $\sim 10^{14}\ n^{-1}$ sec, which is comparable to D/V for $n \sim 3 \times 10^{11}$ atom cm^{-3}. Equation (3), for $T = 10^6$ °K and $H = 10$ gauss, gives $n \cong 10^{10}$ atom cm^{-3}. It accordingly seems unlikely that hydrogen alone could produce cooling in the required time scale for H as low as 10 gauss, although the cooling time for $H = 30$ gauss is indeed of order D/V. The cooling rate must be increased by a moderate factor above the rate for pure hydrogen, however. The contribution from helium is comparable to that of hydrogen, since the Z^2 factor in the bremmstrahlung emission compensates for the lower helium abundance. Furthermore, recombinations of electrons on heavy ions must also contribute appreciably, since such recombinations increase as Z^4, where Z is the number of charge units carried by the ion.

It does not appear unreasonable therefore to suggest that radiative cooling by X-ray emission reduces the temperature to a normal value, at any rate in cases where H is large. It is possible that temperatures less than 10^6 °K could occur in some cases, in which case the electromagnetic decay time (12) is actually reduced below the value calculated above.

A further point deserves mention. We have discussed the whole problem on the basis that the layer of separation remains a more or less plane sheet. It does not appear certain, or even likely, that this will be the case. The thin layer of separation between the loops could develop highly complex contours—it could become a 'lung', with a much larger surface area than the simple $D\Delta R$ used above. Suppose the surface area is increased above $D\Delta R$ by a factor x. Then a factor x must be included on the right hand side of (7). This implies that the ohmic dissipation per unit area of the layer is decreased by x^{-1}. On the other hand the total layer area is increased by x, so that the total dissipation in the whole layer remains essentially unchanged. The time of outflow from the layer is increased by $\sim x^{1/2}$, however, and this could be effective in enhancing the importance of radiative cooling.

3. *Coronal heating.*—Although it is not the main purpose of this note to discuss the source of the heat of the corona, it does turn out that the dissipation of magnetic energy by ohmic decay yields a degree of heating of a significant order of magnitude. Consider, first, the case of a strong loop with $H_0 = 30$ gauss. The magnetic energy per unit area (projected on the photosphere) is $\sim R_\odot H_0^2/8\pi$, this result being exact when (10) is satisfied. To produce a change of polarity of 3 gauss everywhere over the solar surface, loops of strength 30 gauss must cancel over at least 10 per cent of the surface. In this connection it may be remarked that the main dissipation probably occurs where the field is strongest, and that it is hence more realistic to regard the change of polarity as being caused by the dissipation of strong loops over a fraction of the solar surface, instead of by weak loops distributed over the whole solar surface. On this basis the dissipation averages at least $10^{-1} R_\odot H_0^2/8\pi$ per unit area for the whole surface.

If, now, the change of polarity occupies five years, the average rate of dissipation is of order

$$10^{-9} R_\odot H_0^2/8\pi \text{ sec}^{-1} \text{ cm}^{-2}. \qquad (13)$$

With $H_0 = 30$ gauss, (13) gives $\sim 2{\cdot}5 \times 10^3$ erg sec^{-1} cm^{-2}. While it is true that

this estimate falls below the normally accepted requirement for the equatorial regions of the corona by a factor perhaps as great as 10, the polarity change of 3 gauss refers more to high latitudes than to the equatorial zone. The change in the latter zone could be as great as 10 gauss, as we have already noted above. Moreover, the dissipation is most unlikely to be wholly confined to changes affecting the reversal of polarity. Cancellations between loops each of which has feet in the same hemisphere will take place, and such dissipation is irrelevant for establishing a general field of the Sun—it simply cancels one local field against another. For these reasons it appears entirely reasonable to take the mean rate of heating as $\sim 10^4$ erg cm^{-2} sec^{-1}, at anyrate at low latitudes. This is of an order to be of interest as a possible mode of heating of the whole corona.

If one turns the problem round, by taking ohmic dissipation of loops as the main mode of heating, several interesting correspondences with observation emerge. We expect the temperature T and the electron density $\bar{n}$ to be highest in regions where the loops are the strongest and the most frequent—in general in low latitudes. The typical radial streamer structure corresponds to the loops of greatest intensity. In general, the values of T, $\bar{n}$ at a particular place in the corona reflect the degree of photospheric activity, probably flare activity, that has taken place during the preceding weeks and months.

4. *The shape of the corona.*—Our final remarks concern the long term changes in the form of the corona. It is interesting that the form of the corona, as judged (7) from isophotes of the green line λ 5303, changes much more in a week than it does in two or three complete rotations of the Sun. This implies that on a time scale of a few months the shape of the corona is approximately constant, but that the shape is not axially symmetric—the rotation of the Sun and of the whole corona changes the aspect seen from the Earth.

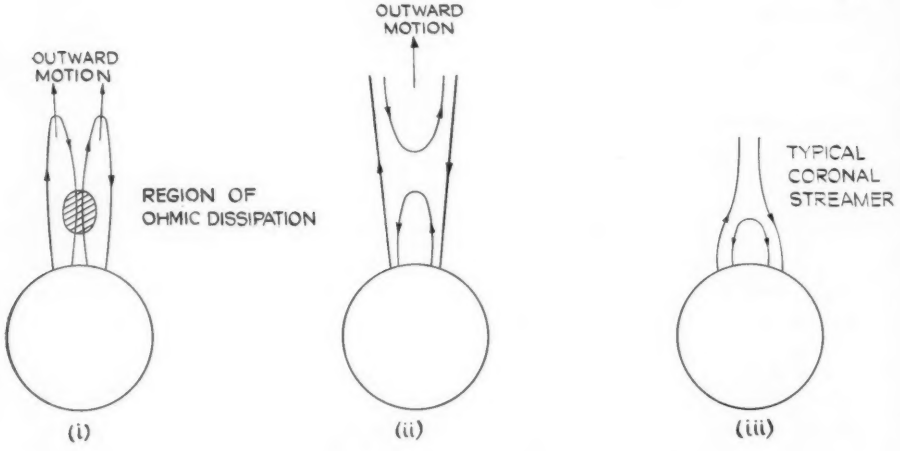

THE SCALE OF THE LOOPS IS EXAGGERATED IN ORDER TO SHOW THE FORMATION OF A TYPICAL CORONAL STREAMER.

FIG. 3

The process of heating of the corona by ohmic dissipation is clearly not axially symmetric, but depends on the precise distribution of the magnetic loops that emerge from the photosphere.

We mention also a problem concerning the rotation of the corona. It has always seemed difficult to understand why the magnetic structure of the corona did not become more and more twisted by solar rotation. While it is true that the twisting of the field would mainly occur at distances far out from the Sun, the continued accumulation of turns, producing an increasing toroidal field at large distance, would be expected to exert an increasing couple on the inner part of the corona. There are no indications of the presence of such a couple.

The resolution of this problem may lie quite simply in process of ohmic dissipation, which destroys the connectivity of lines of force passing from the Sun to distant regions. As a consequence of ohmic dissipation the connectivity of the loops of Fig 3 (i) can be changed to Fig. 3 (ii), whence the free loop can be pulled clear, leaving the typical streamer form shown in Fig. 3 (iii).

We are much indebted to Professor P. A. Sweet, who pointed out an important error in the derivation of the electromagnetic decay time as given in the first draft of this paper.

St John's College,
Cambridge:
1961 *April.*

Trinity College,
Cambridge.

References

(1) Babcock, H. W., and Babcock, H. D., *Ap. J.*, **121**, 2, 349, 1955.
(2) Babcock, H. D., *ibid*, **130**, 364, 1959.
(3) Gold, T., I.A.U. Symposium No. 6 on *Electromagnetic Phenomena in Cosmical Physics*, p. 275.
(4) Alfven, H., *ibid*, p. 284.
(5) Spitzer, L., *Physics of fully ionised gases* (Interscience, 1956), p. 81.
(6) van de Hulst, H., *The Sun* (Chicago Press, 1953), p. 263.
(7) Waldmeier, M., *Die Sonnen Korona*, Vols. 1 (1951) and 2 (1952,.

PHOTOMETRIC INVESTIGATION OF THE INNER SOLAR CORONA USING AN ECLIPSE PLATE OF 1927 JUNE 29

H. von Klüber

(Received 1961 May 9)

Summary

A number of isophotes of the innermost corona in integrated light has been determined on a very large plate obtained in 1927 by an eclipse expedition of the Hamburg Observatory, using a camera of 20 m focal length and 1 sec exposure time. The corresponding photometric intensities and electron densities could be derived using calibrated photographs of the same corona from other sources. Intensities and their gradients and amplitudes around the limb of the Sun have been determined and graphically represented within the range of 0′·7 to 3′·7 distance from the Sun's limb. Conclusions as to the formation of zones in the innermost corona have been drawn. Finally some measures of an interesting " dome-formation " of this corona are given.

General remarks.—Investigations of the innermost corona have been made since about 1932 thanks to the coronagraph method introduced by Lyot (**1, 2**) and have been carried out ever since systematically and intensively by several observers leading to a number of interesting and important results. They are nearly all based on observations in monochromatic light of the two important coronal lines λ5303 and λ6374 A. In order to investigate the behaviour in ordinary white-light of this same innermost region of the corona within a distance from the Sun's limb of only a very few minutes of arc, it is still most valuable to use large-scale corona photographs obtained with relatively short exposures during total solar eclipses. These are rare; there are in fact very few good large-scale plates of the innermost corona available for photometric investigations and so far these do not cover a sufficient number of epochs of the solar cycle. In view of the general importance attached to all investigations of the solar corona in recent years, it seems very desirable that every eclipse photograph of the corona which appears useful for such purposes should be investigated very thoroughly, so that the information it contains is really available. Photometry in integrated light informs us essentially about the electron density and its gradient; on the other hand figures given by modern monochromatic photometry with coronagraphs are essentially a function of the square of the number of free electrons and of the thermal excitation of the constituents of the corona. In recent years plates of the innermost corona obtained during the eclipses of 1905 August and 1923 September have been re-examined from the point of view of modern corona research (**3, 4**) and only a few other more recent investigations (e.g. (**5, 6**)) cover the innermost corona by very large-scale photographs.

In the large collection of eclipse plates at the Hamburg–Bergedorf Observatory, the author found an excellent plate of very short exposure time, taken at the eclipse of 1927 June 29. From the same collection the author had previously

XUM

examined a plate of the 1923 eclipse (**7**). He is greatly indebted to Professor Heckmann of Hamburg for the permission to make a photometric investigation of this 1927 plate also.

The primary aim was to derive isophotes as near as possible to the Sun's limb. These isophotes had then to be calibrated and the distribution of surface brightness, especially its radial gradient, had to be examined over a great number of position angles. An absolute calibration permitted electron densities to be derived also. Finally the possible formation of zones, the existence of which is known from monochromatic investigations of the corona, was to be studied.

The plate under discussion is of very good quality and was obtained with the unusually large focal length of 20 m. Since quite reliable relative photometric calibrations and also absolute photometric values are available for this corona this plate contains valuable and rare observational information, especially because of its large scale. A great deal of trouble has therefore been taken in examining it. Measures have been made at about 10 000 separate points, and these have been combined in a drawing of the isophotes with a diameter of more than 1 m, giving one of the most detailed photometries of the innermost corona so far made in integrated light.

Observational material.—The plate was obtained by the Hamburg eclipse expedition (**8**) of 1927 June 29 at Jakkmokk in Lapland ($\phi = 66° 36'$; $\lambda = 19° 50'$ E; altitude 240 m), using the large Hamburg horizontal camera, with a Zeiss objective of 16 cm aperture and 20 m focal length. The dimensions of the plate are 50 × 50 cm and its scale is 1 mm = 10 second of arc. The weather was very favourable and the Sun free of clouds during totality. The exposure time was 1 sec. The plate is excellent in every respect and shows a wealth of detail in the corona and in the prominences. Plate 5*a* shows a reproduction of the corona very near to the limb. Of course, as usual, many details of the original plate are lost in the reproduction. To give some idea of the connection of the inner corona with the outer corona and its well-developed streamers we reproduce a drawing from (**9**) of the outer corona of the same eclipse (Plate 5*b*).

The apparent semi-diameter of the Sun was $15' 43''{\cdot}9$ and that of the Moon $15' 54''{\cdot}4$. The position angle P of the Sun's axis was $-4°$, the heliographic latitude B_0 of the Sun's centre $2°{\cdot}7$, the longitude of the central meridian at the moment of eclipse $1°{\cdot}9$, the time of totality $5^h 45^m{\cdot}6$ G.M.T., i.e. $7^h 4^m{\cdot}7$ mean local time, and the duration of totality 37 seconds.

At the time of totality the Sun's limb showed a number of prominences which could be identified very accurately on the various plates of this corona. They do not, however, fit very well into the drawing of the prominences in (**10**); similar discrepancies have been found on other occasions (**7**). It is nevertheless important to take the prominences into account when examining the isophotes so near to the limb. They are, therefore, summarized in the following list as they appear on the original. Some of these prominences have been specially studied in (**11, 12**).

1. *P.A.* 347° to 4°, height H above Sun's limb $1'{\cdot}0$; extended high region with much detail. This is prominence *a* in (**11**) and has been treated in (**11**) and also in (**12**).
2. 11°, $H = 1'{\cdot}2$; thin, distinct, perhaps ascending prominence.
3. 28° to 35°, $H = 1'{\cdot}2$; compact and bright; in the northern part apparently in movement.

4. *P.A.* 43° to 66°, H = average 1′·0; in motion with characteristic arches known from prominence films. Arches and spikes reach up to heights of 1′·7. Centres of attraction probably at position angles 43° and 54° and perhaps also, in the bright coronal matter, at about 70°.

5. 85°, H = up to about 1′·0; here again bright prominence arches become visible, starting in the bright coronal matter in the region around position angle 74°. The centre of disturbances connected with them is probably the long-lived spot group Greenwich No. 10335.

About here is the brightest part of this corona and the electron density has its maximum as shown below.

6. 141° to 146°, H = 0′·5; low, compact and probably stationary region. Above it, and undoubtedly in connection with it, a prominent dome-formation of the corona (see below) in several concentric arches, with its base at position angles 138° and 148°. Height of the apex of the brightest inner arch about 2′·3. Another is above.

7. 165° to 167°, H = 0′·8; spikes of a presumably extended region, nearly without structure.

8. 169° to 170°, H = 0′·4; the same as No. 7. Prominences 7 and 8 noted as *b* in (**11**).

9. 178° to 180°, H = 0′·6; the same, but with a little more structure.

10. 193°, H = 0′·2; small spike.

11. 228°, H = 0′·1; spike-like, bright point.

12. 252° to 262°, H = 1′·5; the same as at position angle 85° (No. 5) but obviously due to spot group Greenwich 1032 (see below, Table I). Out of bright corona matter prominent streamers radiate with isolated bright light knots.

13. 291°, H = 0′·2; thin, faint spikes. Now follows a region of very low intensity with a minimum of the electron density as shown below.

14. 315° to 324°, H = 1′·5; compact and very bright region above a faint dome-formation. Noted as *c* in (**11**).

15. 330° to 332°, H = 0′·5; upper part only compact; faint matter streams in low arches between this and the preceding region No. 14.

16. 343° to 345°, H = 0′·2; upper spike region.

Our Plate 5*a* and also Fig. 4 in (**11**) give an impression of details in position and appearance of these prominences. In addition, we may draw attention to Fig. 2 of (**9**) which scarcely shows any resemblance to the picture of the innermost corona of Plate 5*a* except for the decrease in brightness in the north-west quadrant. A system of rays centred at a position angle of about 100° and curved very remarkably in opposite directions is a very striking feature of this corona. The plate now under discussion has no orientation mark, but there was no great difficulty in orientating it in position angle (referred to the Sun's axis and reckoned as usual from north through east) utilizing published prominence data and especially the original manuscript of the very careful observations of A. Wolfer at the Zürich Observatory from $6^h\,30^m$ G.M.T. on the same day. The small column-like prominence No. 2 at position angle 11° is very characteristic of this corona and very helpful for its orientation. The positions of the prominences entered in the above table are not precise but should be correct to within 1° and therefore sufficiently accurate for our purpose.

In recent times sunspots, and particularly the magnetic fields regularly accompanying them, have gained particular importance for the theory of the solar corona (e.g. (**13**–**17**)). They also play an important role in the exploration of the solar radiation in radio frequencies. A tabulation of those active parts of the Sun's surface (characterized by spot formation) which at the moment of totality were sufficiently near to the Sun's limb to be able to influence the

TABLE I

Active regions characterized by sunspots near the east and west limb of the Sun for the day of the eclipse 1927 June 29

Greenwich Spot No.	Heliogr. Longit.	Heliogr. Latit.	Transit through Central Meridian	Area of Umbra	Area of all spots.	Mt. Wilson No.	Magn. Field strength Mt. Wilson	Zürich No.	Remarks
			June	*West*				Rotation No. 896	
10 326	46°.5	− 8°.7	25.87	3	8			12	Group of spots with penumbra and with small spots.
10 323	52.6	− 7.9	25.41	26	148	3029	1900		
10 321	93.7	−10.1	22.30	9	45	3025	900	11	The same, but also in the preceding and in the following rotations.
10 322	96.5	−14.0	22.09	4	14	3028	900	10	Small short living group.
10 324	103.7	−29.0	21.5	6	29	3027	800	9	Group of small spots.
	136	+10	19.1			3036	200		
10 318	149.7	−24.9	18.07	8	24	3023	1100	8	Small spots.
			July	*East*				Rotation No. 897	
10 338	218°.6	− 8°.4	10.06	17	51	3045	1300	6–5	Long chain of small groups.
	226	+18	9.6			3046	200		
	229	+10	9.4			3050/1	200/500	4	Group of small spots, appeared on July 12.
	237	+20	8.8					3	Small short living spots.
10 337	250.6	− 8.7	7.7	8	15	3044	700	2	Small spot, appeared on July 1-2.
	277	+15	5.6					1	Small group.
								Rotation No. 896	
10 335	280.4	+15.0	5.38	103	655	3042	2800	22	Large group; visible to naked eye; third and last appearance.
10 334	299.6	−21.0	3.9	13	63	3041	1300	21	Group of small spots disintegrating.

Columns 1–6 according to (**18, 19, 20**).
,, 5–6 corrected values in millionths of the visible hemisphere.
,, 7–8 according to (**19**).
,, 9 according to (**20**), number of Spörer.
,, 10 according to (**18, 19, 20**).
Heliographic longitude of west limb at the moment of the eclipse: 91°.9.
Heliographic longitude of east limb at the moment of the eclipse: 271°.7.

structure of the inner corona is therefore in this case important. Indeed most of these active areas show up quite well in the intensity distribution of the present corona. At totality the longitude of the central meridian of the Sun was 1°·9. Particular spot regions near heliographic longitudes 90° and 270°, having meridian transits June 22 and July 5, are therefore of interest. They are compiled in Table I, according to the notes in (**18, 19, 20**). The outstanding brightness of the inner corona in the spot regions Greenwich Nos. 10321 and 10335 is at once conspicuous.

The Zürich sunspot relative numbers are 69·0 for the whole year 1927, 60·5 for June only and 55·4 for July. The Zürich prominence statistics show conditions typical for a time near sunspot maximum: a nearly uniform distribution of prominences in 50° heliographic latitude on both sides of the equator, a decrease in the neighbourhood of about 60° latitude and a secondary maximum towards the poles, with a rapid decrease at the poles themselves.

There was a rather low sunspot maximum at 1928·4 with a mean relative number of 78·1; the preceding minimum was at 1923·8. The phase ϕ in the spot cycle of the time T of the eclipse, following Ludendorff (**21**), is given by

$$\phi = (T-m)/(M-m)$$

where M is the time of maximum which follows T, and m the time of the minimum situated between the preceding and the following maximum. For the eclipse under consideration we obtain $\phi = 0{\cdot}89$, and we note that the corona shows all the characteristics of a maximum corona.

The determination of the isophotes.—Since the plate itself has no intensity calibration, it was necessary to proceed by first determining a family of isophotes as accurately as possible. As in previous investigations of this kind, the recording photometer available at the time could not deal with these very large plates, so that a large Hartmann microphotometer, constructed by the Askania-Werke in Berlin was used. Its measuring table permits measurements over an area 30 × 30 cm, and by reversing the plate it was comparatively easy to measure the required total area of about 40 × 40 cm. A cross-section of this photometer was reproduced in Fig. 5 of (**22**).

The illuminated spot on the plate had a diameter 1 mm (10 sec of arc). The photometer used a barrier layer photocell and a galvanometer. Even in the regions of greatest density in the innermost corona the galvanometer deflection was ample. Each isophote has been determined, as in earlier work (**7**), by moving the plate-table in small steps in two perpendicular directions keeping the galvanometer deflection constant at some chosen value. After each step the coordinates of the measuring table were read off with an error not greater than 0·1 mm, and the corresponding point immediately entered on a sheet of suitably orientated coordinate paper. To ensure accuracy in plotting, the diagram scale was five times that of the plate, but in subsequent work this very large isophote diagram proved rather cumbersome. Special readings were made at the beginning, during, and at the end of each series of measurements to check the stability of the photometer. The accuracy of the measurements was found to be excellent. This is a very simple kind of photometry. So far it has been applied to two large-scale plates, with altogether many thousands of single measurements, and it can be thoroughly recommended in cases where automatic recording is not feasible.

" 10 according to (**18, 19, 20**).
Heliographic longitude of west limb at the moment of the eclipse: 91°·9.
Heliographic longitude of east limb at the moment of the eclipse: 271°·7.

Since there were no intensity marks on the plate the steps from isophote to isophote are arbitrary, depending only on the technical circumstances of the measurement. Fig. 1 shows the isophotes, but on this reduced scale it is impossible to distinguish all the details contained in the original material. It seems justifiable and in this special case indeed necessary also to tabulate the data. This has been done in Table II. Experience with isophote diagrams from other sources has repeatedly shown how regrettable the lack of such a summary of the numerical data (which the authors must have possessed in any case) can be. Certainly most of the isophote drawings shown in reproductions contain all the measurements in a concentrated form. Nevertheless, they are often insufficient to allow accurate use of the material for other investigations, which may have other purposes in mind.

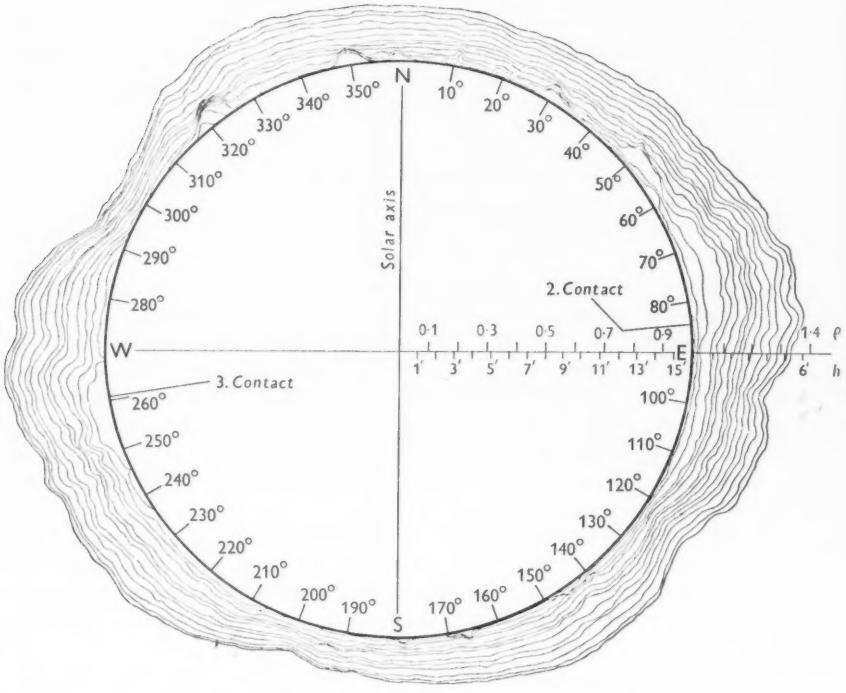

FIG. 1.—*Isophotes of the inner corona from the plate reproduced here in Plate 5 (a).*
ρ indicates distances from the Sun's centre in units of solar radii.
h indicates distances in minutes of arc.
Relative and absolute intensities of the isophotes (counted from the outside inwards) are found in Table IV.

It was found advisable to count the isophotes from the outside inward since then they can be numbered and identified more easily and safely than in the usual method starting from inside, where many isophotes are not complete. It is remarkable how little the isophotes are disturbed by the presence of prominences. Once an isophote ceases to intersect or touch the prominence it appears to continue nearly undisturbed. Distortion of the isophotes in the

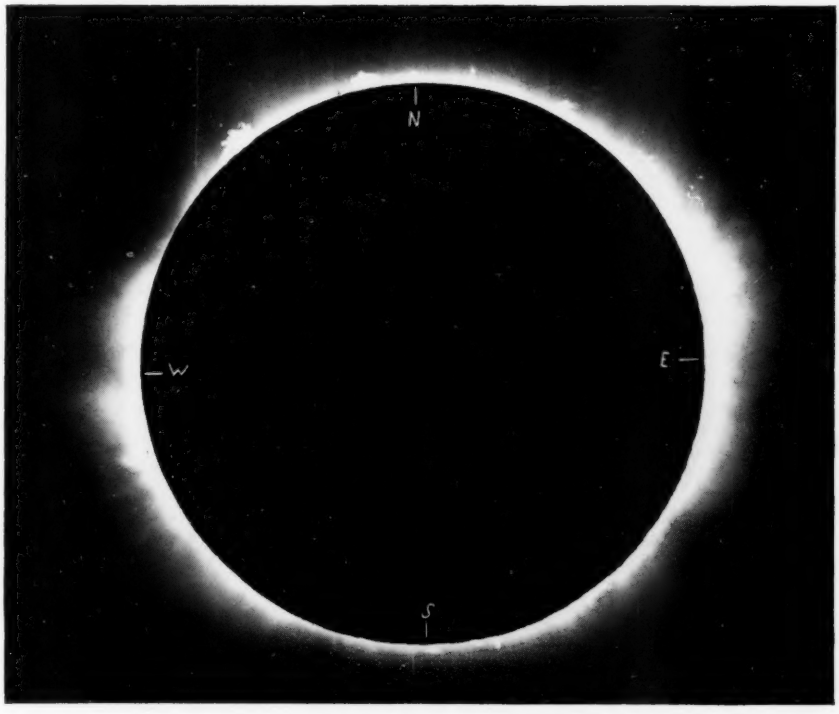

(a) Innermost corona as photographed during the total solar eclipse of 1927 June 29, with a focal length of 2000 cm, an aperture of 16 cm and an exposure time of 1 sec.

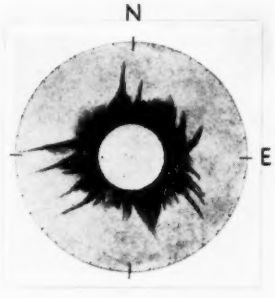

(b) Drawing of the outer corona from plates obtained during the eclipse of 1927 June 29, after (9).

(b) Drawing of the dome formation over position angle 143° for the identification of the dimensions given in Table V.

(a) Reproduction of a well developed dome formation over the prominence at position angle 143° of the corona from Plate 5a.

XUM

TABLE II

Measured distances of the isophotes from the limb of the Sun in minutes of arc.

h = mean distance from the Sun's limb in minutes of arc.
ρ = mean distance from the Sun's centre in solar radii.

Position Angle	Isophotes 1	2	3	4	5	6	7	8	9	10	11	12	13	14
	′	′	′	′	′	′	′	′	′	′	′	′	′	′
0°	2·9	2·6	2·3	2·0	1·6	1·3	1·2	1·0	0·6	0·5	0·4	0·4	0·3	
5	2·9	2·6	2·3	2·0	1 6	1·4	1·2	0·9	0·5	0·3	0·1	0·0		
10	2·9	2·6	2·3	1·9	1·7	1·5	1·4	1·2	1·0	0·7	0·5	0·3	0·1	
15	3·0	2·7	2·5	2·2	1·8	1·6	1·4	1·1	0·8	0·6	0·4	0·2		
20	2·8	2·4	2·2	1·8	1·6	1·4	1·2	1·0	0·7	0·6	0·4	0·2	0·1	
25	3·0	2·7	2·3	2·1	1·8	1·5	1·3	1·2	0·7	0·5	0·4	0·3	0·2	
30	3·2	2·7	2·4	2·1	1·7	1·6	1·3	1·1	1·0	0·9	0·8	0·7	0·6	
35	3·2	2·8	2·5	2·2	1·8	1·6	1·4	1·2	0·8	0·6	0·4	0·3	0·2	
40	3·4	3·0	2·7	2·4	2·0	1·6	1·4	1·1	0·8	0·6	0·5	0·4	0·3	
45	3·8	3·5	3·1	2·7	2·2	1·9	1·7	1·5	1·2	0·9	0·6	0·4	0·3	0·2
50	3·7	3·6	3·3	3·0	2·6	2·3	2·1	2·0	1·5	1·2	1·1	1·0	0·2	0·1
55	4·0	3·8	3·4	2·9	2·5	2·3	2·2	1·8	1·6	1·4	1·2	1·1	0·4	0·2
60	4·2	3·9	3·6	3·4	3·1	2·7	2·6	2·3	1·8	1·3	0·9	0·7	0·4	0·3
65	5·0	4·3	4·0	3·8	3·4	2·8	2·7	2·3	2·1	2·0	1·8	1·5	0·7	0·2
70	5·2	5·0	4·7	4·5	4·3	4·0	3·6	3·3	3·0	2·6	2·3	1·8	1·1	0·4
75	5·9	5·7	5·5	5·1	4·3	3·9	3·8	3·5	3·2	2·8	2·5	2·1	1·1	0·4
80	5·8	5·5	5·0	4·7	4·4	3·9	3·7	3·4	3·1	2·8	2·3	1·9	0·9	0·5
85	6·1	5·8	5·4	4·6	4·2	3·8	3·3	3·0	2·9	2·3	1·8	1·5	0·8	0·4
90	5·4	5·1	4·6	4·2	3·7	3·1	2·7	2·6	2·2	1·7	1·3	1·0	0·4	0·3
95	4·4	4·3	4·1	2·5	3·2	2·9	2·6	2·3	2·1	1·7	1·4	1·2	0·5	0·3
100	4·4	4·3	3·7	3·4	3·1	2·7	2·4	2·1	1·8	1·6	1·4	1·1	0·5	0·3
105	4·7	4·3	3·9	3·5	3·2	2·8	2·6	2·5	2·1	1·7	1·4	1·2	0·5	0·3
110	4·7	4·0	3·8	3·4	3·1	2·8	2·4	2·2	1·8	1·4	1·3	1·2	0·7	0·2
115	4·6	3·9	3·5	3·1	2·8	2·5	2·2	1·9	1·7	1·3	1·1	0·9	0·5	0·3
120	3·3	3·0	2·7	2·3	2·0	1·8	1·6	1·4	1·2	0·8	0·6	0·5	0·3	0·2
125	2·9	2·7	2·4	2·0	1·7	1·5	1·3	1·1	1·0	0·7	0·6	0·5	0·3	0·2
130	3·2	3·1	2·7	2·6	2·1	1·8	1·6	1·4	1·2	0·9	0·7	0·5	0·2	0·2
135	3·7	3·5	3·1	2·7	2·3	2·0	1·7	1·6	1·2	0·9	0·7	0·6	0·2	
140	3·7	3·5	3·1	2·6	2·4	2·0	1·6	1·3	1·0	0·6	0·5	0·3	0·2	
145	3·7	3·6	3·1	2·5	2·3	2·0	1·6	1·4	1·0	0·7	0·6	0·5	0·4	0·2
150	3·8	3·5	3·2	2·7	2·4	2·0	1·6	1·5	1·3	0·9	0·7	0·4	0·2	
155	3·5	3·4	3·1	2·6	2·3	1·9	1·5	1·4	1·2	0·8	0·6	0·4	0·2	
160	3·2	3·0	2·7	2·3	2·0	1·7	1·4	1·2	1·0	0·7	0·5	0·3	0·2	
165	3·0	2·9	2·6	2·1	1·9	1·6	1·2	1·1	0·9	0·6	0·5	0·4	0·3	
170	2·8	2·6	2·3	1·9	1·6	1·4	1·0	0·9	0·6	0·4	0·3	0·2		
175	2·5	2·3	2·1	1·7	1·5	1·3	1·0	0·9	0·6	0·4	0·3	0·2		
180	2·4	2·3	2·0	1·7	1·4	1·2	0·9	0·8	0·6	0·5	0·4	0·3		
185	2·2	2·1	1·9	1·6	1·4	1·2	0·9	0·8	0·6	0·4	0·3	0·2		
190	2·1	2·0	1·8	1·5	1·3	1·2	1·0	0·8	0·7	0·4	0·2			
195	2·0	1·9	1·7	1·5	1·3	1·1	0·9	0·8	0·6	0·4				
200	1·7	1·6	1·4	1·3	1·1	1·0	0·8	0·6	0·5	0·3				
205	2·2	2·1	2·0	1·7	1·5	1·2	1·0	0·8	0·6	0·4				
210	2·8	2·7	2·3	2·2	1·9	1·7	1·3	1·2	1·0	0·7	0·5	0·3		
215	3·4	3·2	3·0	2·6	2·2	2·0	1·6	1·3	1·2	0·7	0·5	0·3		
220	3·7	3·5	3·2	2·8	2·4	2·3	1·8	1·5	1·3	0·8	0·5	0·4		
225	4·1	3·8	3·5	2·9	2·6	2·3	1·9	1·7	1·4	0·9	0·6	0·4		

TABLE II—*continued.*

Position Angle	Isophotes 1	2	3	4	5	6	7	8	9	10	11	12	13	14
	′	′	′	′	′	′	′	′	′	′	′	′	′	′
230	4·0	3·8	3·5	3·2	2·7	2·4	1·8	1·6	1·3	0·9	0·6	0·4		
235	4·2	3·9	3·7	3·2	2·8	2·6	2·1	1·8	1·5	1·0	0·7	0·4		
240	4·2	3·9	3·8	3·4	3·1	2·9	2·4	2·1	1·7	1·3	1·1	0·6	0·3	
245	4·0	3·8	3·6	3·2	2·8	2·5	2·4	1·7	1·6	1·1	0·9	0·7		
250	4·4	4·1	3·9	3·6	3·2	2·8	2·3	2·0	1·7	1·3	1·1	0·9	0·5	
255	4·6	4·4	4·1	3·7	3·5	3·3	2·9	2·3	2·1	1·7	1·5	1·2	1·0	
260	5·0	4·8	4·7	4·3	4·0	3·8	3·4	3·0	2·7	2·2	1·9	1·6	1·2	
265	5·4	5·1	4·8	4·5	4·2	4·0	3·6	3·5	2·9	2·5	2·0	1·3	0·6	
270	5·0	4·9	4·5	4·1	3·6	3·2	2·7	2·2	2·0	1·4	1·1	0·8	0·4	
275	5·0	4·9	4·4	4·0	3·5	3·2	2·9	2·4	2·1	1·6	1·2	0·9	0·4	
280	4·5	4·3	4·1	3·8	3·4	3·2	2·8	2·6	2·1	1·7	1·2	0·9	0·4	
285	3·7	3·4	3·3	3·0	2·6	2·5	2·2	2·1	1·7	1·4	1·1	0·8	0·5	
290	2·5	2·4	2·3	2·1	1·8	1·6	1·4	1·3	1·0	0·8	0·6	0·3		
295	2·0	1·8	1·7	1·5	1·2	1·1	0·9	0·8	0·5	0·2				
300	1·8	1·5	1·4	1·2	1·0	0·8	0·7	0·5	0·3					
305	2·0	1·9	1·6	1·4	1·2	1·0	0·9	0·8	0·6	0·4				
310	2·4	2·2	2·1	1·8	1·6	1·3	1·2	1·1	0·9	0·5	0·3			
315	3·1	2·7	2·6	2·3	1·8	1·5	1·3	1·1	0·9	0·4	0·3			
320	3·3	2·9	2·5	2·3	1·8	1·5	(1·4)	(1·3)	(1·3)	(1·2)	(1·1)	(0·9)	1·0	0·2
325	3·7	3·2	3·0	2·7	2·1	1·7	1·4	1·0	0·9	0·6	0·5	0·2		
330	3·7	3·5	3·1	2·8	2·3	2·0	1·6	1·4	1·1	0·7	0·5	0·3		
335	3·7	3·3	3·0	2·6	2·3	1·8	1·5	1·2	1·0	0·6	0·5	0·2		
340	3·5	3·1	2·9	2·5	2·2	1·8	1·4	1·2	1·0	0·6	0·4	0·2		
345	3·4	3·1	2·7	2·4	2·0	1·7	1·4	1·2	1·1	0·6	0·4	0·1		
350	3·3	2·9	2·7	2·3	2·0	1·6	1·3	1·1	1·0	(0·9)	(0·9)	(0·9)	(0·8)	
355	3·3	2·9	2·7	2·4	2·0	1·7	1·4	1·1	0·9	0·7	0·5	0·4	0·2	
$h=$	3·7	3·5	3·2	2·8	2·5	2·2	1·9	1·7	1·4	1·07	0·91	0·71		
$\rho=$	1·23	1·22	1·20	1·18	1·16	1·14	1·12	1·11	1·09	1·068	1·058	1·045		

neighbourhood of prominences through scattered light in the sky, in the instrument, or through a photographic process in the plate itself, is certainly very small or even negligible in this case, as one can immediately see from Fig. 1. Measurements in Table II are bracketed if they are known to be disturbed by a prominence or suspected of having been affected by a nearby prominence.

Ellipticity of the isophotes.—First, following Ludendorff (**21**), we make use of the isophote diagram to derive the constants ϵ, a, b, which are useful empirical parameters for various purposes and of which relatively few have so far been derived from a region so near to the limb of the Sun. Taking the only isophotes suitable for this purpose, Nos. 12 to 1 (from inside outwards), our measurements give the values quoted on the left part of Table III.

For the two parameters we find

$$a = +0{\cdot}04 \pm 0{\cdot}005 \text{ m.e.}$$

$$b = +0{\cdot}14 \pm 0{\cdot}03 \text{ m.e.}$$

Ludendorff himself (**21**) has carried out a similar determination, using all photographs of this eclipse available to him in 1934. These, for comparison are quoted on the right-hand side of our Table III. His values refer essentially to much larger distances from the Sun's limb than those that could be reached here, but they still cover roughly the region of our isophotes 1 to 5. It is,

TABLE III

The parameters R and ϵ for the ellipticity of the corona after Ludendorff's (21) *definition. Left part of the table derived from the present investigation. Right part of the table as derived by Ludendorff* (21) *for the same corona.*

Present isophotes	R	ϵ	R	ϵ	Reference
12	1·07	0·04	1·21	0·06	(23)
11	1·08	0·05	1·28	0·05	(21)
10	1·09	0·06	1·35	0·02	(21)
9	1·12	0·07	1·37	0·04	(21)
8	1·14	0·07	1·42	0·05	(21)
7	1·15	0·07	1·42	0·06	(21)
6	1·19	0·08	1·72	0·06	(23)
5	1·20	0·08	1·73	0·02	(21)
4	1·23	0·08	1·84	0·05	(21)
3	1·25	0·08	1·95	0·04	(24)
2	1·27	0·08	1·97	0·05	(23)
1	1·28	0·08	2·35	0·04	(24)
			(2·81)	(0·02)	(24)
			(3·69)	(0·04)	(23)

therefore, of interest to use them for comparison since in this way we obtain a complete system of data for the same corona, covering the range for Ludendorff's quantity R from $R=0{\cdot}07$ to $R=3{\cdot}69$. His parameters are:

$$a_0 = +0{\cdot}049 \pm 0{\cdot}009 \text{ m.e.}$$
$$b_0 = -0{\cdot}006 \pm 0{\cdot}012 \text{ m.e.}$$

The agreement of Ludendorff's a_0 with our a is very satisfactory. This shows again (**25, 26**) that the value of the general ellipticity for mean distances from the Sun can be determined comparatively well. The rather large size of b is obviously caused by the fact that our values of ϵ increase appreciably from within outwards. Since $a+b$ is the flattening at the distance $R=2$ this increase necessarily produces a value of b which is too large. It is well known, and is confirmed by Ludendorff's values, that this increase does not continue if we go farther outwards. Indeed, Ludendorff's b, which is practically zero, is the correct one for this eclipse.

Mikhailov (**27**) has represented the isophotes of the same corona approximately as ellipses. Accordingly, his ellipticity is $c=(\alpha-\beta)/\alpha$ where α is the major and β the minor axis of the ellipse, and he finds:

α	c
2·5	0·09
2·0	0·08
1·5	0·07
1·0	0·04

Tables III and IV and Mikhailov's values show that ϵ at first increases slightly from the Sun's limb outwards. This has been observed at many eclipses (**21, 25**). Farther out still, ϵ decreases again, and the isophotes become more and more circular. During the eclipse of 1905 August 30, however, ϵ appears to have decreased outwards everywhere (**3, 4**).

In monochromatic light of the corona emission lines the ellipticity of the corona (so far as it can be determined at all) seems much more pronounced (**28**).

Calibration of the isophotes.—By a happy chance we can determine the relative intensities for our isophotes with comparatively great accuracy: three other expeditions obtained photographs of this corona, and these were fortunately provided with photometric calibrations.

J. Balanovsky and E. Perepelkin (**23**) have published results from the Pulkova Expedition to Northern Sweden near Malmberget ($\phi = 67° 10'{\cdot}6$, $\lambda = 1^h 22^m{\cdot}8$ E.Gr.; altitude 490 m). These photographs are calibrated for relative intensities, and the measurements of the authors, which approach the Sun's limb down to about $\rho = 1{\cdot}04$, are among the very few careful photometries of the inner corona in this range (ρ is the apparent distance from the Sun's centre expressed in units of the Sun's radius). From the same eclipse also R. Mikhailov (**27**) published carefully derived isophotes using calibrated photographs obtained by the expedition of the Russian Astrophysical Institute to Malmberget. His measurements approach the Sun's limb almost to $\rho = 1{\cdot}02$. A most valuable study of this particular corona is furthermore available in a spectrophotometric investigation by A. Pannekoek and N. W. Doorn (**11**). Their results are derived by an entirely different method, using a prismatic camera of only 27 cm focal length, and are calibrated in absolute units of the surface brightness of the Sun's disk.

The relative intensity values as given in (**23, 27**) are very well suited for a first calibration of our isophotes on a relative scale. Unfortunately none of the three authors has published his values in sufficient detail to allow calibration

TABLE IV

Calibration of the isophotes

1	2	3	4	5	6	7	8	9	10
1	1·23	3·72	3·83	3·82	3·79	3·77	3·50	7·62	7·77
2	1·22	3·75	3·85	3·83	3·81	3·80	3·52	7·66	7·80
3	1·20	3·79	3·88	3·89	3·86	3·87	3·57	7·72	7·85
4	1·18	3·89	3·96	3·97	3·95	3·94	3·66	7·79	7·91
5	1·16	3·97	4·04	4·03	4·01	4·01	3·72	7·86	7·97
6	1·14	4·06	4·11	4·12	4·10	4·09	3·81	7·93	8·04
7	1·12	4·17	4·17	4·17	4·17	4·17	3·88	8·01	8·12
8	1·11	4·23	4·24	4·19	4·22	4·21	3·93	8·05	8·15
9	1·09	4·24	4·31	4·27	4·27	4·28	3·98	8·12	8·24
10	1·068	4·48	4·39	4·37	4·41	4·38	4·12	8·19	8·32
11	1·058	4·54	4·43	4·41	4·45	4·43	4·16	8·23	8·37
12	1·045	4·60	4·46	4·47	4·51	4·48	4·22	8·27	8·43

1. Number of isophotes counted from outside inwards.
2. Mean distances from the Sun's centre in solar radii.
3. Log relative intensities after J. Balanovsky and E. Perepelkin, Table 7 of (**23**).
4. Log relative intensities after A. Mikhailov, Table 4 of (**27**).
5. Log relative intensities after A. Pannekoek and N. W. Doorn, Fig. 7 and Table 13 of (**11**).
6. Means of the log of intensities of Columns 3–5, adopted for the calibration of the isophotes of Fig. 1 of this paper.
7. Log absolute intensities in units of 10^{-10} of the average brightness of the Sun's surface for the model of a maximum corona after v.d. Hulst, Table 10 of (**29**).
8. Log absolute intensities in the same units as in Column 7, after A. Pennekoek and N. W. Doorn, Fig. 7 and Table 13 of (**11**), as adopted in this paper.
9. Log electron density N_r per cm^3, calculated from the figures of Column 8 and adopted in this paper.
10. Log electron density N_r per cm^3, for the model of a maximum corona after v.d. Hulst Table 10 of (**29**).

of our own measurements point by point, or at least along radii at certain desired position angles. The following method (as in (**7**)) has therefore been used. The distance from the Sun's limb was determined for each isophote for position angles 5° apart. These values are given in Table II. With the exception of the bracketed values they were combined into means giving the average distance of any particular isophote from the Sun's limb. These mean values are entered at the foot of Table II. Isophotes 13 and 14 are unfortunately not complete and thus their mean distances above the limb could not be derived sufficiently accurately by this method. The values of h and m_0 were taken from (**23,** Table IV), and from (**27,** Table 4). From these data we can derive immediately the relative differences in brightness between all our isophotes. Finally, in order to obtain values which can be compared with each other and also directly with the well-known data compiled by Baumbach, as used in van de Hulst's model (**29**), our seventh isophote which corresponds approximately to the centre of the region we are examining, with $\rho = 1{\cdot}12$ ($h = 1'{\cdot}9$), was assigned a relative $\log I = 4{\cdot}17$. This is the value given by the van de Hulst model for a maximum corona at this distance. The values according to (**23**) and (**27**) represent two systems which are essentially independent and probably of about the same weight. They are entered in columns 3 and 4 of our Table IV. Of course it must be remembered that the measurements of (**23**) and (**27**) themselves (but not of (**11**)) have contributed to van de Hulst's model so that the comparison mentioned is not totally independent. However, the van de Hulst model depends also on several other measurements within the range discussed here.

Furthermore, Pannekoek and Doorn's (**11**) Tables 13 and 15 and Fig. 7 give relative as well as absolute intensities for the brightness of the corona as a function of the distance from the Sun's centre. Using these values as given for the readings of the Opta plate with a slight correction we can derive from this paper a third and again entirely independent relative calibration of our isophotes. This third relative calibration, normalized in the same way as the others, gives values entered in column 5 of our Table IV. If one remembers the difficulties of making intensity calibrations at eclipses, these three independent sets of figures must be considered to be in remarkably good agreement. We therefore consider it justifiable to adopt the simple mean of the three, as given in Table IV, column 6, to represent the relative intensities of our isophotes. A comparison with the figures of the van de Hulst model in column 7 of the same table shows that within the range dealt with here our relative calibration is practically identical with that of the model.

Next, in order to obtain absolute intensities also, and later electron densities, we have made use of Pannekoek and Doorn's absolute calibration (**11**), and expressed the results in the same units as used in the van de Hulst model, i.e. 10^{-10} of the mean brightness of the Sun's disk. These absolute intensities are entered in Table IV, column 8. They are systematically slightly smaller than the figures of the model for maximum corona, but still well within the range between maximum and minimum corona models. Remembering that Pannekoek and Doorn's original absolute figures were based on readings which needed several corrections to convert their spectrophotometric values from a low dispersion spectrum of the corona into an absolute calibration for integrated corona light, the close agreement must again be considered as very satisfying,

since an error of a factor 2 could well be tolerated under such conditions. Adopting for our isophotes the absolute intensities of column 8 we have also calculated electron densities per cm^3. These are entered in column 9 and can be compared with the figures for the model corona shown in column 10. Here again an error of a factor 2 would be tolerable. Pannekoek and Doorn (**11**) have themselves also calculated electron densities, using somewhat rounded-off figures and without taking into account the limb darkening. Their figures for the electron densities from their Table 15 are therefore somewhat larger than ours and practically identical with van de Hulst's figure for the model and maximum corona. As a result of these calculations we believe that the *relative* intensities as well as the *relative* electron densities discussed here are quite reliable and are in fact in very good agreement with the van de Hulst model; the absolute figures may be right to a factor about 2. We remember also that the 1927 corona was photographed near a very low maximum and it may well be that intensity and electron densities were indeed rather below those of a model intended to represent average maximum solar activity.

Gradients of brightnesses and intensities.—The much discussed law of the average radial distribution of surface brightness of the corona will not be derived in detail from the present material. We cannot expect to get new results since this had already been done with the measurements we have used from papers (**23, 27**). The close agreement with the van de Hulst model indicates that Baumbach's empirical law for the intensity distribution will on average also represent our measurements satisfactorily. Omitting the outermost isophotes, the mean values of Table IV can be well represented by the empirical expression

$$J(\rho) = 2{\cdot}54 \times 10^4 / r^{11}$$

for $1{\cdot}04 < r < 1{\cdot}25$ and with units 10^{-10} of the average brightness of the Sun.

It is, furthermore, of interest to consider the variations in the intensities of the corona at a fixed distance from the Sun's limb. Comparatively few of these circles, concentric with the Sun's centre and lying near the limb, are covered completely by isophotes for which we have reliable intensities. The values of $\log J$ were first plotted against position angle for fixed distances from the limb ($1'{\cdot}0$, $1'{\cdot}5$, $2'{\cdot}0$ and $2'{\cdot}5$) and these four diagrams were then combined in Fig. 2*a*.

Some values disturbed by prominences or by other causes or insufficiently covered by our intensity range have again been omitted. There are some insignificant deviations from Table V because of this or because of rounding of errors in the figures. Despite small irregularities in the run of the points caused by the complex structure of the corona, Fig. 2*a* is particularly helpful in visualizing the whole intensity distribution. It should be studied in connection with the direct photographs in Plates 5*a* and 5*b*. The behaviour of the intensities along the Sun's limb and the position of the maxima and minima stand out clearly. The known maxima about the spot zones (in our case symmetrical), and the minima near the Sun's poles become immediately obvious. There are indications of secondary maxima and minima as well but these can be regarded as real only if also found on other similar photographs of the corona. This matter must remain uncertain for the present although of course it is tempting to think that we have here the secondary zones of coronal activity as found in monochromatic observations. Of course, one should in any case bear in mind that some of these features may be peculiar to this particular corona. A comparison

with similar investigations of the inner corona on large-scale plates which we hope will be made in future is therefore necessary before any general law can be derived with certainty.

There are outstanding intensity maxima with amplitudes of 0·35 and 0·40 in log$J$ near position angles 75° and 260°. The maximum near 75° corresponds obviously to the very active long lived spot at longitude 280°, Greenwich No. 10335 (Table I). The activity of the chromosphere below this part of the corona shows itself also in the appearance there of typical spot prominences.

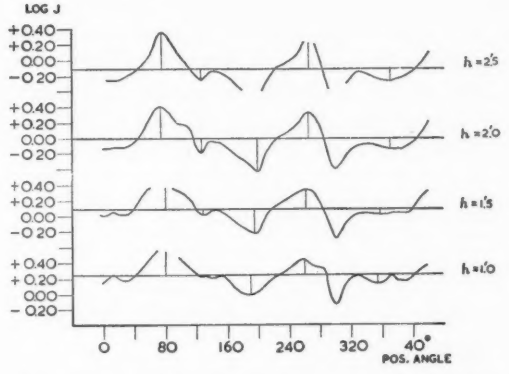

FIG. 2*a*.—*Log of intensities J against position angle for four different heights h in minutes of arc over the Sun's limb.*

Sunspot magnetic fields of the order of 3000 gauss most probably existed in this region (**19**). The other intensity maximum at position angle 260°, if assigned to longitude 93° quite near the limb, coincides with the small spot group Greenwich No. 10321 which survived for more than four rotations. The exact coincidence of the two maxima just mentioned with these two spot groups near the limb is certainly not fortuitous and is presumably the cause of the asymmetrical location of the maxima relative to the equator. Higher up in the corona this asymmetry becomes hardly noticeable (Fig. 2*a*). The two small secondary maxima which can be suspected at position angles 145° and 330° both lie outside the spot zone. There may perhaps be some connection with the very active secondary zones of the corona. On the other hand the two other corresponding secondary maxima do not appear in the curve of Fig. 2*a*. Principal minima with amplitudes similar to the maxima can be seen distinctly at the position angles 200° and 300°. The first and the last of these correspond perhaps to the known polar minima.

From the figures and from Table II we can see that in the range $h = 1'{\cdot}0$ to $2'{\cdot}5$, log$J$ varies along the Sun's limb by about 0·8 or, in intensity, by about 1 : 6, with principal maxima having an amplitude 0·4 in log$J$ in the neighbourhood of the spot zones and with principal minima of the same amplitude at position angles 200° and 300°.

We have in addition used values of log$J$ taken from the whole material of Table II and have derived as many values as possible for the gradient $a = -d(\log J)/dh$. In this expression h denotes the distance from the Sun's

limb in minutes of arc. The values of these gradients have been used by Waldmeier (**30**) and many other authors. They have a certain interest in view of the corresponding values based on numerous monochromatic corona observations available from coronagraphs. Our figures for a were compiled in a table in steps of 0′·5. It is somewhat regrettable, but unavoidable because of the method used in deriving our intensity values, that neither the isophotes nor their gradients could be traced as near to the Sun's limb as one would like. This table certainly shows that at $h = 1'{\cdot}0$ we have on the whole a gradient of 0·3, decreasing to 0·2 beyond $h = 4'$. Where the isophotes approach the Sun's limb the gradients at $h = 1'{\cdot}0$ clearly increase. In other cases the gradient is abnormally small, probably 0·2. This result had also been found for the corona of 1905 August 30 (**3, 4**) but here it is much more pronounced. It appears that in this respect the gradients have some similarity to the monochromatic gradients for the corona line λ 5303 A. For these for example Waldmeier (**30**) has found values of a between 0·3 and 0·45.

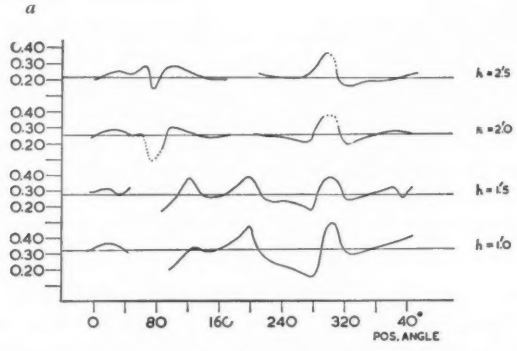

FIG. 2*b*.—*The gradient* $a = -d(\log J)/dh$ *against position angles for four different heights* h *in minutes of arc over the Sun's limb.*

Furthermore, the material leaves no doubt as to the fact that the gradients increase only in a general way as we go from the outer corona inwards; in fact they reach a maximum in the neighbourhood of $h = 1'$ or 1′·5 after which they decrease slowly. This too, has already been pointed out earlier (**3, 30, 31**). Although not all our gradients come sufficiently near to the Sun's limb, a critical examination of the figure leaves no doubt as to the reality of this behaviour. For the polar region we estimate our gradients as about 0·3 and for the equatorial zone $< 0{\cdot}2$. The behaviour of the gradients may be conveniently surveyed by plotting them against position angle as in Fig. 2*b*. Because of the incompleteness of some isophotes we were obliged to restrict ourselves to four distances from the Sun's limb, 1′·0, 1′·5, 2′·0 and 2′·5 (Fig. 2*b*). At 2′·5 the variation of the gradient is already rather small so that the general picture from here onwards becomes rather uncertain. Some gradients, possibly falsified by prominences or uncertain for other reasons, have been omitted in the diagrams. Because of the complicated fine structure of the corona it is not surprising if the sequence of gradients fails to give a smooth curve. Besides a remarkable scatter we can easily recognize a minimum in the gradients in the vicinity of position angles 70° and 270°, e.g. in the brightest regions of the corona (compare Plate 5*a*). A very clear

maximum lies at position angle 300° and a less pronounced one possibly near 200°. Fig. 2*b* also shows at once the variations in the size of the gradients. The close relation between the gradients and the behaviour of the brightness along the Sun's limb is clearly indicated.

It is now generally accepted that one can explain the brightness differences in the corona as resulting from variations in the electron concentration. In this way one can obtain from the observed intensities an approximate picture of the prevailing electron densities. Although in detail the phenomena are more complicated, photometry alone is insufficient to justify more than approximate estimations. An elegant way for calculating the electron density from the observed intensity has been pointed out by K. Schwarzschild (**32**). Later, such calculations have been carried out for instance by Baumbach and van de Hulst (**33**) where details of the mathematical treatment can be found.

One must remember that the procedure generally followed supposes a spherically symmetrical form of the corona in the region under consideration. This assumption will certainly not be exactly fulfilled in our case. However, graphical integration shows immediately that for the case considered here only comparatively near to the Sun's limb are there sufficient electrons to give any substantial contribution. It must therefore be possible to state at least the order of magnitude of the electron density required by the photometry of the present paper because the observed intensities $J(\rho)$ for our purposes can be represented at different position angles always very well by simple power series of the form $J(\rho)=K/\rho^m$, K being a constant and ρ as usual the distance from the Sun's centre in units of solar radii. K and m, of course, will be somewhat different for different position angles.

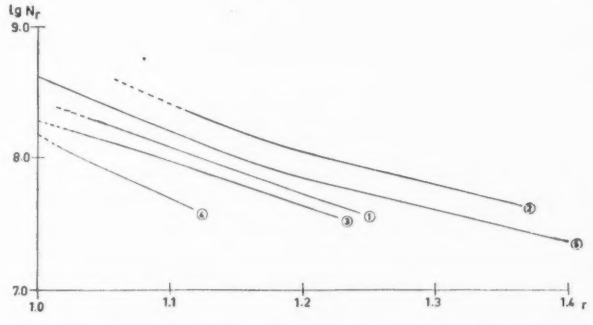

FIG. 3.—*Log of the electron density N_r per cm³ as a function of the distance from the Sun's centre in units of solar radius r.*
(1) *average values for the present corona,*
(2) *at position angle* 80°.
(3) *at position angle* 150°.
(4) *at position angle* 300°.
(5) *for the v.d. Hulst model* (**29**) *for maximum corona.*

As mentioned before we have first calculated the average electron density for the whole present corona, using the photometric values of Table IV, column 8. These are entered in column 9 of the same table and can be compared conveniently with the figures for van de Hulst's (**29**) model for maximum corona as entered in column 10. Furthermore, the electron densities for some typical position

angles of our present corona have been examined, the calculations being made with rounded-off figures. Fig. 3 shows electron densities as a function of radius for three different position angles: viz. 300°, which is a region of small brightness; 80°, a region of great brightness, and 150°, an average region which happens also to be near to the dome formation mentioned below. The dashed parts of the curve are based on extrapolations of our photometric measures; they are given merely to provide some rough numerical idea but should not be regarded as very reliable. Nevertheless, one can see that at about $r = 1{\cdot}1$ the electron density at the Sun's limb may well vary with position angle by a factor 10. The highest values are over the two spot regions at position angle 75° and 260°.

Fig. 3 also gives electron densities for the whole corona (from Table IV, column 9) as well as the electron densities for the van de Hulst model maximum corona. There are noticeable similarities to the corona of 1945 July 9, of which a careful photometric study was made by J. M. Ramberg (**5**), who at several places measured down to $\rho = 0{\cdot}01$. Fortunately he has published his photometric data in sufficient detail. Over a range of radii similar to that covered in the present paper, the intensity distribution in the 1945 corona can be represented satisfactorily by an expression of the form $J(\rho) = K/\rho^m$ with m varying around 7 to 10. The 1945 electron densities at small radii appear also to have varied over a range of about 1 : 10, and again the largest electron densities occurred above the spot zones and the equatorial region. In 1945 important spot groups appear near the limb at position angle 70°, 110° and 240°, where the corona measures show small values of m, i.e. high electron densities. A similar behaviour has also more recently been found by A. Wallenquist (**6**) for the corona of 1954.

With the values of the electron densities N_r for different distances r, taken for instance from Fig. 3, and assuming the corona to be a more or less isothermal atmosphere, one can derive approximate figures for the electron temperature T, by using the equation of hydrostatic equilibrium. Knowing the density gradient of N one can write,

$$\frac{6{\cdot}9 \times 10^6}{T} = \frac{d(\log N_r)}{d(1/r)} + \frac{d \log T}{d(1/r)} .$$

To a first approximation we may neglect the temperature gradient; its value is not known for certain, and recent interferometric observations of the corona lines (**34**) seem once more to indicate a fairly uniform temperature distribution. In this way one obtains approximate temperatures between $1{\cdot}4$ and $2{\cdot}1 \times 10^6$ degrees. Apart from the absolute values of these figures it is interesting to see, by an actual example, how large a temperature difference can be found for different position angles in one and the same corona. The importance of such differences in relation to the general problem of temperatures within the corona has been pointed out recently again by C. W. Allen (**35**) and A. Unsöld (**36**).

Dome formation.—Finally, we would like to discuss briefly a certain feature of this corona, which appears to have some importance for corona theories. Above the flat prominence at position angle 130° to 137° the plate examined here shows a very beautiful example of the well-known arc or dome formations. This part of the corona is reproduced separately in Plates 6*a* and 6*b*.

There are less conspicuous examples of similar features above the prominence at position angle 320° and again at position angle 30°. The first arch is also clearly visible on an excellent Hamburg reproduction on Plate 1 in (**8**).

The arch formation at position angle 143° has also been pointed out by J. Balanovsky and E. Perepelkin (**23**) and they have published a number of isophotes of this region drawn on a large scale. The original of our own isophote drawing shows this phenomenon very clearly, although it is not so easily distinguished on the very much reduced reproduction of Fig. 1. Inspection of the plate shows clearly a somewhat darker region situated above the prominence and above this several wide arches in a concentric arrangement. The higher arches are not seen complete, probably because of insufficient exposure time. We find that quite generally there is a noticeable decrease in the brightness of the corona over every prominence. For instance we find this phenomenon quite distinctly over the prominence at position angle 320° and small depressions of the isophotes above various prominences have frequently been noticed in earlier works. A careful examination of suitable original photographs has made it clear that these appearances cannot be attributed to purely photographic effects. Were photographic effects responsible, halo formation would show itself also over the Moon's disk, and effects caused by the developer can certainly be excluded because some prominences of a wide range of brightness on the same plate show no clear dome formation.

There is good quantitative agreement between our photometric measurements of the arches at position angle 143° and the reproduced enlarged curves of Fig. 2 in (**23**). In the dark space above the prominence the isophotes dip towards the limb, the depression amounting to about $0^{m}\cdot1$ or $0^{m}\cdot2$. The bright arches on the other hand show an increase in brightness of $0^{m}\cdot1$ to $0^{m}\cdot2$. Since very few measurements on original large-scale plates of such features have been so far available, we give below the outer dimensions of these structures, as taken directly from the original plate. The notation is that of Plate 6*b*. The base

TABLE V

$L = 143°$ P.A.

$JK = 5'\cdot2 = 223\,000$ km		
$GH = 2'\cdot9 = 128\,000$,,		
	Dark arches	
	$ED = 0'\cdot6 = 25\,000$ km	
$FE = 1'\cdot1 = 47\,000$,,	$CB = 0'\cdot5 = 22\,000$,,	
$FD = 1'\cdot7 = 73\,000$,,		
$FC = 2'\cdot5 = 110\,000$,,	*Bright arches*	
$FB = 3'\cdot0 = 131\,000$,,	$DC = 0'\cdot8 = 36\,600$ km	
$FA = 3'\cdot7 = 161\,000$,,	$BA = 0'\cdot7 = 29\,200$,,	

points *G* and *H* lie at position angle 138° and 148°. The two outer, well-defined arches seem to have their base in the lower boundary of the corona while an inner arch only faintly visible appears to rest at its centre on top of the prominence. The somewhat distinct arch over the prominence at position angle 220° gives the same impression. Another similar arch formation in the corona of the eclipse of 1926 January 14 has been described earlier by the present author (**26,** Fig. 6). In this case the base of the innermost arch was lying clearly within the prominence.

The final explanation of this characteristic structure, which appears so significant for the corona, is still lacking. One is naturally tempted to attribute these structures to magnetic fields and some interesting calculations in this line have been published by J. W. Dungey (**37**). On the other hand, as in our case

here, the dome formations quite often lie outside the proper spot zone to which one would expect all fairly large magnetic fields to be confined. But the fine structure of the magnetic fields over the whole solar surface according to recent magnetographic observations (**38, 39, 40, 41**) is rather complicated so that to suppose this to be a magnetic phenomenon seems at present still one of the most promising explanations. If one attributes the differences in brightness in this corona to differences in the electron density it may also be possible under certain circumstances to account for the dome formation as a kind of natural three-dimensional velocity diagram. One could imagine that above some of the prominences in certain stages of development the electron density is very much decreased; but that periodically additional electrons are ejected for short time intervals from the prominence region, their velocities being largest in the radial direction and smaller for larger inclinations. It may be possible to account in this way for the origin of a three-dimensional space distribution in the form of elongated concentric shells or domes showing in projection what actually is observed over these prominences. The electron densities in these shells would certainly be somewhat higher than in their immediate neighbourhood. Some well-known facts agree with this conception. The jumps in acceleration observed in many prominences are usually separated by intervals of the order of an hour. Velocities of about 20 km/sec in the relevant part of the corona are certainly plausible and they have been measured on various occasions (e.g. (**42, 43**)). These values agree well with the distances between the arches of about 50 000 km as measured on the various original plates. With this idea in mind we can perhaps consider the arches as structures moving rather rapidly outwards. Plates obtained at various stations in the course of an eclipse of considerable duration should show noticeable change within two or three hours. Indeed it has been claimed that an outward movement of such arches with a velocity away from the Sun at about 16 km/sec was observed on plates from observing stations lying far apart during the eclipse of 1918 (**44**). Also motion picture films seem to indicate such motions (**45**). All this would agree well with our ideas. The present author on the other hand has measured similar arches on plates taken at intervals of $2\frac{1}{2}$ hours during the eclipse of 1926 January 14 (**26**). In this case no velocities were found to exceed 2·6 km/sec. This result would, of course, be quite invalid if the respective measurements on the various plates do not refer to the same arches (they would certainly look very much alike) and such explanation appears possible in view of the above discussion. Another possible assumption is that the dome-like envelopes come to rest at a certain height as do some prominences.

We may also ask ourselves what electron deficit may have existed in the dark dome formation of Plate 6*a*, assuming we are dealing with three-dimensional dome-like cavities, i.e. hollow spaces whose base is the diameter of the visible prominence at about $r = 1{\cdot}05$ from the Sun's centre. Within this space the apparent brightness in the line of sight is smaller by $0^{m}{\cdot}1$ to $0^{m}{\cdot}2$ than that of the immediate neighbourhood, assumed undisturbed.

We have therefore examined the question as to what electron deficit would be necessary at the relevant position angles, in van de Hulst's standard corona, to give rise to an intensity deficit such as is observed in the dome formation. For this we have assigned an intensity depression of $0^{m}{\cdot}2$, a path length within the dome in the line of sight of $0{\cdot}1r$ and a mean distance from the Sun's centre of $1{\cdot}05r$. We find the rather surprising result that there would be more or less no

electron scattering in this region, although we may admit that the photometry is not capable of deriving accurate values. A special investigation would be necessary to discover what mechanism could be made responsible for such a strong decrease in the number of electrons if indeed this should be the explanation of the dark spaces. If we have really to deal with actual cavity-like structures our results rather favour the view that they arise from a bending of corona streamers. However, one should not forget that the assumptions which form the basis of our numerical estimates doubtless correspond only rather roughly to reality, so that the computed values should be taken only as an illustration of the order of magnitude. Attention may also be drawn to two special investigations by S. G. M. Haug (**12**) dealing with the prominence at position angle 347°–4° of this corona for which he found an average electron density of the order of $1{\cdot}6 \times 10^{10}$. Earlier, in 1938, this same prominence was also studied by A. Unsöld (**46**) in a more preliminary investigation.

The Observatories,
Madingley Road,
Cambridge:
1961 *May* 1

References

(1) B. Lyot, *M.N.*, **99**, 580, 1939.
(2) M. Waldmeier, *Die Sonnenkorona*, Basel, 1951 and 1957.
(3) M. Waldmeier, *Z. f. Astrophys.*, **22**, 18, 1942.
(4) H. Brück, *M.N.*, **104**, 33, 1944.
(5) J. M. Ramberg, *Stockholm Obs. Ann.*, **16**, No. 3, 1951.
(6) A. Wallenquist, *Ann. Obs. Uppsala*, **4**, 44, 1956.
(7) H. von Klüber, *Z. f. Astrophys.*, **25**, 280, 1948.
(8) *Jahresbericht für* 1927 *der Sternwarte Hamburg*, Bergedorf 1928.
(9) S. Vsessviatsky, *Publ. Inst. Astrophys. Russia*, **4** (2), 67 (Moscow 1929).
(10) *Immagini Spectroscopiche del Bordo Solare* (Unione astronomica internationale).
(11) A. Pannekoek, N. W. Doorn, *Verh. Akad. Amsterdam Afd. Natuurk.*, **XIV**, No. 2, 1930.
(12) S. G. M. Haug, Circ. 5a, Astr. Instit. Amsterdam (1952).
(13) H. Alfén, *Cosmical Electrodynamics*, Oxford, 1950.
(14) T. S. Cowling, *Magnetohydrodynamics*, London, 1957; and *Vistas in Astronomy* (Ed. A. Beer), **I**, 313, London 1955.
(15) K. O. Kiepenheuer, *Z. f. Astrophys.*, **20**, 332, 1941.
(16) C. Walén, *Arkiv Math. Astr. och Fysik*, **33A**, No. 18, 1946.
(17) K. O. Kiepenheuer, *Nature*, **158**, 340, 1946.
—— *Annales d'Astrophysique*, **9**, 42, 1946.
—— *Ap. J.*, **105**, 408, 1947.
(18) *Greenwich Photo-Heliographic Results* 1927, London 1929.
(19) *Publ. Astr. Soc. Pacific* No. 39, 245, 320, 1927.
(20) *Astr. Mitt. Zürich*, 117, 1928.
(21) H. Ludendorff, *Sitzb. Preuss. Akad. d. Wiss. Berlin* (Math. Phys. Klasse), 1928, 16, and 1934, 16.
(22) H. von Klüber, *Z. f. Astrophys.*, **3**, 142, 1931.
(23) J. Balanovsky, E. Perepelkin, *M.N.*, **88**, 740, 1928.
(24) A. Jenvall, *Astr. Jakttagelser och Undersökningar Obs. Stockholm*, **11**, No. 8, 1932.
(25) H. von Klüber, *Z. f. Astrophys.*, **2**, 289, 1931.
(26) H. von Klüber, *Z. f. Astrophys.*, **4**, 1, 1932.
(27) A. Mikhailov, *Publ. Inst. Astrophys. Russia*, Bd. **4** (2), 49 (Moscow 1929).
(28) M. Waldmeier, *Z. f. Astrophys.*, **28**, 262, 1951.
(29) H. C. van de Hulst in G. P. Kuiper *The Sun* (Chicago 1953), p. 207ff.

XUM

(30) M. Waldmeier, *Z. f. Astrophys.*, **22,** 1 1942.
(31) M. Waldmeier, *Z. f. Astrophys.*, **21,** 124, 1942.
(32) K. Schwarzschild, *Astr. Mitt. Göttingen,* **13,** 1, 1906.
(33) H. C. van de Hulst, *Bull. Astr. Inst. Nethl.*, **11,** 408, 1950.
(34) A. H. Jarrett, H. von Klüber, *M.N.*, **122,** 343, 1961.
(35) C. W. Allen, *Rep. Progress in Physics*, **17,** 135, 1954.
(36) A. Unsöld, *Zeitschr. f. Astr.*, **50,** 48, 1960.
(37) J. W. Dungey, *M.N.*, **113,** 180, 1953.
(38) D. W. Beggs, H. von Klüber, *Nature*, **178,** 1412, 1956.
(39) A. B. Severny, *Crimean Astr. Obs.*, **20,** 22, 1958.
(40) V. E. Stepanov, *Crimean Astr. Obs.*, **20,** 52, 1958.
(41) N. V. Steshenko, *Crimean Astr. Obs.*, **22,** 49, 1960.
(42) E. Pettit, *Ap. J.*, **84,** 319, 1936.
(43) M. Waldmeier, *Z. f. Astrophys.*, **15,** 299, 1938.
(44) J. S. Miller, *P.A.S.P.*, **32,** 207, 1920.
(45) R. B. Dunn, Sacramento Peak Observatory, 1956/7.
(46) A. Unsöld, *Physik der Sternatmosphären*, 1st ed., 417, 1938.

XUM

TURBULENCE AND ROTATION IN EARLY-TYPE STARS

A. J. Meadows

(Communicated by the Director, University Observatory, St. Andrews)

(Received 1961 May 12)

Summary

The spectra of 54 early-type stars in galactic clusters have been examined in an attempt to discover the regions in the H-R diagram where large-scale turbulence and rotation are, respectively, the major sources of spectral line broadening. A demarcation line between the two regions, which varies with spectral type and absolute magnitude, has been found. The factors determining the position of this line are discussed, and the results are compared with previous stellar rotational velocity measurements.

Introduction.—Slettebak (**1**) has shown that, for weak lines not appreciably broadened by the Stark effect, line-broadening in early-type stars is predominantly due either to rotation or to large-scale turbulence. In his survey, the spectra of O- and early B-type stars always showed line-widths greater than a certain minimum value, whilst the spectra of later B-type stars occasionally showed line-widths of the same order as the instrumental broadening. It may therefore be deduced that, in the former group, large-scale turbulence is the major line-broadening mechanism (so that even pole-on stars have broadened lines), whilst, in the latter group, rotation is the major mechanism (so that pole-on stars have sharp lines).

1. *Observational data.*—The data presented by Slettebak (**1**) cover stars in the general galactic field and, therefore, for the most part, of unknown absolute magnitude. In order to divide the H-R diagram into two regions (one where large-scale turbulence is of major importance in line-broadening, and one where it is of minor importance), it is necessary to know both the spectral type and absolute magnitude of the stars involved. This may be accomplished by considering stars which are members of galactic clusters with accurately known distances. Photo-electric cluster distances have been measured recently by Johnson *et al.* (**2**) and are used in this paper. There is a possible further advantage in using cluster stars. In discussing the results, it will be assumed that the extent of large-scale turbulence depends only on the position of the star in the H-R diagram. This is an assumption which is, perhaps, easier to justify for homogeneous groups of stars.

The spectra analysed in this paper were obtained by Sanford (**3**) in connection with a survey of the interstellar calcium lines. Most of these spectra had a dispersion slightly better than 40A/mm at 4471A and 30A/mm at 4026A, but the stars in NGC 1960 had spectra of lower dispersion—approximately 80A/mm at 4471A and 60A/mm at 4026A. Not all the spectra listed in (**3**) were used. Plates were selected for (*a*) their quality, (*b*) the existence of an accurate photo-electric cluster distance, and (*c*) the existence of an accurate MK classification for the individual star. In connection with (*a*), the major drawback

XUM

was that many of the spectra had been over-exposed in order to define the interstellar lines clearly.

2. *Reduction of data and results.*—The profiles of the 4471A and 4026A lines of helium were traced for the 54 selected stars. A projected slit width of slightly more than five microns was used. Calibration was by means of a step-wedge. Apparent rotational velocities $v \sin i$ were derived by the usual method (4) of distorting the line profile of an assumed zero-velocity star—in this case HD 57682*. Owing to the low dispersion of the spectra, it was not considered realistic to try and estimate the rotational velocity of an individual star to closer than the nearest 25 km/sec. Those stars for which the spectral lines appeared unbroadened, in comparison with the standard star, are listed in Table I. It was estimated that

TABLE I

Stars with apparent turbulent velocities $v^* < 40$ km/sec

Cluster (NGC)	Star (HD or BD)	Visual absolute magnitude	Spectral type (MK)
581	9311	−4·8	B5 Ib
663	60° 343	−2·7	B2 II
869+884 (h+χ Per)	13866	−4·3	B2 Ib
	14053	−3·4	B1 II
	14134	−5·2	B3 Ia
	14143	−5·1	B2 Ia
	14443	−3·8	B2 Ib
	14818	−5·5	B2 Ia
	14956	−4·6	B2 Ia
	15690	−3·8	B1·5 Ib
1444	23675	−3·3	B0·5 III
2129	23° 1148	−3·3	B2 IIIe
	23° 1149	−4·2	B3 Ib
2244	46202	−2·6	O 8·5
6871	190919	−3·9	B1 Ib
	35° 3955	−3·9	B1 Ib
6910	194279	−4·1	B1·5 Ia

the minimum turbulent velocity v^*, which could be distinguished at this dispersion, was slightly less than 40 km/sec, the velocity v^* being defined as the most probable velocity in the random motions of large-scale turbulent eddies with a Maxwellian velocity distribution (cf. (1) and (5)). The positions of these stars in the H-R diagram are plotted in Fig. 1. Values of $v \sin i$ for stars above this minimum limit are listed in Table II.

3. *Discussion of results.*—A comparison of the results plotted in Fig. 1 with those obtained in (1) indicates quite good agreement. According to Slettebak's data, the line dividing stars with minimum $v^* < 40$ km/sec from stars with minimum $v^* > 40$ km/sec, runs from O9V, through B1 III, to B1·5 I. The choice of $v^* = 40$ km/sec as the dividing line is, of course, purely arbitrary, being decided by the plate dispersion. However, a study of the available data seems to indicate that large-scale turbulence decreases quite rapidly in importance after this limit. It may therefore be suggested, as a tentative hypothesis, that large-scale turbulence only plays a major part in line-broadening for stars to the left of the points

* This star is not a member of a galactic cluster, but was selected as it had been used as a standard in (1).

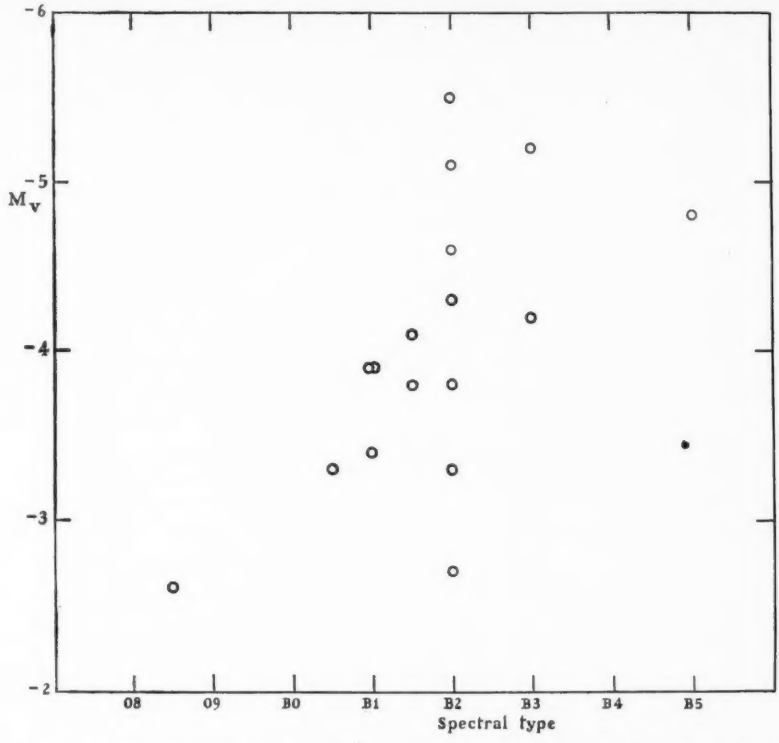

FIG. 1.—*The distribution in the H-R diagram of stars with apparent turbulent velocities* $v^* < 40$ *km/sec. Large-scale turbulence will be of major importance in line broadening in the region to the left of the plotted points.*

plotted in Fig. 1. The extent to which large-scale turbulence continues in later-type stars is uncertain. Huang and Struve (**9**) have suggested that large-scale turbulence is important in supergiants of all spectral types down to A2, but Slettebak's results (**1**) indicate that a relatively minor amount of turbulence exists in supergiants later than early B. Abt (**18**) has investigated supergiants of tybe Ib, for spectral classes Ao and later, and has shown that the large-scale turbulent velocities in these stars cannot be more than a few kilometres per second. It seems probable that a small amount of large-scale turbulence does exist in super-giants of intermediate spectral class, but any large amount of line-broadening should be attributed to axial rotation. Underhill (**10**) has considered instability in early-type stars on the assumption that this is due to radiation pressure in the stellar atmospheres. If we assume that the region in the H-R diagram, where the onset of large-scale turbulence occurs, lies in the range Bo–B2 for main-sequence stars, we can estimate the surface gravity g of these stars from the theoretical stellar models at present available (e.g. (**11**)). A comparison of the resulting values of g with the minimum values permissible for stable equilibrium derived by Underhill indicates that the former exceed the latter by a factor of between ten and a hundred.

TABLE II

Stars with apparent turbulent velocities $v^* > 40$ km/sec

Cluster (NGC)	Star (HD or BD)	Spectral type (MK)	Estimated $v \sin i$ (km/sec)
663	60° 339	B6 Iab	125
869+884	13051	B1 III	150:
(h+χ Per)	13402	Bo·5 I	50
	13745	Bo III	150
	13841	B2 Ib	50
	13969	B1 IV	125
	14357	B2 II	125
	15642	Bo IV	300:
1502	25638	Bo II–III	225
1960	120†	B2 III	150
	208a	B2 V	75
	238	B2·5 V	125
	249	B2 V	225
	250	B2 V	150
	258	B3 V	150
	313	B2 V	175
	350	B3 V	175
	365	B2 Ve	150
2244	46056	O8	200
	46106	O9·5 V	75
	46223	O6	150
	8†	O8·5	125
	13	B2 V	150:
	15	B2 V	150:
2362	57061	O9 III–V	125
6231	152233	O6	125
	152234	Bo·5 I	50
	152249	O9 I	100
6530	165052	O7	150:
6531	164844	B1 V	50
	164883	Bo V	225:
6611	168075	O7	75
	168137	O8 V	50
6871	227634	Bo II–III	50
	35° 3956	Bo·5 V	300
7160	208392	B1 IV	325:
IC4996	193007	Bo·5 II	50

Note.—A colon after a rotational velocity indicates an uncertain measurement. † The stellar designations in these clusters are those given in (**6**). The majority of the spectral classifications in both tables come from (**7**) and (**8**).

As in (**1**), the present survey showed that the line profiles of nearly all the early-type stars examined were distorted in a manner characteristic of large-scale turbulence, or of rotation, rather than by electron scattering, as suggested in (**12**). However, two stars—HD 46106 (O9·5 V) and HD 57061 (O9 III–V)—showed signs of the broad wings which characterize electron scattering. Both these stars are known to be spectroscopic binaries and both are members of clusters which contain nebulosity. The lines may, therefore, be distorted by a secondary spectrum, or by a surrounding gaseous nebula—possibilities which have been mentioned previously in this connection (**1**).

Boiarchuk and Kopylov (**13**) have suggested that rotational velocities for stars near B2 V and A2 V are a minimum as compared with the rotational velocities for stars of slightly earlier or later spectral types. A consideration of published work by Treanor (**14**) has provided some confirmation of this suggestion. The stars in NGC 1960 (except for 120) are of spectral type B2–B3 V. Their average apparent rotational velocity is 150 km/sec. This agrees well with the value of 160 km/sec given in (**13**) for the average rotational velocity at B2 V, and is distinctly less than the average rotational velocity for the early B-type stars taken as a whole. Hence, this would appear to provide some confirmation for the suggested minimum at this point. It is of some interest, in this connection, to consider measurements of rotational velocities in M39 and the Ursa Major cluster, which have been obtained previously (**15**). If the earlier, and later, A-type stars are averaged separately, it is found that the former have a distinctly lower average rotational velocity than the latter. This might be attributable to a minimum velocity in the early A-types. However, the sample of stars considered is rather small.

It should be noted that there is a selection effect present in the data of Tables I and II. Owing to the over-exposure of the plates, mentioned in Section 1, the best plates selected may have tended to be those of stars with fairly sharp lines. In NGC 1960, however, this effect should not appear, since tracings were made of all the plates available.

4. *Concluding remarks.*—It should be pointed out, in conclusion, that rotational and turbulent line-broadening effects can, to some extent, be separated in an individual star. If a sufficiently large sample of stars of a given spectral type and luminosity class are examined, then it can be assumed that the star with minimum line-width is a pole-on star. For this star, all the broadening is due to large-scale turbulence. It is further assumed that all the stars in this group have approximately the same mean turbulent velocity. Then the greater values of the line-widths measured in the other stars must be due to super-imposed rotation. We can, therefore, build up our rotationally distorted line profiles from a "zero rotational velocity" line which is itself turbulently distorted by the appropriate amount. This method is mainly of interest in estimating rotational velocities for O-type stars, where large-scale turbulence is of major importance. The number of O-stars in the present survey does not make it worthwhile to attempt such a reduction. However, by combining data from (**1**) with that obtained in the present paper, it is possible to indicate a use of this method. Taking a group of nine stars, of relatively low luminosity, in the range O6–O7 (four from Table II and five from (**1**)), their average apparent rotational velocity is approximately 155 km/sec and the minimum broadening corresponds to $v \sin i$ about 75 km/sec. According to recent calculations, e.g. (**16**), stars of this spectral type on the main-sequence should evolve through the B1–2 (II–III) region in the H-R diagram. The apparent rotational velocity of fourteen stars in this latter range (five from this paper and nine from (**1**)) is 95 km/sec and the minimum broadening corresponds to $v \sin i$ about 40 km/sec. Using this data, it can be estimated that the present observed radii are about a factor of two greater than the calculated radii if it is assumed that the stars remain in solid body rotation during evolution (cf. (**17**)). This result is, of course, based upon very meagre data, but such a discrepancy, if it is real, might indicate that the evolved stars had developed a dense core.

Acknowledgments.—The author wishes to thank Dr H. L. Johnson for permission to use his results on photo-electric cluster distances prior to publication. He is also indebted to Dr I. S. Bowen for permission to visit the Mount Wilson and Palomar Observatories as a guest investigator, and to the National Science Foundation for a grant supporting the investigation, which was awarded whilst the author was at the University of Illinois Observatory.

Note added in proof.—Corrections for interstellar absorption have not been applied to the visual magnitudes listed in Table I. The following approximate values may, however, be applied:

NGC	$3E_{B-V}$
581	1·1
663	2·6
869+884	1·7
1444	2·1
2129	2·0
2244	1·7
6871	1·4
6910	3·2

In general, therefore, the ordinate of Fig. 1 should be increased by about two magnitudes.

University Observatory,
Buchanan Gardens,
St. Andrews:
1961 *May.*

References

(1) A. Slettebak, *Ap. J.*, **124**, 173, 1956.
(2) H. L. Johnson, A. A. Hoag, B. Iriarte, R. I. Mitchell, and K. L. Hallam, *Lowell Observatory Bulletin*, Vol. 5, in press.
(3) R. F. Sanford, *Ap. J.*, **110**, 117, 1949.
(4) G. Shajn and O. Struve, *M.N.*, **89**, 222, 1929.
(5) S. S. Huang and O. Struve, *Ap. J.*, **118**, 463, 1953.
(6) P. Hayford, *L.O.B.*, **16**, 53, 1932.
(7) W. W. Morgan, A. D. Code and A E. Whitford, *Ap. J.*, *Supp.* II, **41**, 1955.
(8) W. A. Miltner, *Ap. J.*, *Supp.* II, **389**, 1956.
(9) S. S. Huang and O. Struve, *Ann. d'Ap.*, **17**, 85, 1954.
(10) A. B. Underhill, *M.N.*, **109**, 562, 1949.
(11) C. B. Haselgrove and F. Hoyle, *M.N.*, **119**, 112, 1959.
(12) G. Münch, *Ap. J.*, **108**, 116, 1948.
(13) A. A. Boiarchuk and I. M. Kopylov, *Soviet A. J.*, **2**, 752, 1958.
(14) P. J. Treanor, *M.N.*, **121**, 503, 1960.
(15) A. J. Meadows, *Ap. J.*, **133**, 907, 1961.
(16) M. Schwarzschild, and R. Härm, *Ap. J.*, **128**, 348, 1958.
(17) J. B. Oke and J. L. Greenstein, *Ap. J.*, **120**, 384, 1954.
(18) H. A. Abt, *Ap. J.*, **127**, 658, 1958.